

University of Bath
Centre for Sustainable Chemical Technologies
Department of Chemistry

Overcoming the Efficiency Bottlenecks of Metal Sulfide Solar Cells

Suzanne K. Wallace

Lead Supervisor: Professor Aron Walsh

Confirmation Report

August 5, 2016



Abstract

Due to the large energy payback time of silicon solar cells there is a strong drive to develop new solar absorber materials for cost-effective and, ideally, highly-efficient solar cells. A number of metal sulfide materials have been found to have some desirable optical properties for this application, such as direct and sunlight-matched band gaps. Furthermore, many of these materials have the additional benefit over other solar cell technologies such as CdTe and $\text{CuIn}_x\text{Ga}_{1-x}\text{Se}_2$ (CIGS) of containing only earth-abundant and non-toxic components. $\text{Cu}_2\text{ZnSnS}_4$ (CZTS) has received a great deal of scientific interest in recent years for this reason. With a direct band gap of 1.5 eV, the Shockley-Quiesser limit would predict a theoretical power conversion efficiency (PCE) limit for a CZTS solar cell of 28%. However, currently the highest performing devices are achieving efficiencies far below this limit with the PCE of record devices at around 8%, which is also much below that of similar CIGS technology. Low open circuit voltage (V_{OC}) relative to the band gap has been recognised as a key bottleneck for the performance of CZTS solar cells. Therefore a major component of this study is to investigate possible origins of this deficiency due to the fundamental material properties of CZTS. It is possible that, in spite of the ideal band gap, other fundamental and unavoidable properties of the material may hinder device performance. The second component of this study therefore is to predict the optoelectronic properties of other metal sulfide materials that until now have received little scientific interest for the application of solar cells, to determine if these materials could be candidate absorber materials for highly efficient solar cells.

Contents

Abstract	ii
1 Introduction	2
1.1 The Case for New Solar Absorber Materials for Photovoltaic Devices	2
1.1.1 Terawatt-Scale Power Production from Renewable Resources	2
1.1.2 Basic Operating Principles of a Solar Cell Device	6
1.1.3 Key Properties for Solar Absorber Materials	9
1.1.4 Current Commercial Solar Cell Technologies & Limitations	17
1.2 The Role of Computational Modelling in Material Design	22
2 Bottlenecks of Metal Sulfide Solar Cells	24
2.1 Possible Performance Bottlenecks of Cu ₂ ZnSnS ₄ Devices	26
2.2 Predicting the Properties of New Candidate Solar Absorber Materials	33
3 Background Theory	40
3.1 Models of Perfect Periodic Crystal Structures	40
3.2 Band Theory & Band Structure of Semiconductors	42

3.3 Electronic Properties of Defects in Semiconductors	45
3.3.1 Impact of Defects on the Band Structure & Optical Spectra	47
3.3.2 Impact of Defects and Disorder on Solar Cell Performance	50
3.3.3 Photoluminescence Spectra of Cu ₂ ZnSnS ₄	54
4 Monte Carlo Simulation of Thermodynamic Disorder in Cu₂ZnSnS₄	58
4.1 Mapping the Crystal Structure of Cu ₂ ZnSnS ₄ onto a Simple Lattice	58
4.2 Monte Carlo Simulation with the Metropolis Algorithm	61
4.3 Equilibration & Finite Size Effects	64
4.4 Multi-Scale Approach with Density Functional Theory	70
4.5 Spatial Extent of Disorder Amongst Cu & Zn Ions	71
4.6 Quantification of Disorder Using Radial Distribution Functions	72
5 Conclusion & Future Work	74
5.1 Further Development of Monte Carlo Disorder Models for Cu ₂ ZnSnS ₄	74
5.2 Predicting the Photovoltaic Performance of Other Metal Sulfide Materials	77
A Calculation of the Formation Energy of the [Cu_{Zn}⁻ + Zn_{Cu}⁺] Defect Pair in Cu₂ZnSnS₄	83
B Density Functional Theory (DFT) Methodology for the Calculation of Total Energy	89
C Convergence of Total Energy with Number of K-Points for Geometry Optimization of Sulfosalt Crystal Structures	95

D High Symmetry Paths for Sulfosalt Band Structure Calculations	97
Bibliography	98

Chapter 1

Introduction

1.1 The Case for New Solar Absorber Materials for Photovoltaic Devices

1.1.1 Terawatt-Scale Power Production from Renewable Resources

It is now widely accepted that the world is heading towards a major energy crisis, where there will come a point that the current major sources of energy (namely fossil fuels) will be unable to meet increasing global demand for energy. Furthermore, there is the ever present worry of climate change linked to increased carbon dioxide emissions from the burning of fossil fuels. Renewable, low-carbon alternatives are therefore clearly desirable. From purely environmental considerations, it seems clear that we should meet our energy needs solely from renewable, low-carbon energy resources such as solar power. However, we must also consider the economic feasibility of solar power for large-scale projects. Germany is an example of a country making considerable efforts to increase the percentage of their energy supplied by solar power. On the 9th of June 2014 Germany even generated over 50% of its electricity demand from solar for the first time [147]. Although on average the country is not able to produce such a large portion from solar power, with solar-generated power providing approximately 7.5% of net electricity consumption in 2015 [151]. To facilitate the growth of the solar power capacity in Germany a

number of schemes and financial incentives to encourage investment were introduced, such as feed-in tariffs (FiTs). FiTs set the rate a utility company must pay for renewable generated energy and guarantee the provider of renewable energy a specific rate for a long period of time, typically fifteen to twenty years. As this cost is higher than fossil fuel based electricity, the higher price is then passed on to all customers of the utility company to spread out the higher costs. In Germany, this has resulted in an increase of 6% on the average electricity bill for users in a specific region [98]. The social implications of such a cost increase must also be considered in assessing the viability of a particular power source.

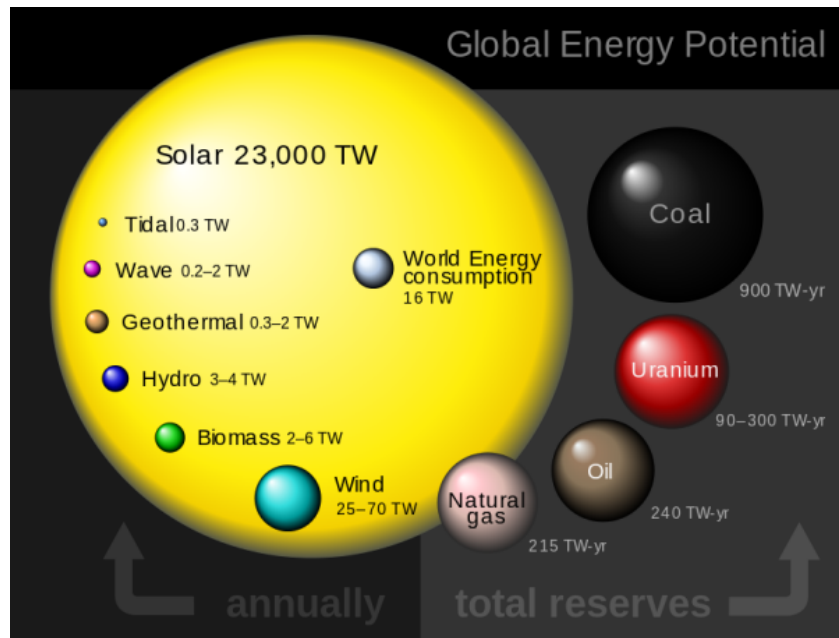


Figure 1.1: Illustration of power available annually from various renewable energy resources, annual world energy consumption and total reserves of various non-renewable energy resources. Figure take from reference 142.

However if solar power, in combination with proper energy transport, storage and secondary conversion into heat and fuels, could be made to be economically feasible; it is a realistic candidate for replacing fossil fuels as a major supply of global energy. It is by far the largest source of energy available to us, as illustrated in figure 1.1, and it is also the most widely geographically distributed [62]. The Sun supplies 3×10^{24} J of energy to the Earth each year, which is around 10^4 times more than mankind's current annual energy consumption. Assuming a fairly modest module efficiency of 20% and 50% losses related to storage and secondary conversion, 1.6% of the Earth's land area would be required for solar-generated power

to meet current world energy needs [111]. Although this would be a fairly large area, it would not be completely unrealistic. For instance, this area would be less than 5% of the area used for agriculture worldwide [111]. The area required could also be reduced further through improvements in the efficiency of photovoltaic (PV) modules and by making use of building-integrated PV (BIPV) innovations, largely made possible by flexible, thin-film second generation PV technologies which are discussed further in section 1.1.4. An example of a BIPV project is shown in figure 1.2, where solar panels are not only placed on the roof of a building but can also be placed on the windows and outer walls.



Figure 1.2: A building integrated photovoltaics (BIPV) project fitted in the United States by BISEM-USA [14].

Recent years have seen a rapid increase in the installed solar generation capacity, with the global grid-connected PV capacity growing from 1.3 GW in 2000 to 139 GW in 2014 [8], with approximately a doubling in the cumulative installed capacity every two years [65]. Additionally, creative business models have spurred investment in residential solar systems [99]. Great improvements in technology, price and performance have helped to facilitate this growth, but solar energy still only provides a minor fraction of the world's energy. In 2013 solar power only provided 0.87% of the world's electricity [112]. Further advances are required to enable a dramatic increase in the contribution from solar power at socially acceptable costs [99]. Ultimately, solar power-generation technologies must become cost-competitive with conventional fossil-fuel based power sources.

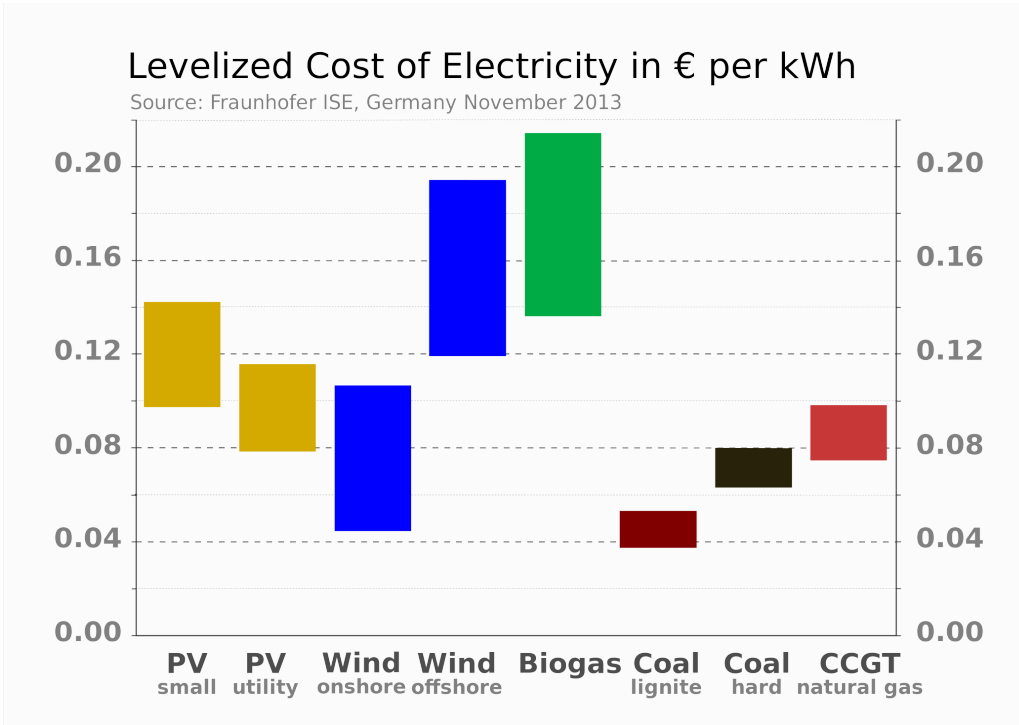


Figure 1.3: Levelized cost of electricity (LCOE) of renewable energy technologies and conventional power plants at locations in Germany in 2013. Specific investments are taken into account with a minimum and maximum value for each technology. Figure taken from reference 42.

Levelized cost of energy, or electricity, (LCOE) is a common way to assess how cost competitive renewable energy sources are with their non-renewable counterparts. LCOE allows for the measurement of the performance of different power generating technologies, which may have unequal lifetimes and differing capacities. It is calculated by summing all costs incurred during the lifetime of the technology and dividing this value by the units of energy produced during the lifetime, with units of energy expressed as dollars per kilowatt hour (\$/kWhr) [83]. This measure is also used as the key selling point for a number of commercial solar cell manufacturers such as First Solar Inc., who market their product as being able to generate electricity at an average of \$0.63 per Watt as stated in their 2013 Annual Report [61]. Using the LCOE, comparisons of grid competitiveness for renewable energy sources can be made [83]. Figure 1.3 shows the LCOE of renewable energy technologies and conventional power plants at locations in Germany in 2013, enabling an assessment of the cost-competitiveness of PV power generation at this location, accounting for, for example, typical solar irradiation at the given locations [42]. As the figure shows, both small-scale and large-scale utility solar power are still not cost

competitive with the cheapest non-renewable resources.

1.1.2 Basic Operating Principles of a Solar Cell Device

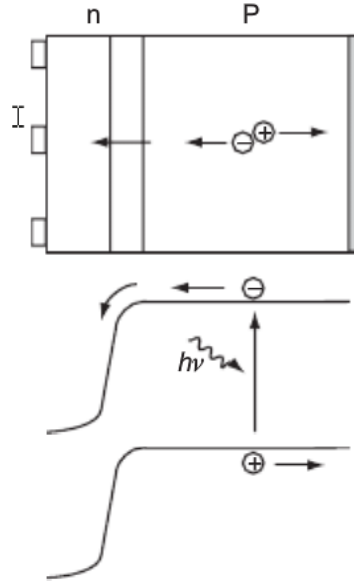


Figure 1.4: Schematic of a typical crystalline silicon solar cell device (top), where the majority of the cell consists of a thick p-type base in which most of the light is absorbed. After light absorption, the minority carriers (electrons) diffuse to the junction where they are swept across by the strong built-in electric field. The electrical power is collected by metal contacts to the front and back of the cell. Excitation of an electron-hole pair across the band gap of the p-type material (bottom). Figure taken from reference 85.

A solar cell device converts solar energy directly into electrical energy. Solar energy can be described as either a spectrum of electromagnetic radiation or a flux of photons and electrical energy is a flow of charge carriers able to do work in an external circuit [19]. Voltage is generated in a solar cell device by the photovoltaic effect. The terms ‘solar cell’ and ‘photovoltaic (PV) cell’ are therefore often used interchangeably. Semiconducting materials are usually utilized in a PV device. A semiconductor is described by its valence and conduction energy bands i.e. a group of energy levels, which electrons may occupy, and a gap in between with no available energy levels called the band gap. In thermal equilibrium at 0 K, all energy levels in the valence band are occupied by electrons while all energy levels in the conduction band remain unoccupied. Energy level occupancy at finite temperatures is usually described by the Fermi-Dirac distribution [19].

In the case of a perfectly pure semiconductor, only photons with energies higher than the band gap can be absorbed to excite an electron from the valence band into the conduction band. Photoexcitation results in the formation of an electron-hole pair, as shown in figure 1.4. The photoexcited electron-hole pair would eventually recombine and relax back to the ground state of the material with the emission of a photon of an energy equal to the energy of the electronic transition that has just occurred. However in a PV device, there is a built-in asymmetry that leads excited charge-carriers away before they can recombine back to the ground state. The extra energy of the excited electron generates a potential difference that drives electrons through a load in the external circuit to do electrical work. In the conventional PV effect, as electrons are excited across the band gap of a semiconductor, the band gap of the material sets the upper limit for the maximum voltage that can be generated. In early PV devices, the asymmetric junction was a Schottky barrier between a metal and a semiconductor but now more effective p-n junctions are used, which are formed by joining together p-type and n-type semiconductors [92].

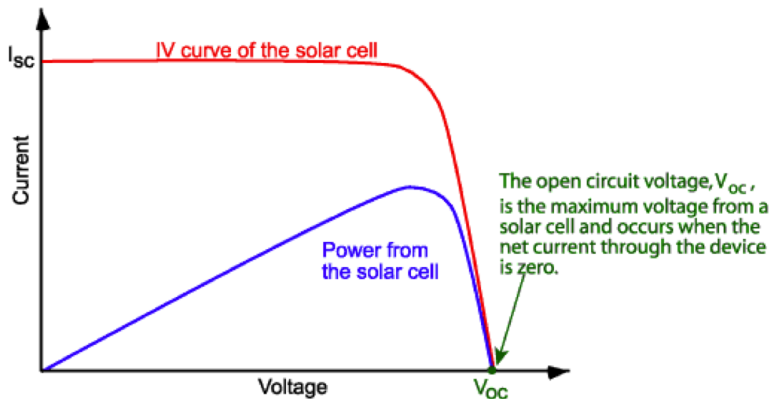


Figure 1.5: The current-voltage (I-V) curve of a solar cell showing the open circuit voltage (V_{OC}). Figure taken from reference 59.

When a cell consisting of a p-n junction is illuminated, a voltage develops across the terminals, i.e. between the p-type and n-type semiconductors. When the terminals of the solar cell are disconnected from any external circuit, or there is an infinite load resistance, this voltage is at a maximum and is called the open circuit voltage (V_{OC}) and no current is drawn from the solar cell. Conversely, if the terminals of the solar cell are connected together then there is no voltage as all of the electromotive force is used to extract charge-carriers. The maximum

possible current is drawn, which is called the short circuit current (I_{SC}). For a solar cell to generate power, there must be both voltage and current generated, therefore when the cell is operating at either V_{OC} or I_{SC} the power output is zero. To generate power, a finite load resistance is added to the circuit so that some current is drawn from the solar cell and a voltage develops across the cell that is between 0 and V_{OC} [92]. There is a maximum operation point for the power output (P_{MP}) of a solar cell in terms of I and V, as shown in figure 1.5. This can be defined in terms of V_{OC} and I_{SC} when used in conjunction with the fill factor (FF), which is a number less than one that describes the squareness of the I-V curve [51] shown in figure 1.5 and is given by equation 1.1. The current and voltage are determined by the load and illumination so the load can be tuned such that maximum power output is achieved, but the value of V_{OC} places a limit on the power output of the cell [92].

$$P_{MP} = FFV_{OC}I_{SC} \quad (1.1)$$

$$\eta = \frac{P_{MP}}{P_{in}} = \frac{FFV_{OC}I_{SC}}{P_{in}} \quad (1.2)$$

The power conversion efficiency (PCE), η , of a solar cell is the ratio of power output from the solar cell to the power input from the Sun. This is shown in equation 1.2, where P_{MP} has been taken from equation 1.1. For an efficient solar cell, it is desirable to have a high I_{SC} , a high V_{OC} and a FF that is as close to 1 as possible [51]. Investigating the possible causes of the low efficiency of $\text{Cu}_2\text{ZnSnS}_4$ (CZTS) solar cells is a major component of this study. Devices made from this material typically have a high short-circuit current density, but have a low efficiency compared to other PV devices due to a large deficit in the open-circuit voltage compared to the band gap of the material [90]. Whereas in ferroelectric PV materials, photovoltages orders of magnitude larger than the band gap have been measured (a phenomena referred to as the anomalous photovoltaic effect), but very low photocurrent output is a big challenge for these devices [159]. However materials with such novel properties could provide a means of creating more efficient solar cell devices. For this reason, another component of this study is to investigate the potential of other materials for PV applications which could exhibit such novel phenomena.

1.1.3 Key Properties for Solar Absorber Materials

A solar (or photovoltaic) cell is an example of an optoelectronic device in which the solar absorber material of choice must allow for the manipulation of light, electrical current and their interaction. Metals are excellent electrical conductors, but do not allow light to travel inside. Glass and related dielectric materials can accommodate and guide light waves, as in electrical fibres, but are electrical insulators. Semiconductors are in between these two types of material as they can carry both electrical current as well as light waves [109]. Furthermore, some semiconductors can be used to transform light into electrical current, which was described in the previous section. The two vital processes that must occur in a solar absorber material were also mentioned: the excitation of an electron across the band gap from the valence band into the conduction band in a semiconducting material by a photon and the subsequent collection of the photoexcited charge carriers by an external circuit before the photoexcited electron-hole pair recombine. There are certain optical and electrical properties that are necessary for these processes to occur and then there are also certain properties that indicate how well a material is likely to perform in a solar cell device. In this section the band gap, effective mass, dielectric function and absorption coefficient of a potential solar absorber material will be discussed.

The most obvious necessary requirement for a solar absorber material is for it to be a semiconductor so that it possesses a band gap across which an electron can be excited. The value of this band gap must also be somewhere within the energy range of the solar spectrum shown in figure 1.6, so that sunlight can induce the photoexcitation of an electron-hole pair across the band gap. Secondly the material must allow for the transport of charge carriers out of the absorber material and into a collection electrode and external circuit in order to do electrical work. Provided these necessary conditions are met and some sort of spatial asymmetry is present to drive electrons away from their point of promotion, the material should exhibit the photovoltaic effect [93]. However, how well it will actually perform in a solar cell is determined by more stringent criteria and other material properties. Firstly the actual value of the band gap within the range of the solar spectrum is of importance. It is ideal for the value to be as close as possible to the region of photon energies that make up the majority of the solar

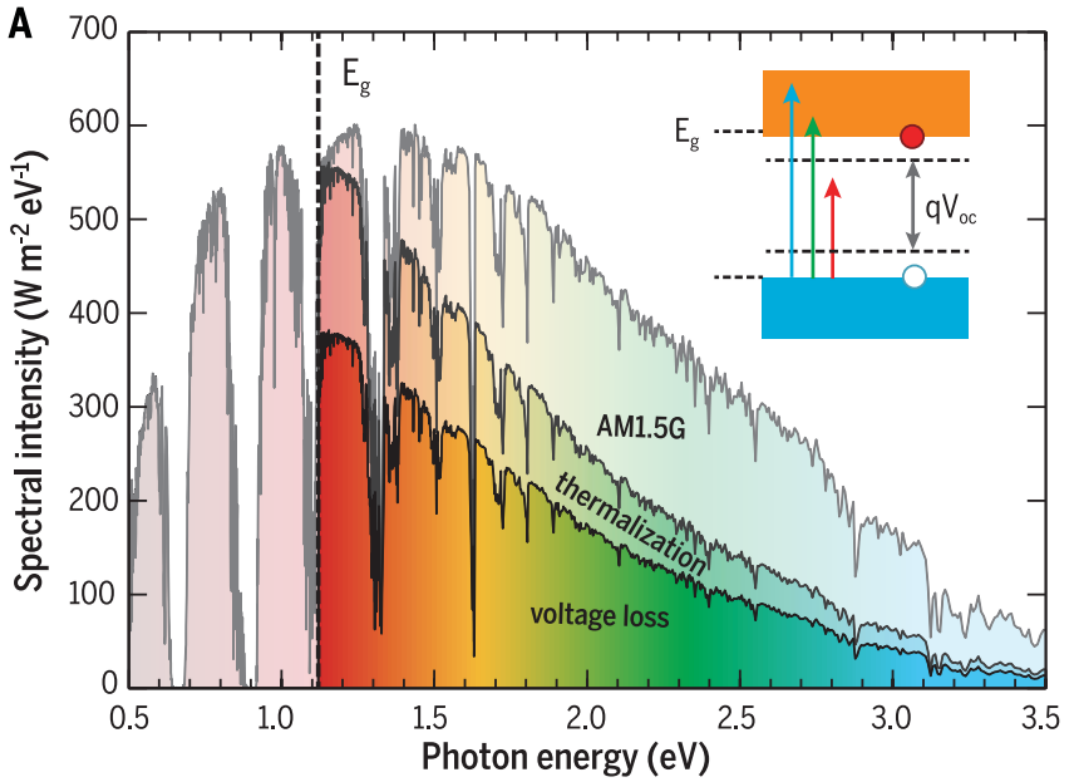


Figure 1.6: AM1.5 solar spectrum with distinct dips due to molecular absorption in Earth's atmosphere. The dashed line shows the band gap of silicon and fading to the left indicates that photons with energies below the band gap will not be absorbed and other fading indicates other loss mechanisms that prevent a solar cell from being unable to convert the full incident spectrum into electricity. Figure taken from reference 111.

spectrum. The optimal range for the band gap under typical radiation conditions is between 1.06 eV and 1.50 eV [63]. The upper limit of the power conversion efficiency (of incident photon energy into electrical energy) by a device made from a particular absorber material based on its band gap was first calculated by Shockley and Quiesser in 1961 [126]. A plot of theoretical efficiency limit as a function of band gap is shown in figure 1.7, as well as the record efficiencies of various PV technologies.

However, it is not only the value of the band gap that is of importance. More intricate details of the band structure of the material can also impact on the performance of a solar cell device made from the material. Band theory and band structures will be discussed more in section 3.2, but it is worth noting at this point whether the band structure shows a band gap that is direct or indirect can have an impact on the performance of a solar cell made from the material. Figure 1.8 shows the band structures of Si and GaAs, where Si possesses an indirect band gap

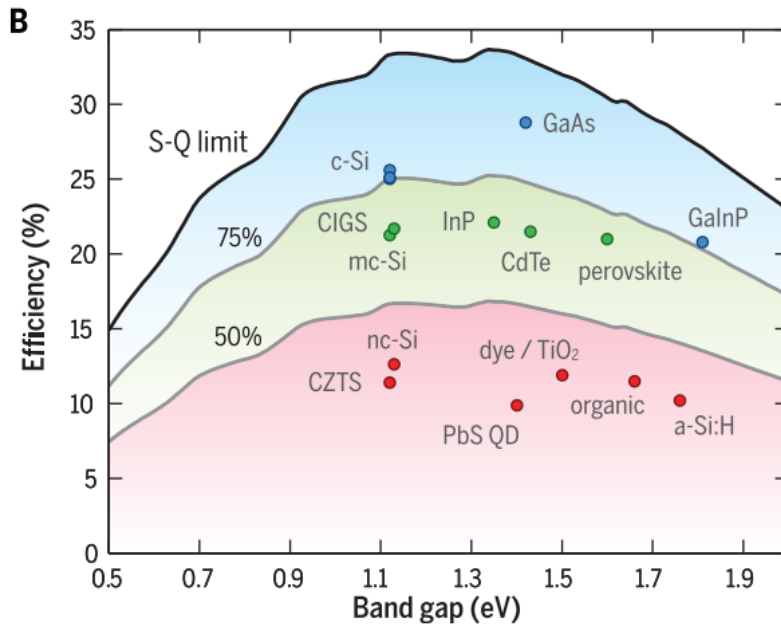


Figure 1.7: Theoretical Shockley-Queisser detailed-balance efficiency limit as a function of band gap[126] (highest black line). The record efficiencies for different materials are plotted for the corresponding band gaps, where materials below the lower two grey lines are achieving conversion efficiencies less than 75% and 50% of their theoretical efficiency limit respectively. Figure taken from reference 111.

and GaAs possesses a direct band gap. The excitation of an electron directly from the valence band to the conduction band is called fundamental absorption, as there are several other optical absorption transitions that can occur in a semiconducting material, especially in a defective material, and this point will be discussed more in section 3.3.1. Both the total energy and momentum of all particles involved in the absorption process must be conserved. Photons do possess momentum ($\frac{h}{\lambda}$), however this is very small compared to the range of crystal momenta and so the electron momentum is effectively conserved during photon absorption. For a direct transition, the absorption coefficient of a material for a given photon energy $h\nu$ is proportional to the probability, p_{12} , of the transition of an electron from the initial state E_1 to the final state E_2 , the density of electrons in the initial state, $g_v(E_1)$, and the density of available final states, $g_c(E_2)$. This is then summed over all possible transitions between states where $E_2 - E_1 = h\nu$. Since the electron momentum is conserved during a direct transition, the crystal momentum in the valence band is approximately the same as that of the final state in the conduction band at energy E_2 [84].

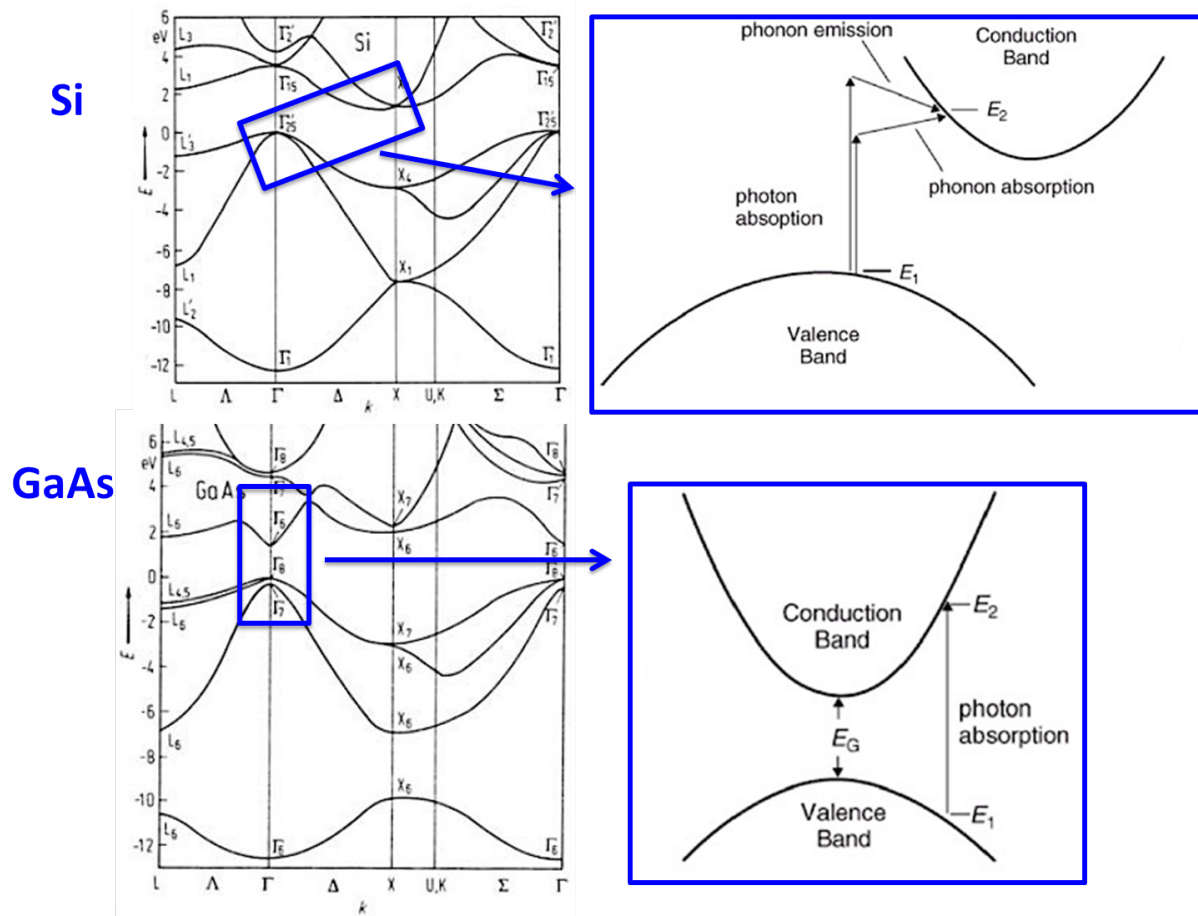


Figure 1.8: The band structure of silicon and a schematic of the absorption process in an indirect band gap semiconductor (top). The band structure of GaAs and schematic of the absorption process in a direct gap semiconductor. Figures adapted from 52 and 84.

However for an indirect band gap semiconductor, such as silicon shown at the top of figure 1.8, the valence band maximum occurs at a different crystal momentum to that of the conduction band minimum. As discussed earlier, the momentum of a photon is far less than that of crystal momenta. In order to conserve the momentum of an electron during an optical transition across an indirect band gap, momentum must be either provided by the lattice or released to the lattice usually in the form of the particle representation of a lattice vibration, known as a phonon, as indicated in the top right schematic of figure 1.8. Since both a phonon and an electron are needed to make an indirect transition possible, the absorption coefficient depends not only on the density of states of the electrons, as for a direct transition, but also on the availability of emitted or absorbed phonons with the required momentum. Therefore, the absorption coefficient for an indirect transition compared to a direct transition is typically relatively small. Consequently, light penetrates more deeply into an indirect band gap semiconductor before

being absorbed. In order to absorb the same amount of light therefore, the absorber layer of a device made from an indirect band gap semiconductor must therefore typically be thicker [84]. This is undesirable if the particular material contains rare or expensive components and also results in higher demands on material quality as charge carriers must be transported through the absorber material in order to be collected.

Another property of importance that can be derived from the band structure of a material is the effective mass. The effective mass is related to the curvature of the band at the top of the valence band (for holes) or at the bottom of the conduction band (for electrons). The effective masses of electrons or holes are the masses they seem to carry for transport properties [10]. For example, in ZnSnO_3 the hole effective mass has been calculated to be large, indicating that hole mobility will be poor in this material. Poor mobility will make carrier extraction difficult, which has been linked to the low photocurrents observed in this material [70]. Effective masses are calculated by fitting a formula to the band extrema. However, just from a quick inspection of the band structure of a material, a more steeply curved shape to the band extrema indicates a lower effective mass and therefore higher carrier mobility. Figure 1.9 shows a schematic of the band structure of a direct band gap semiconductor that has both heavy- and light-hole bands at the valence band extremum, where the flatter band corresponds to the heavy-hole band. Although certain thin-film technologies, which will be discussed towards the end of section 1.1.4, reduce the amount of absorber material the charge carrier must travel through before being collected. So although carriers must still travel through the material, effective mass could be considered less of a crucial parameter for this technology. Furthermore, the effect of the effective mass on the transport properties could be overshadowed by scattering of charge carriers by defects in a real, non-ideal material. It is the dielectric function of the material that provides more insight in this case, which is discussed below.

Materials with ionic or covalent bonding, or a mixture of the two, are usually either insulators or intrinsic semiconductors. Due to this type of bonding, electrons are bound to the atomic structure and so are unable to move throughout the material when an electric field is applied as in a metal. However, these materials can be polarized by an applied electric field where electrons are displaced relative to their nuclei by small distances. When an external electric

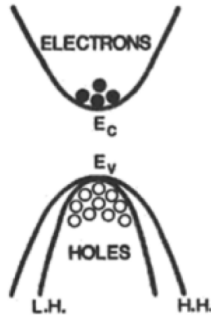


Figure 1.9: Schematic of the band structure of a photoexcited semiconductor with electrons near the bottom of the conduction band, holes near the top of the valence band, where the particular material has both heavy- and light-hole bands (labelled H.H and L.H in the figure respectively). Figure taken from reference 80.

field is applied, the positive and negative charges experience electric forces tending to move them apart in the direction of the external field so that their centres of gravity no longer coincide [161]. The material is now said to be polarized and an electric displacement field (\vec{D}) appears within it. The applied field (\vec{E}) and displacement field are linked by the macroscopic dielectric function of the material, ϵ_r , as shown by equation 1.3 [10], which is a function of the frequency of the applied field.

$$\vec{D} = \epsilon_0 \epsilon_r \vec{E} \quad (1.3)$$

The dielectric function indicates the ability of a material to screen the external electric field by the apparition of a polarization. In a solid, this polarization comes from the re-organization of the electronic density or from the motion the ions that make up the material. These two mechanisms are illustrated in figure 1.10a and associated frequencies of the applied field to induce particular polarization responses are shown in figure 1.10b. The contribution to the dielectric function from the electronic density, sometimes referred to as the high-frequency dielectric function, is denoted as ϵ_∞ and the contribution of ionic motions is denoted ϵ_{vib} in equation 1.4 [10], and is sometimes referred to as the static or low-frequency dielectric function.

$$\epsilon_r = \epsilon_\infty + \epsilon_{vib} \quad (1.4)$$

The value measured for the dielectric function for various frequencies of the applied electric field can give information about different dielectric responses of the material, some of which were

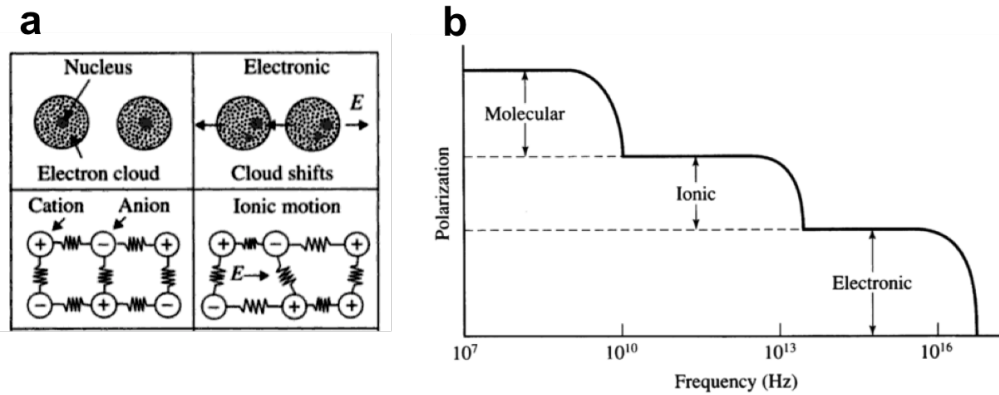


Figure 1.10: Polarization mechanisms in a crystalline solid: response of electronic density and motion of ions (a), figure taken from 96. Typical frequencies of applied electric field to induce polarization mechanisms, where the response at high frequencies is only that of the electronic density (b), figure adapted from reference 60.

shown in figure 1.10. Furthermore, the dielectric function is usually a complex quantity, where the imaginary part corresponds to a phase shift of the polarization relative to the applied electric field and leads to the attenuation, i.e. a gradual loss in the intensity, of electromagnetic waves as they pass through the material. The dielectric function is an important material property for a photovoltaic material for a number of reasons. Firstly, it can be shown that the absorption of a material, which has been discussed already as a way of comparing the performance of materials with direct and indirect band gaps in a solar cell, is mainly determined by the imaginary component of the dielectric function [43]. The band gap determines the minimum energies photons must have in order to be absorbed by a material, but it does not predict how strongly that material will absorb them. In fact, it has even been suggested that when screening for candidate solar absorber materials, a direct band gap within the optimal range for the solar spectrum is not a sufficient criteria as this does not guarantee that the onset of absorption near the band gap is strong [157]. In this particular work, instead of the Shockley-Quieser limit mentioned earlier, they recommend an alternative screening metric, the Spectroscopic Limited Maximum Efficiency (SLME), which depends explicitly on the calculated absorption spectrum of the material.

The optical absorption coefficient of a material, α , determines the penetration depth, $\frac{1}{\alpha}$, of light incident on the material [165]. Figure 1.11 shows the absorption coefficients of different

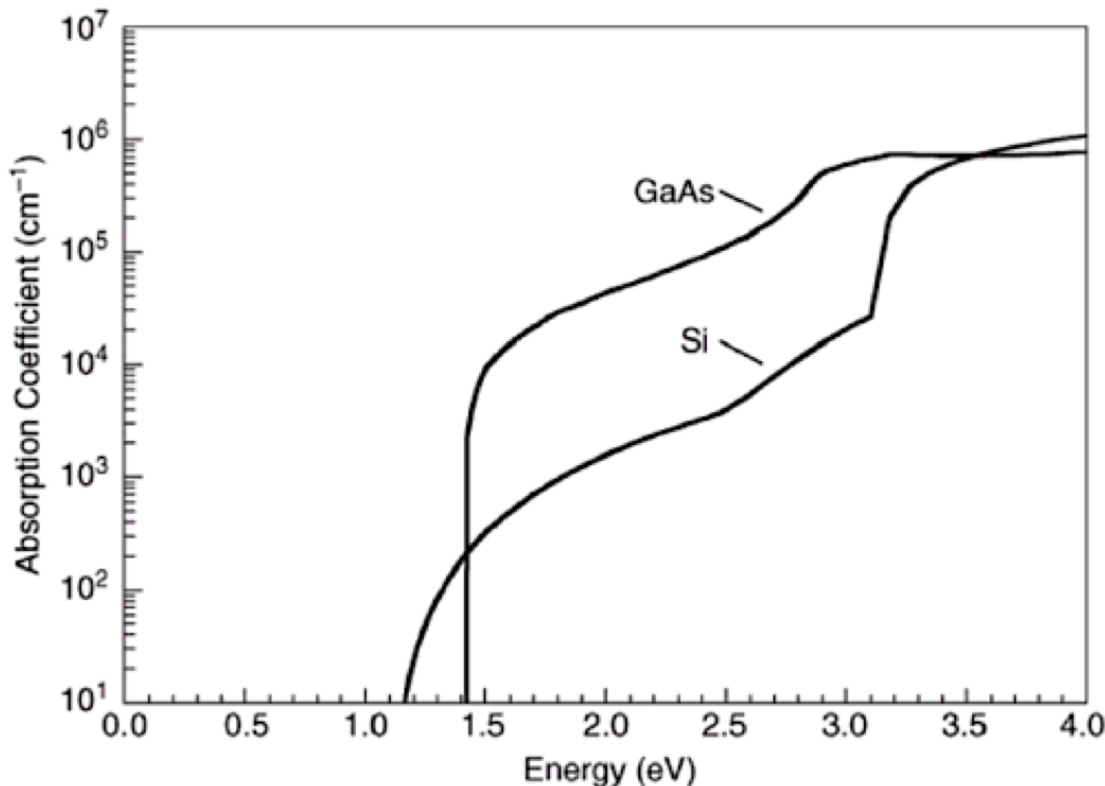


Figure 1.11: A comparison of the absorption coefficients of the indirect band gap semiconductor Si and the direct band gap semiconductor GaAs across a range of incident photon energies. Figure taken from reference 84.

semiconductors across a range of wavelengths. The figure shows a less steep onset of absorption for silicon, which as discussed earlier possesses an indirect band gap, compared to that of GaAs for which the absorption corresponds to a direct band-to-band transition. The implication of the differing absorption coefficients and therefore different optical penetration depths of materials for solar devices is that materials which are stronger absorbers require less material to absorb the light. This forms the basis of thin-film solar cell technologies, where a less high-quality and defect-free absorber layer is necessary as charge carriers do not have to travel through as much of the material in order to reach a collection electrode. Different solar cell technologies will be discussed further in section 1.1.4. Defects in the absorber layer do still play a decisive role in determining the device performance of thin-film PV technology, and this point is discussed much more in section 3.3.2.

The dielectric function of an absorber material has yet more implications on the performance of a PV device made from that material. The electrostatic force between an electron-hole pair

is reduced when the static (or low-frequency) ϵ_r is larger [10] due to the enhanced screening of the charge. This, therefore, will reduce the recombination of electron-hole pairs in a material. Another aspect of this property important for photovoltaic materials is that it can improve the defect tolerance of the material. In the majority of cases producing perfectly defect-free materials is impractical, if not impossible. The impact of defects in a material on photovoltaic performance will be discussed more in section 3.3.2, but for now it is just worth noting that defects can trap charge carriers, enhance electron-hole recombination (reducing carrier lifetimes in the material) and therefore have the overall effect of reducing charge collection from a PV device, thereby decreasing the efficiency of the conversion of incident photons into electrical current. In reference to modelling electronic transport in a material in the presence of defects, ϵ_r has been referred to as the most important property of the material [23]. A higher dielectric function indicates a greater ability to screen charge. The capture cross-section for charge carriers by a charged defect will therefore be influenced by the value of ϵ_r of the material [23]. This property can therefore indicate how well photo-excited charge carriers will be transported through a defective photovoltaic material, towards an electrode for carrier collection and on to do electrical work.

1.1.4 Current Commercial Solar Cell Technologies & Limitations

It was first observed in 1839 by Edmond Becquerel that sunlight could be used to generate electricity. Becquerel discovered that if silver chloride was placed in an acidic solution, connected to platinum electrodes and exposed to sunlight, an electric current flowed. However the effect was small and poorly understood before Albert Einstein's discovery of the photoelectric effect and explanation of the phenomena by the quantum nature of light in 1904 [131]. Even then, it was not until the development of semiconductor technology during the silicon revolution of the 1950's that solar cells were fabricated which were able to generate significant amounts of electricity. The first silicon solar cell was created in 1954 in the Bell Laboratories with cells achieving efficiencies of 6%. Originally solar cells were developed for terrestrial energy generation, such as the 108 solar cells used to supply energy to the Vanguard satellite in 1958 [131].

The first oil crisis in 1973 however highlighted the dependency of many economies on fossil fuels and the need to address the security of energy supply, in particular for Japan and West Germany which had few of their own resources. As a consequence, solar cell research was no longer limited to only high-cost crystalline silicon devices for terrestrial applications, but also into creating cheaper, commercial, thin-film solar cell technologies using absorber materials such as amorphous silicon, cadmium telluride and copper indium diselenide [75].

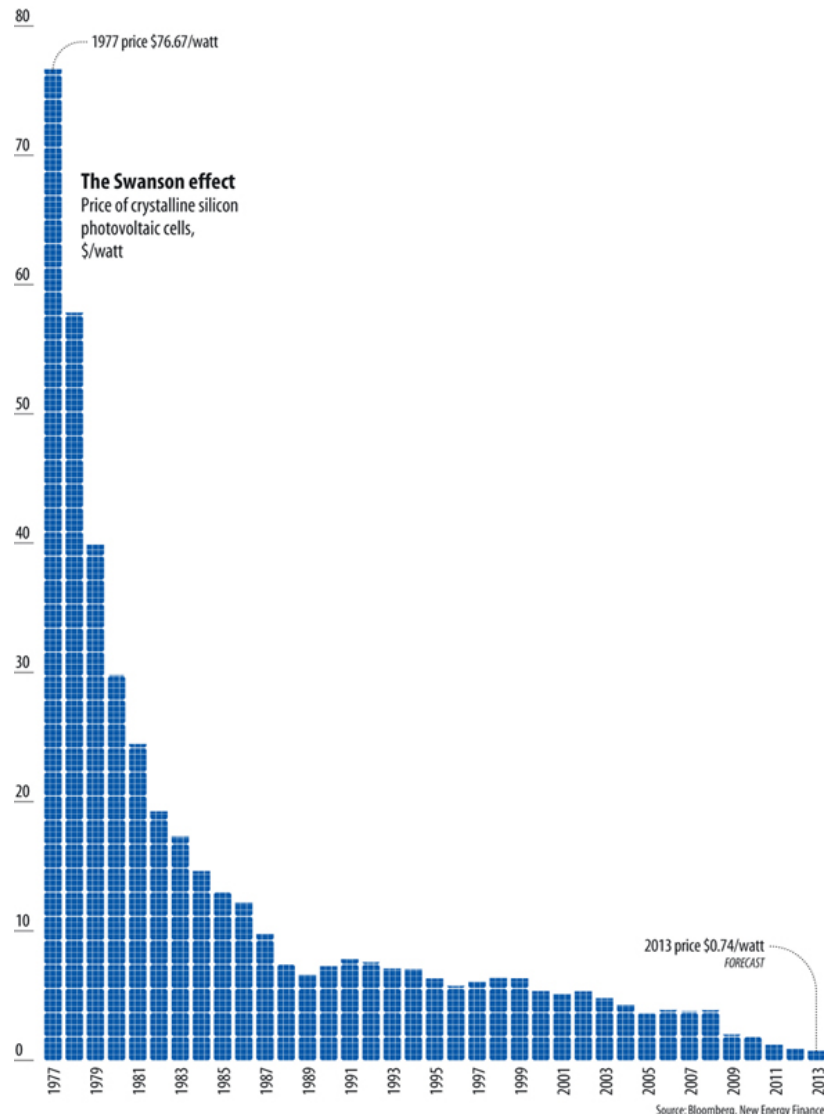


Figure 1.12: Average cost of solar panels composed of a crystalline silicon absorber layer. Figure taken from reference 125.

In spite of this, crystalline silicon is still the dominant solar cell technology with mono- and poly-crystalline silicon photovoltaic cells comprising up to 90% of all the solar cells produced in 2008 [117]. Silicon is the second most abundant element in the Earth's crust [48], making it

a plausible material to use in large-scale solar power generation. Over 60 years of development have seen device efficiencies increase from 6% to 25% for the highest quality research devices and 15-18% for the more common industrial cells [117]. As can be seen from figure 1.7, the best performing silicon devices are now very close to achieving conversion efficiencies close to their theoretical limit, as predicted by Shockley-Quieser [126]. More dramatic however is the fall in manufacturing costs which have halved since 2008 and are more than a hundred times lower than they were in 1977, as shown in figure 1.12. This development was largely aided by progress in semiconductor technology driven by the silicon chip industry, with the solar industry benefiting from advances in silicon manufacturing processes and even making use of waste silicon produced that was not of a high enough grade for silicon chips [131]. Although the development of silicon-based technologies has clearly revolutionized the modern computer, the optical properties of silicon do not make it ideal for use as a solar absorber material in a photovoltaic device and despite the dramatic reduction in manufacturing costs, the technology is still not able to be cost-competitive with fossil-fuel power generation, as was shown in figure 1.3.

The primary issue with silicon is that its band gap of 1.1 eV is indirect. The key consequence of this property is that silicon is therefore not a very strong absorber of sunlight (compared to for instance newer, thin-film technologies which are discussed later), resulting in a low optical absorption coefficient compared to these newer technologies where both band gap and absorption coefficient were two of the key material properties for solar cells discussed in section 1.1.3. To absorb the same amount of sunlight with a silicon solar cell requires a thicker layer of the material than in thin-film technologies. Photovoltaic devices are very sensitive to defects and impurities. This point is discussed further in section 3.3.2, but the consequence for a thick layer of silicon is that very high quality, non-defective material is necessary to enable charge carrier collection before recombination occurs, which results in high manufacturing costs. The devices are made from flat sheets of crystalline or multicrystalline silicon called wafers that consist of very high quality silicon (99.999999% pure) [97]. The production processes of silicon wafers have been thoroughly optimised, but are still very energy-intensive, time-consuming and complex [55] and this is reflected by the position of this type of technology on the plot of

efficiency versus cost shown in figure 1.13. Despite decades of development, commercialized silicon solar panels are still too expensive to compete with fossil-fuel based power sources [124].

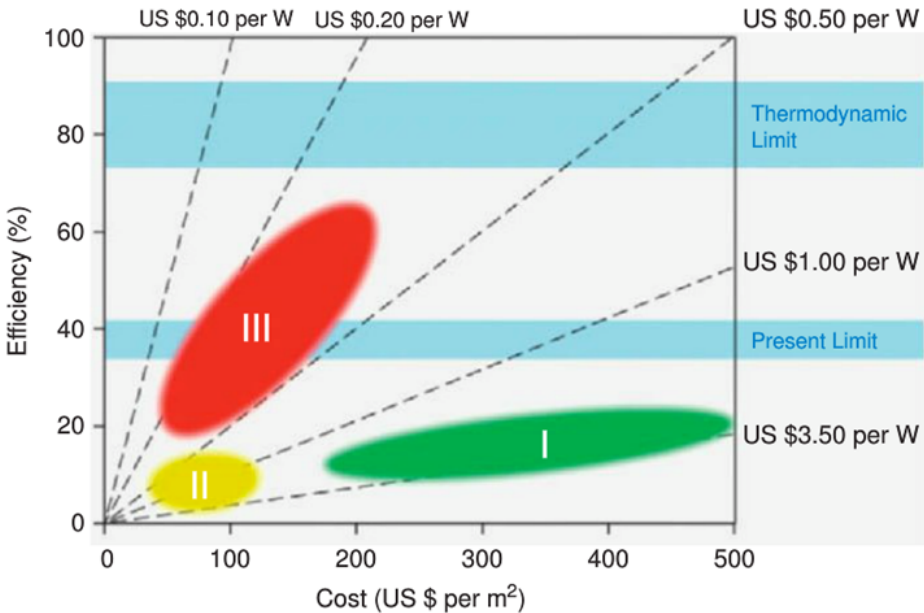


Figure 1.13: Efficiency and cost projections for first-, second- and third-generation photovoltaic technologies, which are comprised of silicon wafer, thin-film and advanced thin-film technology respectively. Figure taken from reference 47.

The ‘holy grail’ of research into new materials for photovoltaic devices would be to find materials that are strong absorbers of sunlight, could be produced cost-effectively and composed of materials that are abundant enough for large-scale fabrication of the devices. Such a drive has resulted in the development of what are considered three generations of solar energy technology. These are shown in figure 1.13, where highly efficient crystalline silicon devices with high associated manufacturing costs are considered the first generation of solar cell technology. Thin-film solar cell devices are typically referred to as second-generation technology. These devices make use of materials that are much more optically thick than silicon (i.e. stronger absorbers of sunlight with higher optical absorption coefficients), which require less material to absorb the same amount of sunlight. Figure 1.14 shows a comparison between the thickness of the absorber layer in some commercial second-generation PV devices to that of first-generation silicon wafers. The consequence of the reduction in the thickness of the absorber layer is that it is then less important for the material to be of as high-quality as in crystalline silicon devices, which enables the use of low-cost and low-energy fabrication methods [55]. In the case of thin-film CuInSe₂

devices, it has even been found that the ‘lower quality’ poly-crystalline material has a higher performance than its single crystal counterpart [118, 113]. Theoretical studies of the electronic properties of the grain boundaries in CuInSe₂ have provided an explanation for this unusual observation based on beneficial band offsets at the grain boundaries [107, 108]. This effect is a special case for this particular material, but it embodies the general ideology of thin-film technology well - namely to produce materials able to convert sunlight into electricity as efficiently as possible with the simplest synthesis techniques possible. However typically the efficiencies of second-generation solar cells are less than that of the best performing first-generation devices. Examples of commercial thin-film technologies include CIGS ($\text{Cu}(\text{In},\text{Ga})(\text{S},\text{Se})_2$) and CdTe and figure 1.7 shows that the best performing Si devices have higher efficiencies, which are also much closer to their theoretical limit, than these second-generation, thin-film technologies. Third-generation PV technology aims to make use of the low cost fabrication techniques of the second-generation devices but use multiple energy threshold devices to overcome the Shockley-Quiesser limit for a single band gap solar cell, such as in tandem solar cells where semiconductor p-n junctions of increasing band gap are placed on top of each other in order to capture more of the solar spectrum. Typically the more complicated device architecture of third-generation devices result in higher fabrication costs. Research efforts are therefore largely focused on reducing the fabrication cost of multi-junction devices [153].

Current mainstream solar cell technologies, such as first-generation Si wafers and second-generation thin-film CdTe and CIGS solar cells, are unlikely to be able to provide solar electricity at the terawatt scale due to the scarcity of Te and In and the relatively long energy payback time for crystalline Si due to the cost and energy intensive fabrication of Si wafers [154]. Models have even quantified such statements with a predicted In-constrained growth potential of power generation from CIGS PV technology of 20 GW per year in 2020 due to competing applications of In, such as in liquid crystal displays [44]. In order to significantly increase the contribution of solar power to the global power supply, it is therefore necessary to develop more economically viable earth-abundant materials for sustainable PV electricity generation. Furthermore, there must be considerable technological breakthroughs that would enable low-cost manufacturing of highly efficient devices with enough of a cost benefit to outweigh the initial cost outlay in

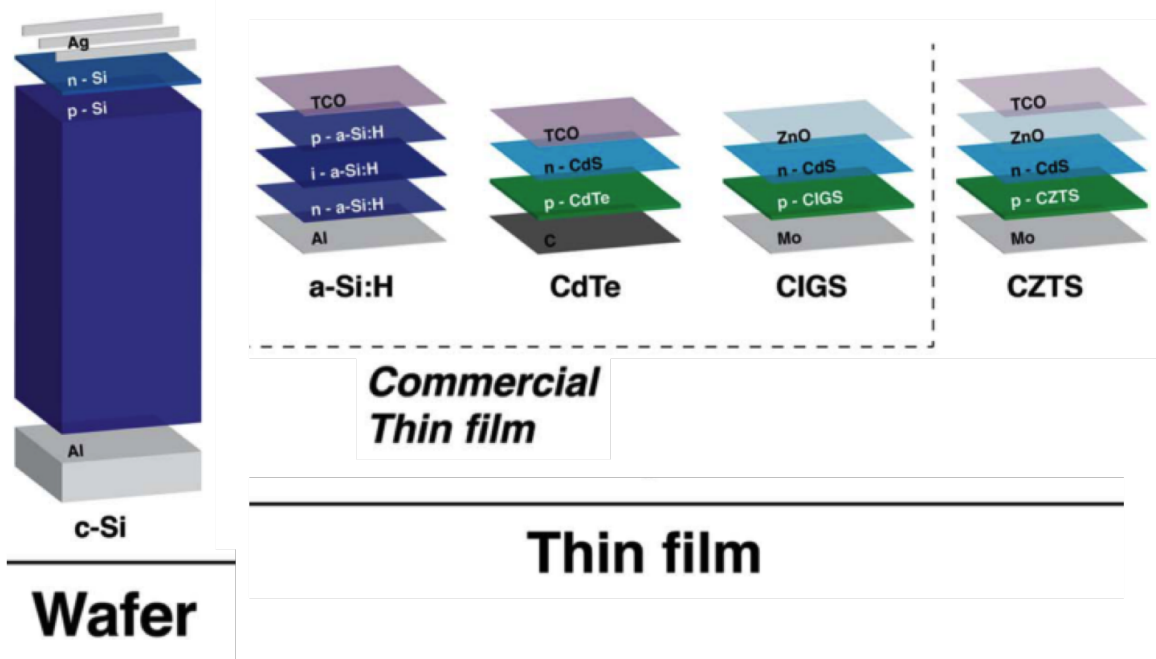


Figure 1.14: Typical structures of a commercial wafer-based PV device (first left) and commercial thin-film photovoltaic devices, as well as a CZTS thin-film device (right). The absorber layers are labelled in white and thickness is shown to scale. Figure adapted from reference 65.

optimizing the manufacturing process of the whole device as has been done for silicon over the past 60 years. For this purpose, there is a drive for solar absorber materials with more optimal properties, such as a direct and sunlight matched band gap (as in thin-film technologies such as CdTe and CIGS), but also for materials that are composed of only earth-abundant components.

1.2 The Role of Computational Modelling in Material Design

The discovery of new functional materials by experimental methods is largely hindered by high costs and time-consuming synthesis procedures [33]. However, with the rapid increase in computational processing power and the availability of large-scale supercomputers, we are entering a very exciting era in computational materials design. There are two main contributions that computational simulations could make towards the technological breakthroughs needed for the development of photovoltaic devices for economically-viable, large-scale solar energy generation. Firstly by predicting properties and screening for certain desirable properties for a solar

absorber material, such as an optimal band gap and high carrier mobility, materials simulations are able to aid in the discovery of new materials for use in photovoltaic devices. Secondly, material simulations are able to provide valuable insight to improve fundamental understanding of known photovoltaic materials to enable the synthesis of better performing devices. In this study we have aimed to make both of these contributions to the field. Firstly, we perform simulations to understand the performance bottlenecks in the candidate earth-abundant, non-toxic solar absorber material $\text{Cu}_2\text{ZnSnS}_4$ (CZTS) and we also study the optical properties of three candidate photovoltaic materials which have so far received little attention as solar materials but could provide another possible route for high-performance photovoltaic devices for cost-effective solar energy generation.

Chapter 2

Bottlenecks of Metal Sulfide Solar Cells

Currently, $\text{Cu}_2\text{ZnSnS}_4$ (CZTS) is one of the most studied candidate earth-abundant thin-film solar cell materials [154]. The potential of CZTS for photovoltaic applications was realised in 1988 by Ito and Nakazawa [64]. The band gap of the material has been predicted [163] and measured [123] to be direct with a value of 1.5 eV, which corresponds to a theoretical conversion efficiency limit of 28% as predicted by Shockley-Quiescer [126]. However, the current record device efficiency is 8.8% [135] and it is believed that this figure must be increased to at least 15% for the devices to be commercially viable [130]. PV devices composed of a CZTS absorber layer are hampered by low open circuit voltage (V_{OC}) [130], which is believed to be due to the formation of secondary phases [12] and defects [28] in CZTS, although the exact origin of the low V_{OC} remains unknown. The first component of this study is therefore an attempt to determine possible origins of this deficit in CZTS.

A number of interesting PV phenomena have been observed in ferroelectric (FE) materials such as the bulk photovoltaic effect (BPE) and the anomalous photovoltaic effect (APE) [25]. Ferroelectric materials usually have a high dielectric constant (which was mentioned in section 1.1.3 as an important parameter for a photovoltaic material) and they possess a spontaneous electric polarization that can be switched between two or more states using an electric field [82]. The BPE was first recorded in 1956 in BaTiO_3 [31], where photovoltages were measured in un-doped single crystals [25]. The BPE effect is distinctly different from the typical PV

effect in semiconductor p-n junctions as it is the polarization electric field that is the driving force for the photocurrent in FE-PV devices [159]. The APE was first observed in PbS films in 1946 [133] and has since been reported in polycrystalline CdTe, ZnTe, InP [66, 50, 144], where photovoltages output along the polarization direction can be significantly larger than the band gap of the material [159], which is usually the limit for a semiconductor PV material [25]. The Shockley-Queisser limit, which prevents any single p-n junction solar cell from converting more than 33.7% of the incident light into electricity, has not been predicted to apply for these photovoltaic phenomena. An upper limit for the theoretical power conversion efficiency (PCE) from this photovoltaic mechanism seems to still be an open question [101], although an ultimate maximum efficiency of any single-band gap absorber of 44% has been set by thermodynamic considerations [126].

The identification, understanding and utilisation of such phenomena may open up the possibility of more efficient PV devices constructed from a number of different photoferroelectric materials. However, most of the commonly used ferroelectric materials such as LiNbO_3 and BaTiO_3 have band gaps larger than 3 eV and can therefore only absorb sunlight in the UV range to convert into electricity, which accounts for only around 3.5% of the solar spectrum [159], which was shown in figure 1.6. Research efforts have also gone into adjusting the optical absorption of ferroelectric materials without influencing the ferroelectric properties of the material through chemical doping or alloying [159]. In $\text{Bi}_4\text{Ti}_3\text{O}_{12}$ (BiT) the optical band gap has been tuned in such a way, resulting in a decrease from 3.6 eV to 2.7 eV [30], although this is still considerably larger than the optimal range of 1.06 eV and 1.50 eV [63] for a PV absorber material.

This then leads on to the second component of this study, which is an investigation of the optoelectronic properties of new candidate solar absorber materials that may also exhibit ferroelectricity, but have band gaps within the optimal range for the absorption of sunlight. In theory, these materials could exhibit novel photovoltaic phenomena such as the anomalous and bulk photovoltaic effects to overcome the Shockley-Queisser efficiency limit without the need for such complicated device architectures as in third-generation tandem solar cells. Although the difference between the Shockley-Queisser limit and the ultimate thermodynamic limit of a solar material is not enormous, it is also possible that ferroelectric materials have properties

that enable more efficient devices to be made more easily, such as good screening of defects due to high dielectric functions or enhanced electron-hole separation from ferroelectric domains resulting in reduced recombination and a higher performance solar cell with ‘low quality’ defective and nanostructured materials [24]. Such technologies could provide one possible route for the technological breakthrough for economically-viable, large-scale solar energy generation.

2.1 Possible Performance Bottlenecks of $\text{Cu}_2\text{ZnSnS}_4$ Devices

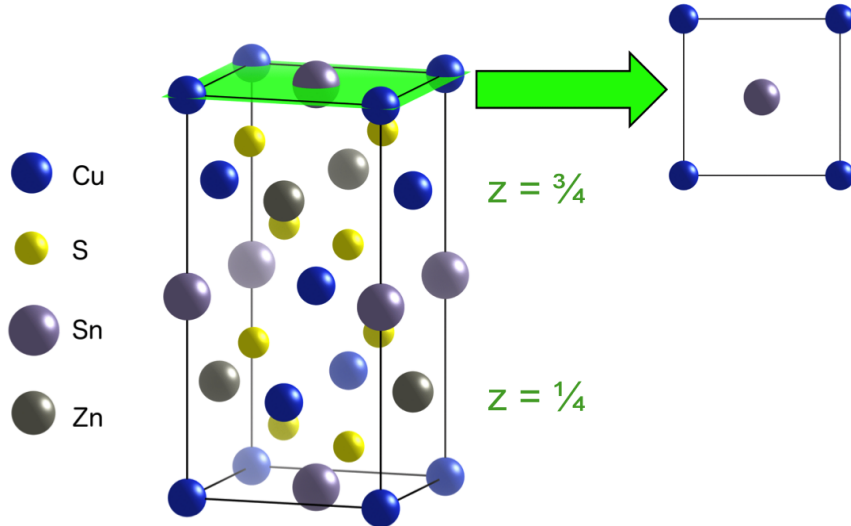


Figure 2.1: The conventional unit cell of CZTS ($\text{Cu}_2\text{ZnSnS}_4$) with the ground-state kesterite crystal structure (space group $I\bar{4}$). The structure consists of alternating layers of Cu-Sn and Cu-Zn where Cu-Zn layers are at $z=\frac{1}{4}$ and $z=\frac{3}{4}$.

The ground state crystal structure of CZTS ($\text{Cu}_2\text{ZnSnS}_4$) is kesterite (space group $I\bar{4}$). The conventional unit cell of CZTS is shown in figure 2.1, where each S is surrounded by two Cu, one Zn, and one Sn to satisfy local charge neutrality and the valence-octet rule. Kesterites meet two necessary conditions for highly efficient solar cells, which are a band gap that is both direct and relatively well-matched to the solar spectrum [63]. Over the last decade the power conversion efficiency of PV devices based on kesterite, $\text{Cu}_2\text{ZnSn}(\text{S}_x\text{Se}_{1-x})_4$ (CZTSSe), compounds has improved greatly from around 5% in 2004 to 12.6% in 2013 [1]. However, this

is still far from the record efficiencies of $\text{Cu}(\text{In}_{1-y}\text{Ga}_y)\text{Se}_2$ (CIGSe) devices of >20%, where the materials have very similar band gaps to those of CZTSSe [22] and so should have the same theoretical efficiency limit as predicted by Shockley and Queisser [126]. Furthermore, the rate of improvement seems to have slowed considerably recently with the last improvement in efficiency being reported in 2014 and with only a 0.1% improvement [69]. A large number of possible explanations have been proposed to explain the current difference in efficiency between CZTSSe and CIGSe devices, many of these are illustrated in figure 2.2. The majority of studies converge towards the low open circuit voltage (V_{OC}) relative to the band gap, i.e. the V_{OC} deficit, being the main limiting factor on device performance. As can be seen from the position of CZTSSe devices on the plot in figure 2.3, the open circuit voltages measured for these devices are considerably less than that of a CIGS device, which has a similar value for the band gap of the material.

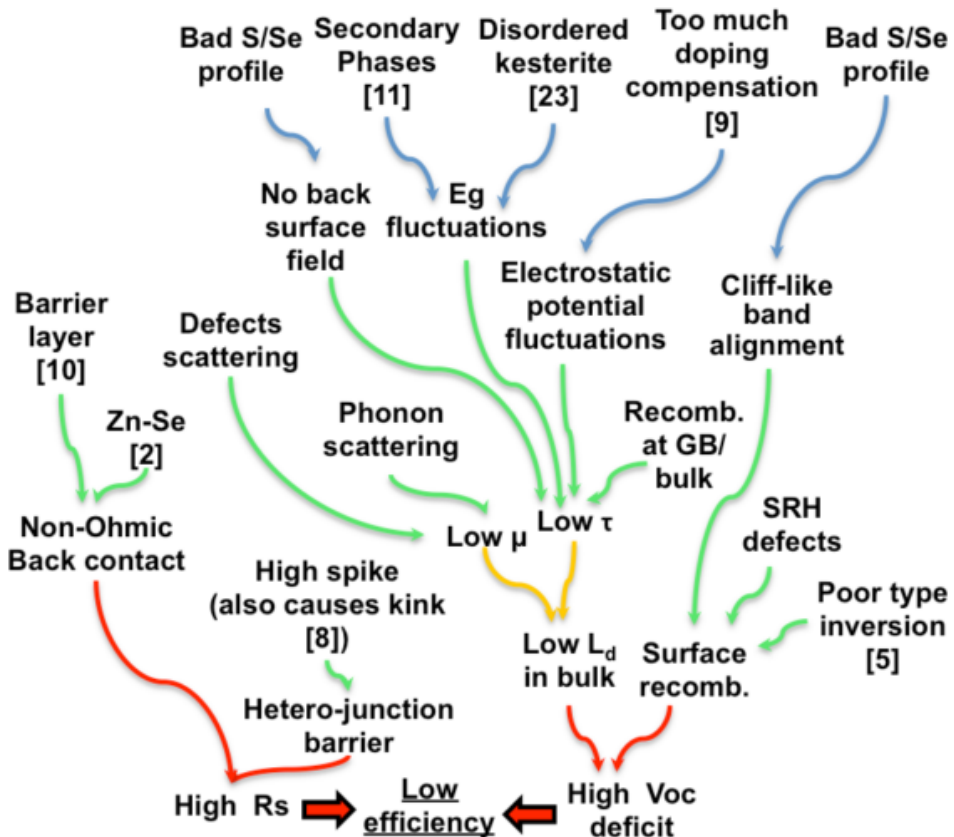


Figure 2.2: Mapping of the numerous possible mechanisms limiting the efficiency in kesterite devices and their possible causes. R_s is the series resistance between the absorber layer and back contact of the device and V_{OC} is the open circuit voltage across the absorber layer. Figure taken from 32.

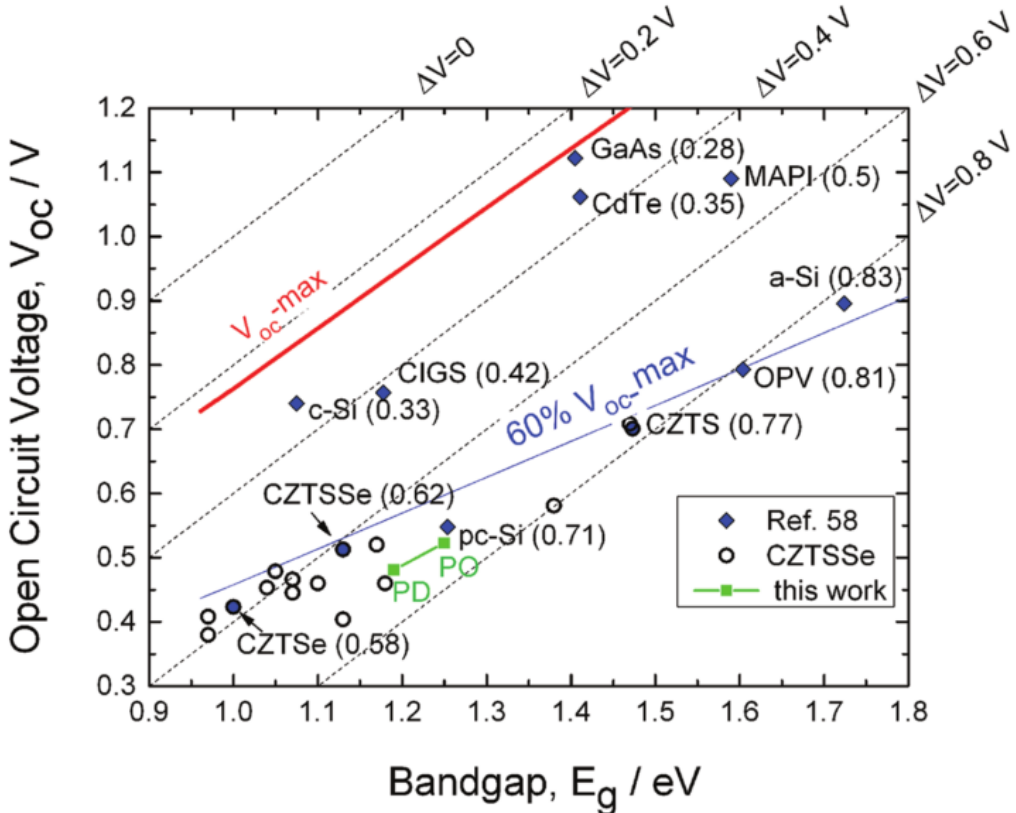


Figure 2.3: V_{OC} versus band gap of high performance CZTSSe devices (>9% efficiency) indicated by circles with best devices based on other photovoltaic materials shown for comparison by diamond symbols: Methyl-ammonium lead iodide (MAPI), amorphous silicon (a-Si), organic photovoltaic films (OPV), crystalline silicon (c-Si) and polycrystalline silicon (pc-Si). The oblique lines give a constant V_{OC} deficit from 0.8 V to 0 V. The green points correspond to CZTSSe films that are partially ordered (PO) or partially disordered (PD) due to disorder amongst Cu and Zn. Figure take from reference 22.

As figure 2.2 shows, there are many different possible causes of the V_{OC} deficit in kesterite solar cells. Developing fabrication techniques to reduce the deficit is therefore an even greater challenge when the exact cause is not yet known. This is an area in which computational materials simulations should be able to provide valuable insight to help pinpoint the specific sources of the V_{OC} deficit in kesterite solar cells. The true power of simulation is the ability to take a perfect system and introduce various imperfections one at a time and then study the effect that particular imperfection could have on device performance. As opposed to in a real system in which there is a myriad of possible causes for each observation, as illustrated in figure 2.2. In our simulations we will start from the most simple system possible, before making any attempts to build up in complexity. Devices made from a compound of $\text{Cu}_2\text{ZnSnS}_4$ and

$\text{Cu}_2\text{ZnSnSe}_4$, i.e. $\text{Cu}_2\text{ZnSn}(\text{S}_x\text{Se}_{1-x})_4$, so far have given the best performing devices, however in this study we are currently focusing on just the pure sulfide material, CZTS. In addition to simplifying the system, figure 2.3 also indicates that the V_{OC} deficit is worse in purely CZTS devices and so potentially studying causes of the problem in this particular system could be more informative. Also although ultimately the aim is to make thin-film devices from CZTS, in which the material is likely to be highly polycrystalline with many grain boundaries, we are currently just focusing on the bulk material. We are doing this for two reasons. Firstly to improve the understanding of the fundamental material properties before attempting to understand a more complex system to ensure that we start from a solid foundation. Secondly, it has been proposed that the V_{OC} deficit in CZTSSe devices could actually be largely due to the natural bulk properties of the crystal [110]. For the purposes of our study therefore measurements performed on single crystals will be the most directly relatable to our findings, wherever the data is available.

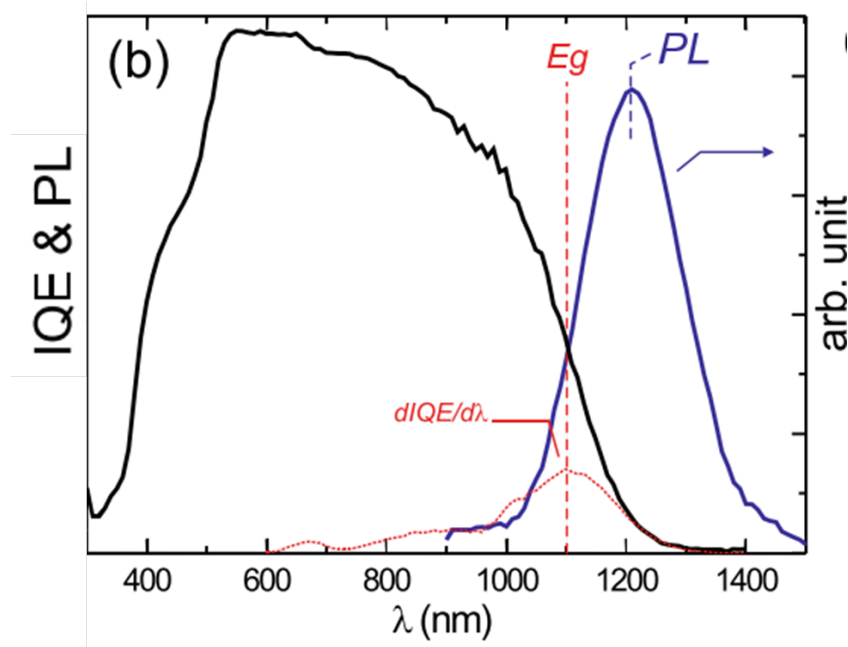


Figure 2.4: Internal quantum efficiency (IQE) and photoluminescence (PL) spectra of CZTSSe thin-films showing the shift of the PL peak to energies below the band gap of the material. Figure taken from reference 49.

In general, the main cause of V_{OC} deficit in a PV device is the recombination of photogenerated charge carriers in the bulk material or at surfaces [22]. Figure 2.4 shows photoluminescence (PL) spectroscopy measurements performed on CZTSSe thin films by Gokmen et al [49]. The

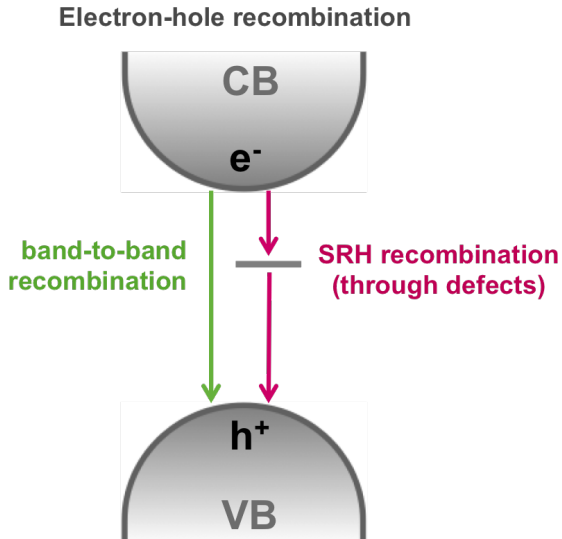


Figure 2.5: Illustration of Shockley-Read-Hall (SRH) electron-hole recombination due to energy states introduced into the band gap by defects.

emission spectra of semiconductors is discussed much more thoroughly in section 3.3.1 and a review of various PL studies performed on kesterite thin films and crystals is given in section 3.3.3, but for current purposes the key observation to be made from figure 2.4 is that there is a shift in the PL peak to lower energies (red-shifting), below the value of the band gap obtained from internal quantum efficiency (IQE) measurements performed on the same thin films. It is also noted in this study when comparing the PL spectra of CZTSSe films to that of CIGSSe films that the PL peak for CZTSSe thin films is broader and that the red-shifting was roughly twice as severe. This effect is referred to as ‘band-edge tailing’, where photons of energies less than the band gap of the material are emitted following photoexcitation and subsequent relaxation back to the ground state. This effect is known to be detrimental for device performance as emitted photons may then not have sufficient energy for subsequent photoexcitations in the absorber layer, the energy of the original photon may then not be converted into electricity if the photoexcited electron-hole pair recombine before the charge is collected [91]. Band tailing and the possible causes of this detrimental effect are discussed further in section 3.3.2, but for now it is worth briefly noting that possible causes are: Shockley-Read-Hall recombination due to defect-induced mid-gap states [127], as illustrated in figure 2.5, as well as fluctuations in electrostatic potential due to the presence of charged defects leading to rigid shifts in the band edges and fluctuations in the band gap of the material due to an inhomogeneous composition

[49], which are both shown in figure 2.6.

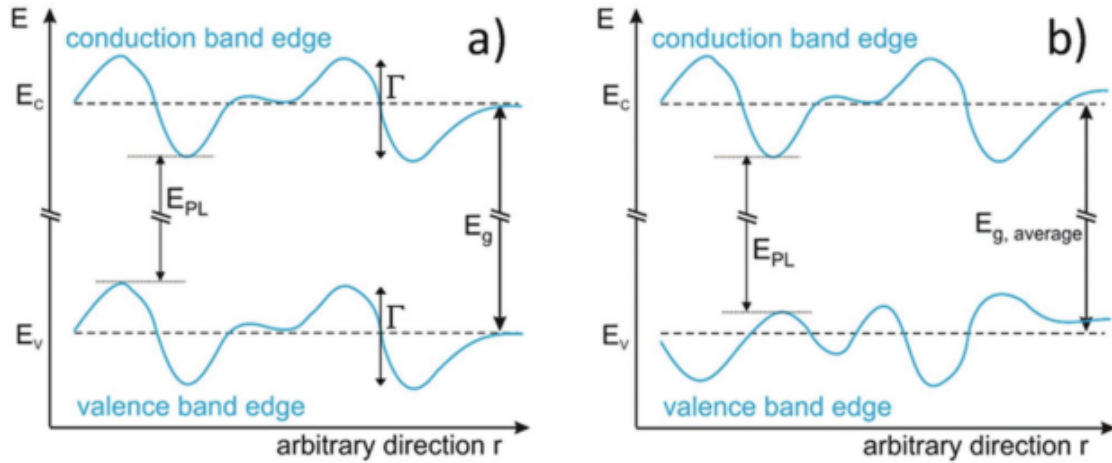


Figure 2.6: The effect of electrostatic potential fluctuations (a) and band gap fluctuations (b) on the electronic bands of a semiconductor. In both cases radiative transitions at energies below the (average) band gap are possible. The band gap in (a) is constant and not affected by local charged defects, while band edges in (b) can differ depending on e.g., long range composition variations. Figure taken from reference 22.

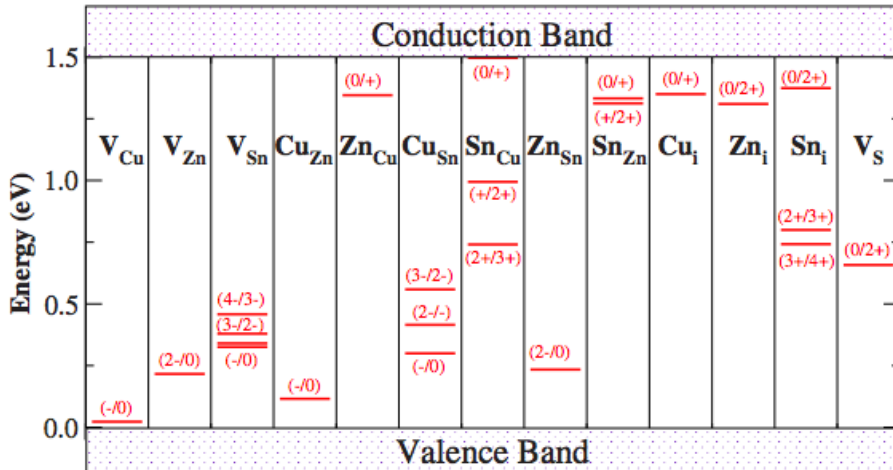


Figure 2.7: The transition-energy levels of intrinsic defects in the band gap of $\text{Cu}_2\text{ZnSnS}_4$ where the GGA band gap has been corrected to the experimental value 1.5 eV, and the donor levels are shifted together with the conduction band minimum (CBM) level. Figure taken from reference 29.

The extent of band tailing due to the additional energy levels introduced into the band gap of a material by particular intrinsic defects is dependent upon the concentration of those particular defects. The equilibrium defect concentration can be obtained directly from the defect formation energy [94], which is discussed in Appendix A. For materials such as CZTSSe that are still at

a fairly early stage of development, theoretical predictions of defect formation energies may be the only values available to help identify specific defects and their properties in real systems [71]. Theoretical predictions for the formation energies and depth of defect-induced energy levels for various intrinsic point defects and defect clusters in CZTS were made by Chen et al [29]. Figures 2.7 and 2.8 show the predicted depth of defect levels for intrinsic point defects and defect clusters respectively. Based on the predictions made by Chen et al, figure 2.7 shows that many of the intrinsic defects involving Sn would induce a mid-gap state, however in the same work the authors predict that the formation energy of those particular defects would all be expected to be high. It therefore would be expected that these defects are less likely to form and should be present in lower concentrations than other defects. Although other works have suggested that the formation of this defect could be more likely if it is forms part of a particular defect cluster [150, 22]. From the work by Chen on defect clusters, it is also expected that certain charge compensated defect clusters would have very low formation energies, in particular the $[Cu_{Zn}^- + Zn_{Cu}^+]$ antisite defect pair.

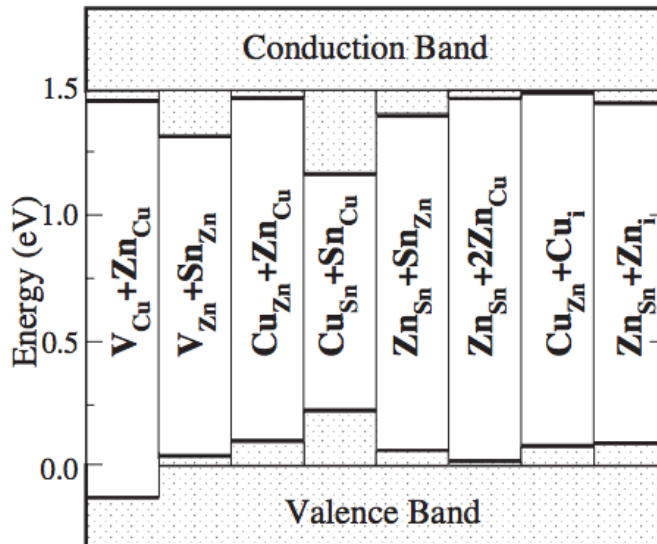


Figure 2.8: The conduction band minimum (CBM) and valence band maximum (VBM) levels in eV of Cu_2ZnSnS_4 with different charge-compensated defect complexes relative to the host material at 0 eV and 1.5 eV respectively. Figure taken from reference 29.

Disorder amongst Cu and Zn ions (or equivalently the formation of the $[Cu_{Zn}^- + Zn_{Cu}^+]$ antisite defect pair) in CZTS has been proposed as one possible origin of the V_{OC} deficit in CZTS and consequently a number of experimental studies have been conducted to investigate this

[122, 120, 40, 119]. Additionally it is worth noting that this substitutional disorder does not exist in the crystal structure of CIGSe due to the considerably larger chemical mismatch between Cu with In or Ga [22], whereas Cu and Zn are so similar that disorder between the two species can be difficult to detect experimentally. As Cu and Zn are neighbouring elements in the periodic table, the changes in the bonding between the two are subtle [87]. This results in a theoretical energy difference between the two structures of just 3 meV per atom [27] allowing for intermixing of the Cu and Zn cations in CZTS, which has been confirmed by neutron diffraction [120, 40] and also measured using near resonant raman scattering [122]. However, a recent work prepared samples with varying degrees of Cu-Zn disorder (by varying the annealing treatments during synthesis, which had been shown in a previous study to have a considerable effect on Cu-Zn ordering in CZTS [122]) and in this work they showed that a reduction in Cu-Zn order resulted in a reduction in both the band gap and V_{OC} , thereby not influencing the V_{OC} deficit relative to the band gap of the material [22].

In this present work we focus mostly on the extent of band tailing in CZTS to be expected from disorder amongst Cu and Zn ions. We simulate thermodynamic substitution amongst Cu and Zn ions in CZTS and study the resulting changes in the distribution of electrostatic potential in the system. As discussed above, disorder amongst Cu and Zn ions has not only be predicted to be very likely based on energetics but has also been observed experimentally, it would therefore be important to know if this particular type of disorder is having a detrimental effect on device performance or to at least eliminate it from the list of many possible causes of the V_{OC} deficit.

2.2 Predicting the Properties of New Candidate Solar Absorber Materials

The primary aim of our studies on the solar absorber material CZTS is to determine if device performance is being hindered by bulk defects and the fundamental properties of the material. It is possible that there are other materials with properties that are much more suited to applications in PV. The second part of this study involves using materials modelling to predict the

optoelectronic properties of materials that could have the potential to be used to produce high performance PV devices, but until now have received little research interest for applications in PV. The central idea in selecting these candidate materials was to identify any that may be ferroelectric and so could exhibit some of the novel FE-PV phenomena discussed earlier but may also have a band gap within the optimal range for solar absorption. Photoferroelectric, or photoferroic, is the name given to materials that exhibit such properties. Using very simple screening criteria, we identified three candidate photoferroelectric solar absorber materials from a data set of over 200 naturally occurring minerals. A dark-coloured material suggests (but does not guarantee) that it absorbs light in the visible range. Ferroelectric materials are a subset of materials with polar crystal structures, therefore not all polar materials exhibit ferroelectricity. It is only polar materials that also possess a spontaneous electric dipole moment within the unit cell which can be inverted by the application of an external electric field that exhibit ferroelectricity [34]. Therefore, the conditions used to screen for candidate photoferroelectric materials shown in the Venn diagram in figure 2.9 are necessary conditions for photoferroelectricity, but cannot guarantee that the materials will exhibit this phenomena. The three candidate photoferroelectric materials identified by our screening process were: enargite (Cu_3AsS_4), stephanite (Ag_5SbS_4) and bournonite (PbCuSbS_3). All three minerals are sulfosalts, which are materials that contain two or more metals, semi-metals such as antimony and arsenic, and sulfur [20].

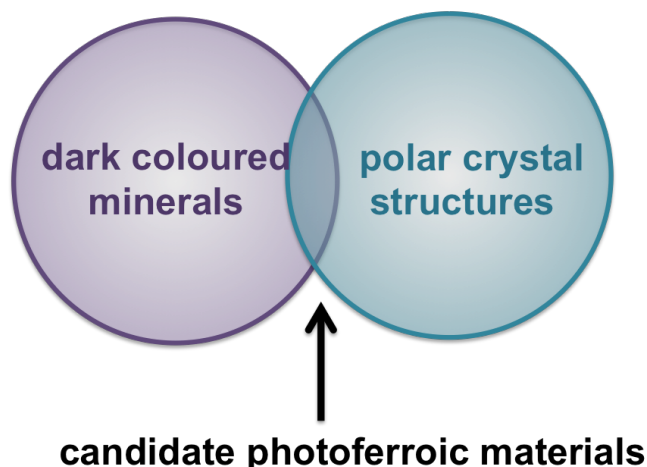


Figure 2.9: Venn diagram showing the necessary (but not sufficient) conditions for a material to exhibit photoferroelectricity, where the dark colour suggests absorption of light in the visible range and a polar crystal structure is a requirement (but does not serve as a guarantee) for a material to exhibit ferroelectricity.

Scientific research on sulfosalts has largely focussed on the thermodynamic properties and crystal structure of the minerals, leaving knowledge of the optoelectronic properties of sulfosalts relevant for PV applications extremely scarce. The potential of sulfosalt minerals for PV applications however was highlighted by Dittrich et al in 2007 [35]. This work also provides an overview of thin film deposition methods that have been developed for synthesizing sulfosalt layers and discusses a 1% efficient Sn-Sb-S sulfosalt thin film solar cell constructed by the authors. The potential of the sulfosalt mineral enargite for PV applications has been suggested even earlier by Pauperté and Lincot in 1995 [103]. In addition to the development of synthesis methods, another important consideration for the large-scale deployment of solar devices composed of the candidate materials is the price and abundance of the elemental components. Figure 2.10 shows a comparison of the price and abundance of some of the elemental components of the three candidate materials: Cu, Sb and S, to that of elements used in some current commercial thin film solar cell absorber materials such as CuIn(Ga)Se₂ (CIGS) and CdTe. The components of the candidate materials not included in the figure are As, Pb and Ag. Lead can be considered as the most abundant and universally diffuse metal after iron. Although it is never found in the native state, its ores are very numerous [137]. 5,200,000 tonnes of lead was produced in 2012 [143], although its crustal abundance is considerably smaller than that of iron being around 10-14 ppm compared to approximately 60,000 ppm for iron [121]. Silver and arsenic are both fairly abundant metals. Silver often occurs in combination with lead, copper, iron, antimony and tellurium. Arsenic is also present in most ores of silver [137]. The crustal abundance of arsenic is approximately 1.5 ppm and that of silver is relatively low at approximately 0.070 ppm [121]. These values are however still larger than that of indium (0.049 ppm [121]), which is also in demand for the display industry [130].

The first candidate photoferroelectric material, enargite (Cu_3AsS_4), is frequently found as an impurity in copper ores [146]. It is a mineral that corresponds to a semiconductor of type $A_3^I B^V C_4^{II}$. The unit cell (as shown in figure 2.11a) has an orthorhombic crystal structure with space group $Pmn2_1$ and tetrahedral coordination for all atoms [128]. The main impurities in natural enargite are Sb and Fe, but Pb and Ag are also known to be present to some extent [146]. Natural samples of enargite have been found to exhibit the electrical properties of a p-type

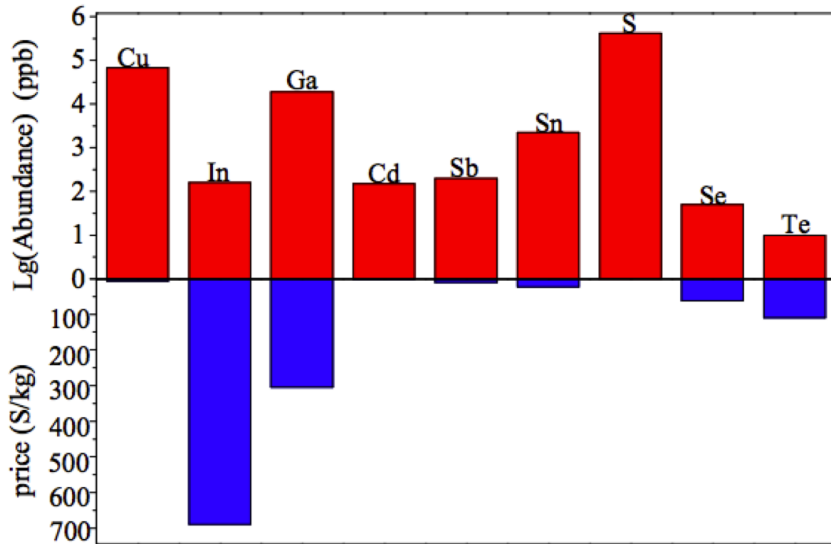


Figure 2.10: Comparison of element abundance and price between Cu, In, Ga, Cd, Sb, Sn, S, Se and Te. Figure taken from the supporting information of reference 155, where data was taken from the London Metal Exchange LME.

doped semiconductor with a conductivity of 0.0014 S/m (from the stated value of approximately $7 \Omega \text{ cm}$ for the resistivity at 295 K) [103]. In the same work, two optical transitions were determined: an indirect one at 1.19 eV and a direct one at 1.44 eV. Although more recent studies have given a value of 1.28 eV for the band gap of enargite from measurements of temperature dependent resistivities, diffuse reflectance spectroscopy and photoacoustic spectroscopy [36]. A theoretical study using the first principles quasi-particle GW method based on wavefunctions generated from the hybrid functional HSE06 [56], has predicted a value of 1.32 eV for the band gap [156]. Although a number of different values have been reported for the band gap of enargite, all values stated fit within the optimal range of 1.06 eV to 1.50 eV [63] for a solar absorber material.

The unit cell of the second candidate photoferroelectric material, stephanite (Ag_5SbS_4), also has an orthorhombic crystal structure but with space group $Cmc2_1$, and is shown in figure 2.11b. The structure is composed of columns of SbS_3 pyramids extended along the z axis. The columns are located pairwise; in each column, pyramids occupied with antimony atoms alternate with empty pyramids. The Sb-S distances in the pyramids are 2.48, 2.42, and 2.42 Å. Silver atoms are located in the tetrahedral coordination between SbS_3 groups (at the centers

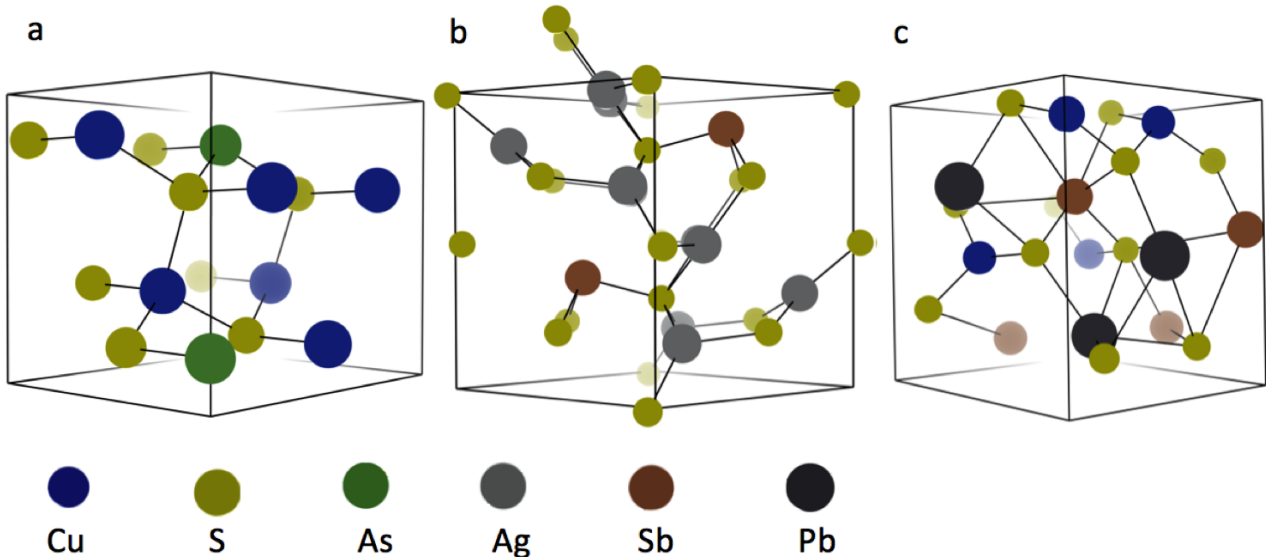


Figure 2.11: The 15 atom primitive unit cell of enargite (Cu_3AsS_4) (a), 19 atom primitive unit cell of stephanite (Ag_5SbS_4) (b) and 23 atom primitive unit cell of bournonite (PbCuSbS_3) (c).

of rhombic channels). Three types of AgS_4 tetrahedra with different Ag-S distances can be identified. The distinctive feature of the structure is a large number of common edges of Ag tetrahedra [100]. It has been reported that stephanite has a band gap of 1.62 eV [36]. Otherwise, there is seemingly very little information available in the literature on the optical or electrical properties of stephanite apart from a work in 1973, given in reference 26, showing the electrical resistivity of a synthetic sample of stephanite as a function of temperature. The work measures a resistivity of approximately $9 \Omega \text{ cm}$ for the stephanite sample at 110°C , which corresponds to a conductivity of 0.0011 S/m. There has also been some speculation in the literature on the possibility of ferroelectric behaviour in stephanite due to the presence of ferroelectric phases at very low temperatures in pyrargyrite (Ag_3SbS_3), proustite (Ag_3AsS_3) and stibnite (Sb_2S_3), which are crystallochemically related to stephanite [100]. The same study also notes that similar displacement structural changes occur in stephanite to those in proustite and pyrargyrite that are responsible for the ferroelectric properties of these materials.

Similarly, up until very recently, little information has been available on the optical or electrical properties of the third candidate photoferroelectric material, bournonite (PbCuSbS_3). Bournonite also has an orthorhombic crystal structure and the same space group as enargite, $Pmn2_1$, with measured values of 1.23 eV [36] and 1.31 eV [149] reported for the band gap.

Table 2.1: Summary of known key properties of the three candidate photoferroelectric materials from the literature.

Candidate	Empirical Formula	Space Group	Band Gap (eV)	Conductivity (S/m)
Enargite	Cu_3AsS_4	$Pmn2_1$	1.28 [36]	0.0014 [103] ⁱⁱ
Stephanite	Ag_5SbS_4	$Cmc2_1$	1.62 [36]	0.0011 [26] ⁱⁱ
Bournonite	PbCuSbS_3	$Pmn2_1$	1.23 [36], 1.31 [149]	-

ⁱ From resistivity of a natural sample measured at 295 K

ⁱⁱ From resistivity of a synthetic sample measured at 383 K

However, very recently this material has received increasing scientific interest for thermoelectric and rewriteable data storage applications due to a measured low thermal conductivity [37]. Consequently, works on the synthesis of bournonite are beginning to emerge such as that in reference 149. The low thermal conductivity of bournonite has been attributed to the distortive environment of the Pb and Sb atoms from the stereochemically active lone-pair s^2 electrons [37]. In the same study they perform electronic structure calculations to predict the band structure of the material, however in the study they use only the generalized-gradient approximation (GGA) level of accuracy in density functional theory for their calculations, which is known to underestimate the band gap of a semiconducting material. They do however show that the inclusion of spin-orbit coupling (SOC) has a considerable impact on the calculated band gap of the material. In the study they predict a direct band gap of 0.686 eV before including SOC and two optical transitions when they do include SOC: a direct band gap of 0.445 eV and an indirect band gap of 0.385 eV. A more recent study has made use of DFT+U methodology to avoid the underestimation of the band gap when calculating the optoelectronic properties of this material, where they predicted a band gap of 1.22 eV [134]. There was however no mention of SOC in the study, which was shown in the previous study to influence the band structure of the material considerably.

The key known experimentally derived properties of the three candidate materials that were described above are summarised in table 2.1. In this study we aim to use the highest level of theory possible to predict many of the properties relevant for a solar absorber material that were discussed in section 1.1.3 for the three candidate PV materials. Although these materials were originally selected based on the possibility of exhibiting ferroelectricity, for now the study

is just focused on the optoelectronic properties that are directly relevant for predicting the performance of these materials in a photovoltaic device. Firstly we use hybrid-DFT electronic structure calculations to optimize the crystal structure of a bulk system, starting from the highest quality X-Ray diffraction data available for the materials. From this we calculate the band structures of the materials to determine the size of the band gap and whether it is direct or indirect in nature as this would be a good indicator of how strongly the materials will absorb sunlight. This particular investigation is one of the areas discussed later as future work in section 5.2.

Chapter 3

Background Theory

3.1 Models of Perfect Periodic Crystal Structures

Theoretical models of crystalline solids are based around the existence of translational symmetry in a crystal lattice such that the lattice can be constructed by periodically repeating a unit cell of atoms. The Bravais lattice specifies the periodic array in which the repeated units of the crystal are arranged. A crystal lattice can therefore be described by its underlying Bravais lattice and the arrangement of atoms, ions or molecules within a particular unit cell, i.e. the basis [5]. This principle is used in a number of ways during this study. Firstly, this process is performed on a finite scale to construct a 64 atom supercell of CZTS from the 8 atom primitive unit cell for use in density functional theory (DFT) calculations to predict defect formation energy. The principle is also used in all DFT calculations of solid state systems through the implementation of periodic boundary conditions to simulate an infinite, bulk system using only a finite unit cell.

Another important concept in the theoretical modelling of periodic structures is reciprocal space and the reciprocal lattice. Converting to reciprocal space enables the description of periodic features with a longer-range periodicity than the unit cell in real space, such as the motion of electrons in a crystal and phonons. In the same way that any quantity that varies with time can be described as a sum of Fourier components in the frequency domain; the spatial properties of a

crystal can be described as a sum of components in Fourier space, otherwise known as reciprocal space or k -space. The reciprocal lattice of a perfect single crystal is an infinite periodic 3D array of points whose spacings are inversely proportional to the distances between the planes in the lattice in real space. Vectors in real space have dimensions of length, whereas vectors in reciprocal space have dimensions of length $^{-1}$. This can therefore be compared directly to the wavevector ($k = \frac{2\pi}{\lambda}$) of an excitation such as a phonon or a moving electron and multiplication of each coordinate of the reciprocal lattice by \hbar converts reciprocal space into momentum space as for a quantised wave $\mathbf{p} = \hbar\mathbf{k}$ [15].

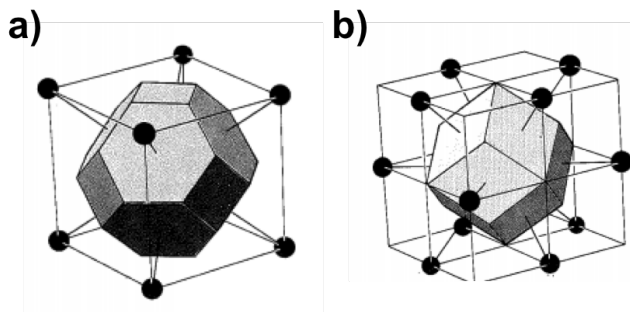


Figure 3.1: The Wigner-Seitz cell for the body-centred cubic Bravais lattice where there is a lattice point at its centre and on each vertex. The hexagonal faces bisect the lines joining the central point to the points on the vertices. The square faces bisect the lines joining the central point to the central points in each of the six neighbouring cubic cells. Figure taken from reference 5.

The Wigner-Seitz primitive cell is the most common choice of primitive cell with the full symmetry of the Bravais lattice. It represents the region of space around a lattice point that is closer to that point than to any other lattice point. For example, figure 3.1a shows the truncated octahedron that is the Wigner-Seitz cell for a body-centred cubic (bcc) lattice [5]. The first Brillouin zone is the Wigner-Seitz primitive cell of the reciprocal lattice. The reciprocal of the bcc lattice is face-centred cubic (fcc), therefore the first Brillouin zone of the bcc lattice is the fcc Wigner-Seitz primitive cell as shown in figure 3.1b [6]. As the full symmetry of the reciprocal lattice is contained within the first Brillouin zone, it is only necessary to sample k -points within this single unit cell of the reciprocal lattice when calculating the electronic ground state of a periodic structure.

3.2 Band Theory & Band Structure of Semiconductors

The band theory of solids provides a means to explain the difference in the electrical conductivity of conductors, semiconductors and insulators. Electrons bound to an atom have a number of possible discrete energy levels. When a large number of atoms are brought together to form a solid, it becomes impossible to assign individual electrons to individual atoms. Instead, the electrons are considered to be shared amongst the atomic nuclei. However, a consequence of this sharing would be a large number of electrons occupying the same energy state, which violates the Pauli Exclusion Principle. The original discrete energy levels therefore are broadened into bands. The new energy levels are so closely spaced that they are considered to be a quasi-continuous band of allowed energies. This is illustrated in figure 3.2. The series of bands of allowed energies in a semiconductor or insulator are separated by bands of forbidden energy, known as the band gap, E_g , of the material [160]. In the simplest model, the upper energy band (the conduction band) is separated from the lower energy band (the valence band) by a constant band gap, which was discussed in section 1.1.3 for the important role this optical property has in a solar absorber material. This is called the flat band model and is often shown in schematics of p-n junctions for PV devices, such as in figure 1.4. In real structures, the band architecture is more complicated than this simple model, like the band structures shown in figure 1.8 [136].

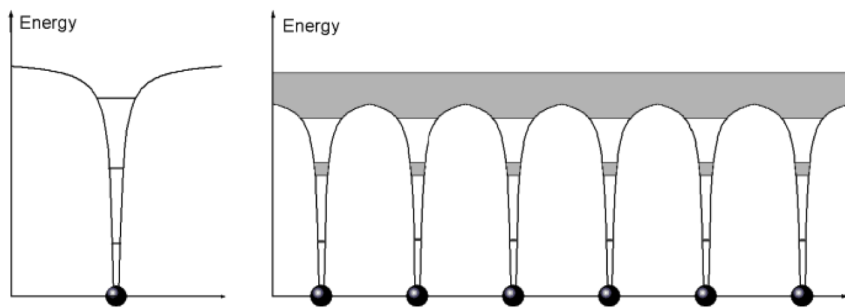


Figure 3.2: Electron energy levels of a single atom (left) and the formation of a quasi-continuous band of allowed energies in a solid crystal when many atoms are brought close together (right). Figure taken from 109.

The concept of the energy band model of a solid emerges from considering the behaviour of electrons in a periodic crystal lattice, but cannot be understood in terms of classical physics

alone. Instead, the electron must be considered in terms of wave-mechanical terms as a wave propagating in a periodic structure with diffraction and interference effects [67]. In the band theory of solids, the energy of a single electron in a perfect crystal is described by the one-electron Schrödinger equation, shown in equation 3.1. The first term in equation 3.1 is the kinetic energy of the electron, $V(\mathbf{r})$ is the effective non-zero periodic potential energy experienced by the electron in the crystal, ψ is the electron wavefunction and ϵ is the eigenenergy of the electron. In band theory, it is assumed that for any electron, everything else in the crystal can be represented by the effective potential energy, $V(\mathbf{r})$ [16].

$$\left[\left(-\frac{\hbar^2}{2m} \right) \nabla^2 + V(\mathbf{r}) \right] \psi = \epsilon \psi \quad (3.1)$$

The spatial dependence of the potential experienced by an outer electron in a crystal for multi-electron systems was considered by Felix Bloch. He determined that the total potential is the sum of two parts. Firstly, the electrostatic potential due to the array of atomic cores. For a perfect lattice this should have the translational periodicity of the lattice. Secondly, the potential due to all other electrons. Bloch assumed that the charge density would have the same long-term average value in every unit cell of the crystal and therefore would be periodic. Bloch's theorem states that the wavefunction which satisfies equation 3.1 subject to a periodic potential should be of the form shown in equation 3.2, where $U_k(\mathbf{r})$ is some function (depending on the value of the wavevector, \mathbf{k}) that also has the complete periodicity of the lattice and \mathbf{k} is confined to the first Brillouin zone [16].

$$\phi_k(\mathbf{r}) = U_k(\mathbf{r}) e^{i\mathbf{k}\cdot\mathbf{r}} \quad (3.2)$$

$$\psi_k(\mathbf{r}) = \sum_k A_k \phi_k(\mathbf{r}) = \sum_k A_k U_k(\mathbf{r}) e^{i\mathbf{k}\cdot\mathbf{r}} \quad (3.3)$$

Due to the translational symmetry of a crystal lattice, an eigenfunction of the one-electron Schrödinger equation can be expressed as a sum of Bloch functions such as that shown in equation 3.2, as shown in equation 3.3. The one-electron wavefunctions therefore can be indexed by constants \mathbf{k} , which are the wave vectors of the plane waves forming the ‘backbone’ of the Bloch function. A plot of the electron eigenenergies from equation 3.1 versus \mathbf{k} is known as the

electronic band structure of the crystal [158].

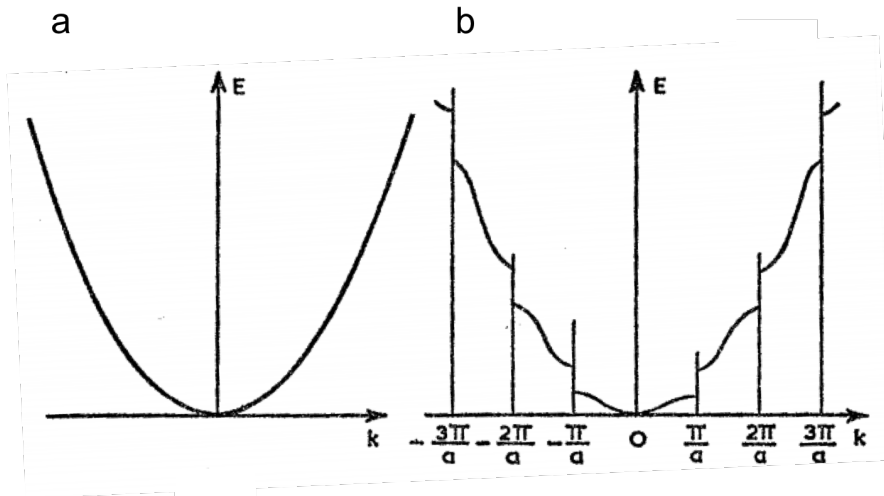


Figure 3.3: Energy-wave vector diagrams: (a) the free electron parabola, (b) modification due to a periodic crystal lattice. Figure taken from reference 67.

The introduction of a medium with a discrete structure, such as a crystal lattice, has a profound effect on the dispersion relation of the waves. The energy dispersion relation of a free electron and that in a periodic crystal lattice is shown in figure 3.3. A periodic medium does not completely suppress the propagation of waves, as would be expected in disordered or amorphous structures, but they do however introduce limiting frequencies and wavelengths for the propagation, followed by cut-off regions. The lower limit of the wavelength is set by the lattice spacing, a , giving an upper limit of the wave vector, \mathbf{k} , of $\frac{\pi}{a}$. As figure 3.3 shows, the parabola of the free electron is modified in a periodic crystal by the introduction of discontinuities at values of \mathbf{k} corresponding to multiples of $\frac{\pi}{a}$. The appearance of such energy gaps implies that electrons in a periodic crystal may only have kinetic energies corresponding to certain bands, whilst being free to propagate in the lattice [68].

A useful concept used to simplify the dynamics of an electron in a crystal lattice in the band theory of solids is that of effective mass, which was first mentioned in section 1.1.3 as a key material property for a solar absorber material. The effective mass is a convenient parameter which accounts for the influence of a periodic lattice on a free carrier, enabling an electron in a periodic crystal to be treated as though it were a free particle but with a different mass in calculations of charge transport. Values of effective mass in semiconductors usually vary

between 0.01 and 1 times the mass of a free electron and it is determined by the curvature of the energy graph in k -vector space [68]. The effective mass is a parameter that can influence the efficiency of a solar cell, in particular, the effective mass of holes in the valence band and electrons in the conduction band (i.e. minority charge carriers) are of interest. The mobility of charge carriers is inversely proportional to the effective mass and the mobility of charge carriers in a PV material is important for efficient charge collection [11].

3.3 Electronic Properties of Defects in Semiconductors

Although the main framework for materials modelling of solid-state systems (as was outlined in section 3.1) is built around perfect, periodic systems; in reality absolutely perfect systems do not exist. There is an energy cost associated with the creation of a defect, but in many cases the free energy of a system can be lowered by the incorporation of a certain concentration of defects due to an increase in the configurational entropy of the system [7]. At this point it is worth distinguishing between different types of defects for the purpose of later discussions. Firstly, if a defect does not involve any atoms that are foreign to the host crystal, then the defect is called an intrinsic or native defect. Defects involving foreign atoms, or impurities, are referred to as extrinsic defects. Figure 3.4b and 3.4c show some examples of extrinsic and intrinsic defects. In our study on $\text{Cu}_2\text{ZnSnS}_4$ we are first interested in the fundamental material properties so we are currently only concerned with intrinsic defects, although in real systems impurities are often unintentionally present in the growth or processing environment. Defects are usually classified as point or line defects. Point defects usually involve isolated atoms in localized regions of a host crystal, whereas line defects involve rows of atoms, such as a dislocation defect. An example of a line defect is shown in figure 3.4a. Another possible type of defect is a defect complex, which is composed of a small number of point defects. Some examples of defect complexes in $\text{Cu}_2\text{ZnSnS}_4$ were shown in figure 2.8. There are then a number of different possible point defects, such as: vacancies, interstitials and antisites. For $\text{Cu}_2\text{ZnSnS}_4$, some examples of possible defects include sulfur vacancies (V_S^0 , V_S^+ , V_S^{2+}) and copper-on-zinc (Cu_{Zn}^-) and zinc-on-copper (Zn_{Cu}^+) antisites, where Cu_{Zn}^- and Zn_{Cu}^+ form the charge neutral

defect complex $[Cu_{Zn}^- + Zn_{Cu}^+]$. The sulfur vacancy is an example of an electrically active defect. In this case the defect can contribute two free electrons to the host crystal and so is a donor or n-type defect. The free electrons can then either be fairly localized on the defect site to form a small polaron, or extended across several sites to form a large polaron, or be completely delocalized across the system.

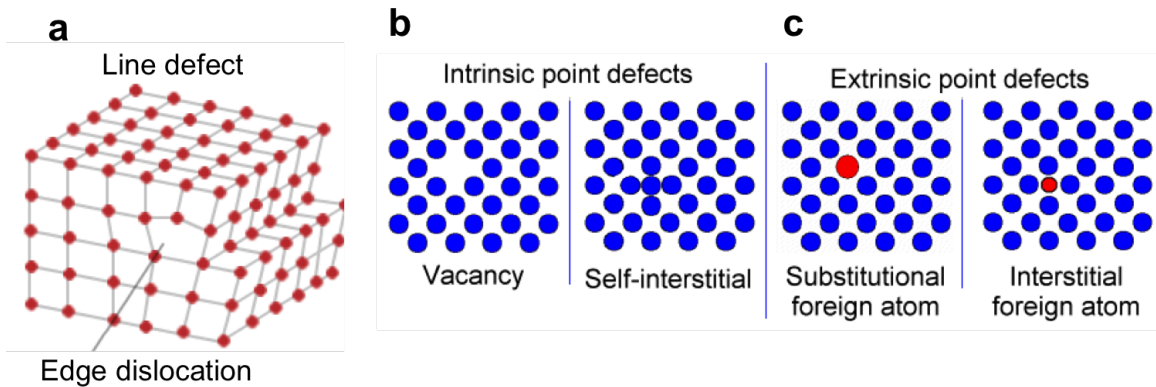


Figure 3.4: An example of a line defect (a) and both intrinsic (b) and extrinsic (c) point defects. Figures taken from references 41 and 104 respectively.

The electrical properties of semiconductors can be modified significantly by the incorporation of very small amounts of impurities or defects. It is often the case that less than one defect per million of host atoms is sufficient to alter the properties of a semiconductor [158]. This sensitivity to defects is one of the reasons why semiconductors find many uses in device applications. For example, luminescence centres in wide-band-gap materials can be used to emit light at specific wavelengths or single-spin centres provided by defects can act as artificial atoms and serve as a qubit in a quantum information system [2]. In order to control the electrical properties of a material by introducing defects, typically processes must first be developed to produce a fairly defect-free material, before intentionally introducing particular defects [158]. However in the case of solar cell devices the presence of defects is typically detrimental. Various ways in which defects in the absorber material can impede solar cell performance are discussed further in section 3.3.2 and more general characteristics of defects in semiconductors are discussed in the next section.

3.3.1 Impact of Defects on the Band Structure & Optical Spectra

The energy band model, which was discussed in section 3.2, has been successful in explaining many aspects of the behaviour of solids and a large amount of experimental data collected has supported the theoretical predictions made using the model. Its main drawback however is that it assumes a perfect, or nearly perfect, crystal lattice. It applies well to single crystals and polycrystalline substances, but cannot be applied to materials that are amorphous or heavily disordered so that the structure deviates significantly from the periodicity of the crystal [67].

Some defects result in additional energy levels in between the valance-band maximum and conduction-band minimum, i.e. within the band gap of the material. Electrically active defects have at least one defect level in the band gap. This level then has an associated defect wavefunction, a state to which the electron is added to or removed when the charge state of the defect changes. If the defect level is positioned relative to the band edges such that the defect is likely to be thermally ionized at room temperature then the defect is conventionally referred to as a shallow level. Otherwise it is referred to as a deep level. Typically deep levels are thought to be the most detrimental to solar cell device performance, which will be discussed further in section 3.3.2. Another way of defining a defect as ‘shallow’ or ‘deep’ is based on the degree of localization of the wavefunction. If a defect wavefunction is delocalized (on the order of many lattice constants) then the defect has the characteristics of a shallow defect. If the wavefunction is instead localized on the length scale of an atomic bond then this indicates a deep level defect [2].

Low concentrations of impurities and defects can be modelled by considering, for example, the introduction of distinct additional donor and acceptor energy levels within the band gap of a material and the scattering of electrons and holes in the solid. However, at higher defect concentration, these local levels interact to form a band. For high n-type doping, for example, the impurity band merges with the conduction band, causing a rigid shift of the conduction band towards the valence band [102]. The band profile can be modified with increasing donor density as shown in figure 3.5 to give rise to conductivity even at temperatures that are too low to produce excitation of carriers into the free conduction bands, called impurity band

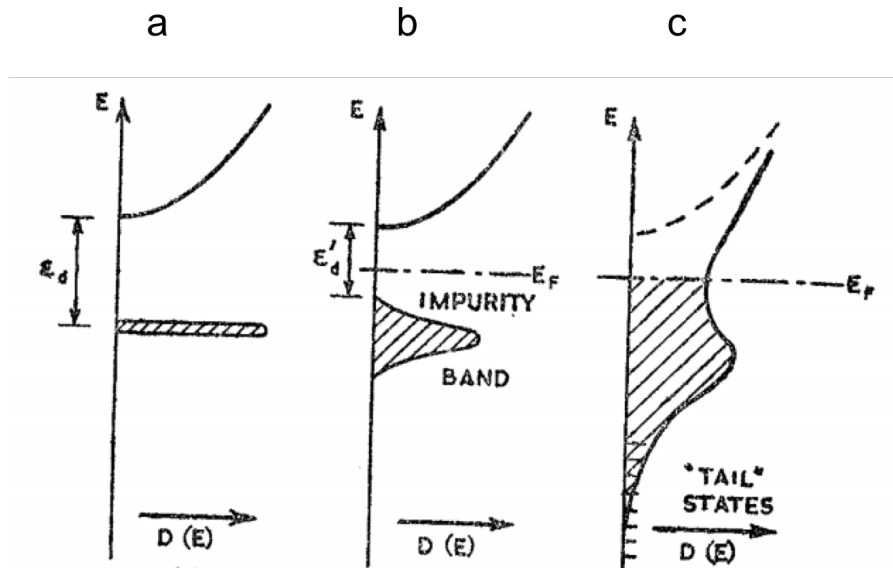


Figure 3.5: The influence of increased donor impurity density on the conduction band profile showing low (a), medium (b) and high (c) densities of impurities. Figure taken from reference 68.

conduction [68]. In heavily-doped semiconductors it is possible to observe a phenomena called ‘band tailing’, where the valence and conduction bands are shifted towards each other resulting in a narrowing of the band gap, as shown in figure 3.6 [102]. The heavy-doping effects then result in a different emitted spectrum which can be detected by techniques such as photoluminescence (PL) spectroscopy.

In a PL experiment, photons with energies larger than that of the band gap excite electrons from the valence band to the conduction band, as shown in figure 3.7a. In addition, electrons can be excited from or to defect levels, as shown in figure 3.7b. When the excited electrons transition to lower energy levels, they can emit light to conserve energy, resulting in a peak in the PL spectrum. In a photoluminescence excitation (PLE) experiment, the PL intensity is measured as a function of excitation photon energy. This gives an absorption profile for the defect. PL measurements are able to pick up optical signatures of defects even if they are only present at low concentrations with high resolution [2]. A review of some of the photoluminescence spectra for Cu₂ZnSnS₄ in the literature and the implications for PV device performance is discussed in section 3.3.3. PL measurements alone however cannot be used to identify the character of a defect, this is an area where first-principles defect calculations can provide valuable insight [2].

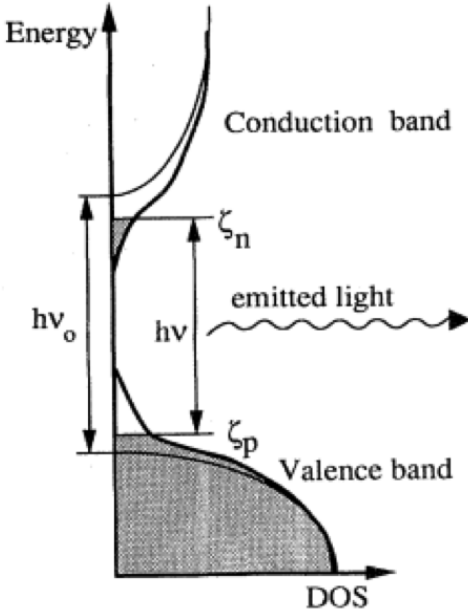


Figure 3.6: Schematic of the laser operation at $T=0$ K in GaAs. $\zeta_{n,p}$ are the quasi-Fermi level for electrons and holes respectively. The narrow line denotes the unperturbed density of states (DOS), while the heavy line depicts the DOS modified by heavy-doping effects. Both valence and conduction bands are shifted towards each other to give a narrowing of the band gap and the DOS is distorted, showing band tails. Heavy doping effects result in a different emitted spectrum. Figure taken from reference 102.

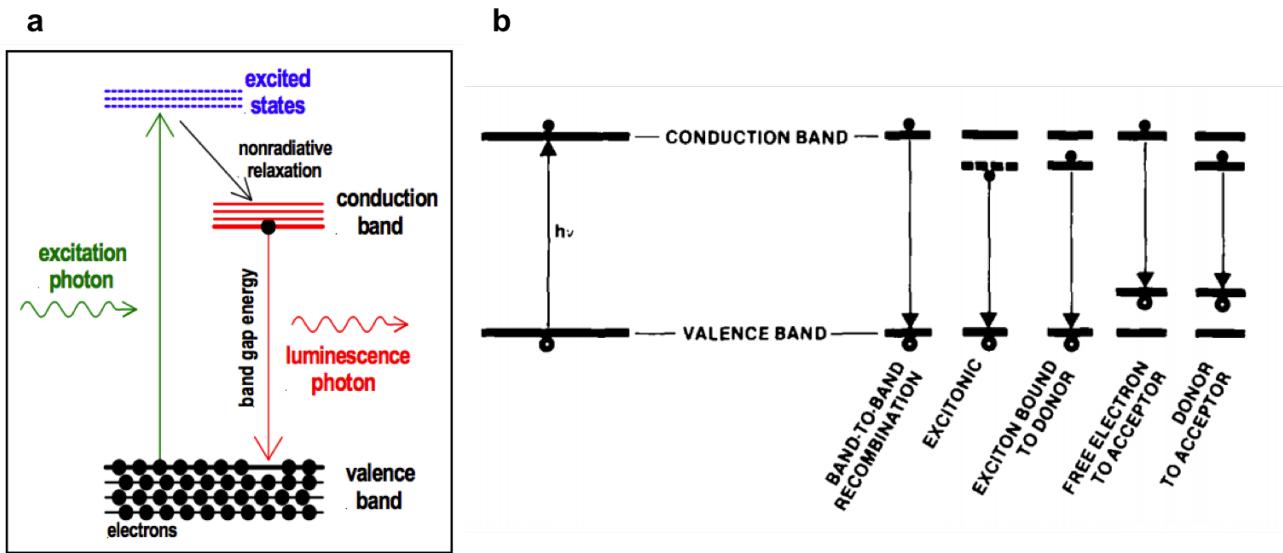


Figure 3.7: Basic optical transitions involved in a measurement during photoluminescence spectroscopy (a). Common emission transitions detected during photoluminescence measurements, including transitions involving defect levels (b). Figures taken from reference and 102 respectively.

Observed band tailing can be caused by either spatial band gap variations or electrostatic potential fluctuations in the material [49]. In the case of the latter, it is the inhomogenous

distribution of ionized defects that cause the fluctuations. An ionized donor exerts an attractive force on conduction electrons and a repulsive force on valence holes. As the defects are distributed randomly, the local interaction varies depending on the crowding of the defects. In this case the energy gap between the valence band and conduction band is maintained, as shown in figure 3.8 and the states of each tail are spatially separated [102]. Defects can also result in fluctuations in the band gap of a material. For example, if an impurity atom is of a different size to the atoms of the host lattice, then this can result in a local mechanical strain, as shown in figure 3.9b which results in a deformation potential, such as that shown in figure 3.9c for an edge dislocation defect. Local strains can alter the separation of atoms in the crystal and, as figure 3.9a shows, the atomic separation within a crystal has a significant impact on the band structure.

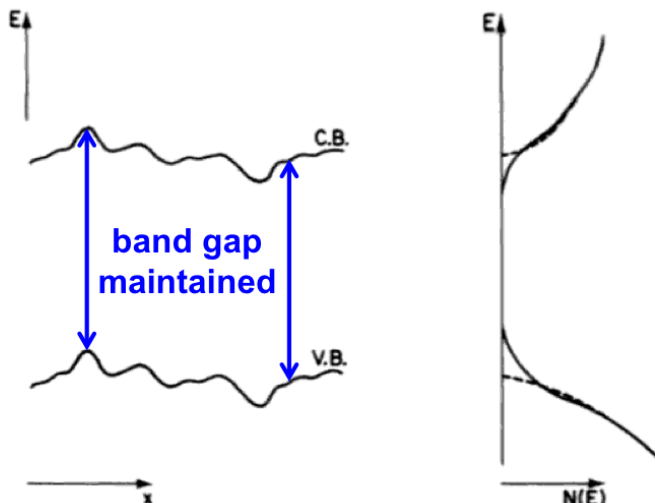


Figure 3.8: The perturbation of the band edges by Coulomb interaction with inhomogeneously distributed impurities (left), leading to the formation of tail states (right). Dashed lines show the distribution of states in the unperturbed case. Figure taken from reference 102.

3.3.2 Impact of Defects and Disorder on Solar Cell Performance

As already discussed, even very low concentrations of defects in a semiconductor can have a significant impact on its optoelectronic properties and therefore heavily influence the performance of an optoelectronic device composed of the material. As discussed in section 1.1.4, one of the main motivations behind developing thin-film PV technologies, where the absorber layer

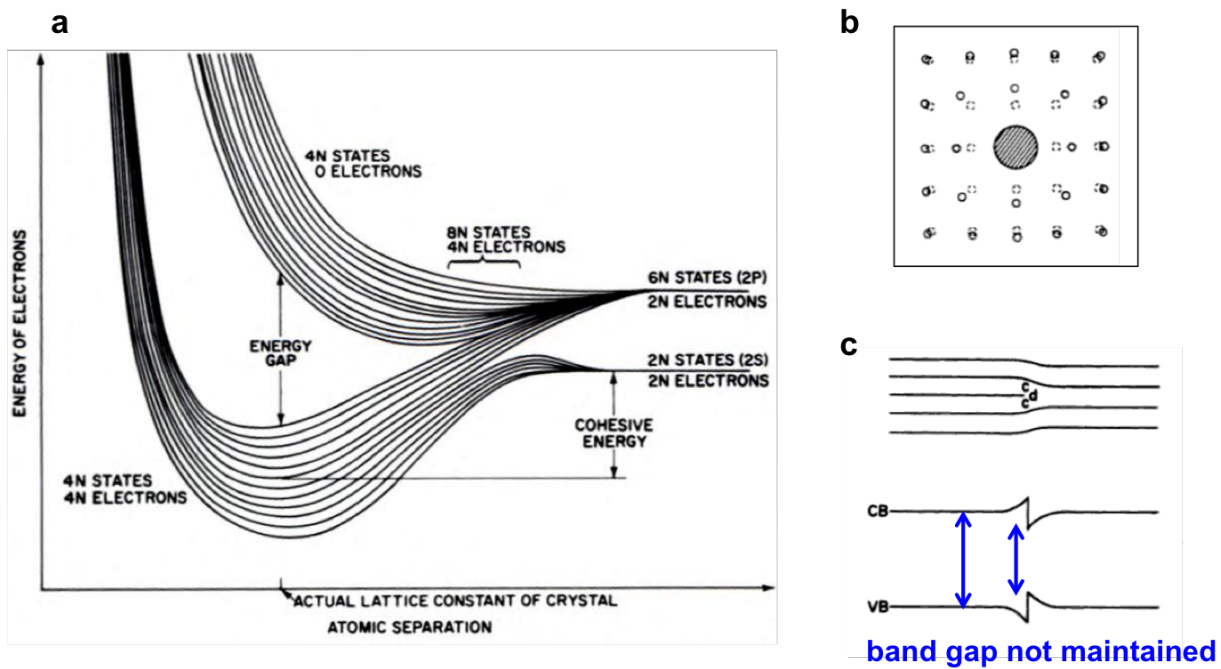


Figure 3.9: Energy banding of allowed levels in diamond as a function of spacing between atoms (a). Compressional strain induced in a crystal lattice by the incorporation of a large impurity atom (b). Deformation potential in the band structure due to compressional and dilational strain from an edge dislocation defect (c). Figures taken from reference 102.

is considerably thinner than that of a conventional silicon wafer, was to reduce the demand on the quality and low-defect concentrations of the material to reduce the energy intensity and high costs associated with the fabrication of the high quality material. A large number of compound semiconductors with direct band gaps have been studied for use in solar cells and some, such as CdTe and CIGSSe, have been commercialized. However, as the number of elemental components in a compound semiconductor increases, so does the various types of defects and disorder that can be present in the material, some of which will have more detrimental effects on device performance than others.

Firstly, thin-films of solar absorber materials fabricated using low cost synthesis techniques will be highly polycrystalline, therefore the layer will contain many grain boundaries, which can heavily influence device performance. In the specific case of CuInSe₂, the more polycrystalline material was found to produce higher-performing devices than its single crystalline counterpart [118, 113], but this has been attributed to the unique grain boundary physics of this material [107, 108]. Typically, grain boundaries are a sink for defects and therefore are more closely

associated with the detrimental effect of defects on PV performance, such as Shockley-Read-Hall recombination which will be discussed further below. It can also be very challenging to synthesise a single phase of a multicomponent material as a large number of secondary phases will also exist which can unintentionally be produced. For CZTS, phase diagrams have been constructed that show only a very narrow region for single phase CZTS, where only an absolute deviation of 1-2% in the composition at most would still result in a single phase of the crystal [129]. A schematic showing various possible secondary phases that could be produced during the synthesis of CZTS is shown in figure 3.10. The formation of secondary phases can be problematic due to recombinations at interfaces between secondary phases but also because the different phases may have a different band gap. Some of which may be less than that of CZTS and so could hinder device performance. However in our study, we are primarily concerned with the properties of the bulk material, to determine if there are fundamental material properties that will limit device performance.

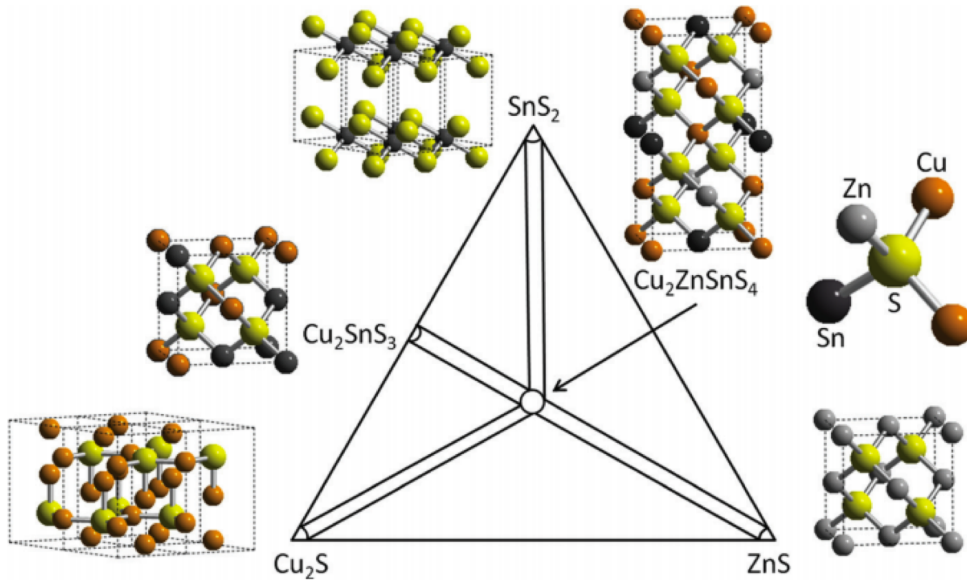


Figure 3.10: Schematic of the thin film Cu_2S - ZnS - SnS_2 ternary phase diagram at 325°C deposition temperature. The crystal structures of CZTS and the observed secondary phases are also presented. Figure taken from reference 38.

Of bulk defects and disorder, defects that produce mid-gap states (i.e. deep defect levels) act as Shockley-Read-Hall recombination sites [127], which was illustrated in figure 2.5. This is regarded as the most important recombination process in real, non-perfect semiconductors. It is a form of non-radiative recombination where a charge carrier is trapped in the defect state

before recombining with a charge carrier of opposite polarity. This type of recombination is known to be detrimental to device performance as essentially it results in energy input from sunlight not being converted into electricity [91]. In the case of Cu₂ZnSnS₄, for the most part predictions of defect formation energy and defect levels suggest that defects which would be expected to produce a deep defect level, also have a high formation energy so would be expected to be less likely to form [29].

For Cu₂ZnSnS₄ a lot of attention in the literature has been paid to disorder amongst Cu and Zn cations with a large amount of experimental evidence for the presence of this disorder [119, 148, 86] and theoretical predictions for the low formation energy of the $[Cu_{Zn}^- + Zn_{Cu}^+]$ [29]. During the synthesis of CZTS, temperatures above room temperature are used and it is possible for some of the thermal disorder associated with the system at higher temperatures to be ‘frozen in’ to the material as it cools to room temperature. Near resonant Raman spectroscopy has been used to examine thin films of CZTS prepared using different thermal treatments to determine if long post-annealing cooling times could produce films with a high level of order amongst Cu and Zn cations. However in this study, the authors postulate that achieving a very high level of order amongst Cu and Zn could require years [116]. This clearly wouldn’t be a practical treatment for a PV device and so it would seem that the presence of a fairly large amount of disorder amongst Cu and Zn, and hence Cu_{Zn}^- and Zn_{Cu}^+ antisites, is inevitable in the material.

Although Cu_{Zn}^- and Zn_{Cu}^+ antisite defects have been predicted to produce only shallow defect levels within the band gap of the material [29], their presence could be linked to band tailing in the material. Point defects in an otherwise perfect lattice can be regarded as missing lattice atoms, which are replaced by lattice defects. Therefore for every defect that creates one or more levels in the band gap of the material, the same number of levels that would have been created by the atoms in the host lattice are missing. Additionally, the lattice atoms surrounding the defect relax into shifted positions and also create states that could be shifted slightly into the band gap [18]. All of these states contribute to perturbations in the band edge, such as that shown in figure 3.6. Such a tail of band states into the band gap is often referred to as a Lifshitz tail [81], it can be observed experimentally and is most noticeable in heavily doped

and amorphous semiconductors [18]. For disorder due to defects with a correlation length on the order of interatomic spacing, the absorption coefficient, α_0 (which was discussed as a key property for PV materials in section 1.1.3) shows a exponential decline. This effect, illustrated in figure 3.11, is referred to as the Urbach tail [141] and is widely observed in disordered semiconductors [18]. Such tailing can be quantified by the Urbach energy, and it has recently been proposed that there is a direct link between the Urbach energy and open circuit voltage deficit in standard photovoltaic materials [22, 152].

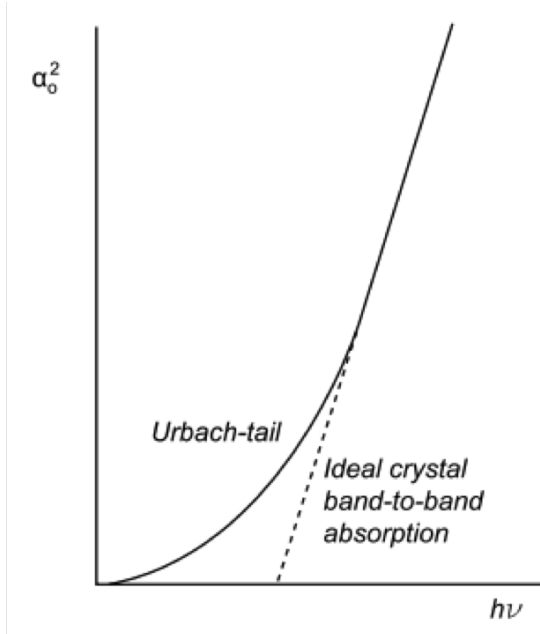


Figure 3.11: Optical absorption spectrum of a typical direct band gap semiconductor with the absorption coefficient, α_0 , proportional to the extended density of states in the Urbach tail. Figure taken from reference 18.

3.3.3 Photoluminescence Spectra of Cu₂ZnSnS₄

Photoluminescence (PL) spectroscopy is a popular method to inspect solar cell materials as it does not require a full functioning device and can be a powerful tool for probing defects in semiconductors. There are a large number of possible optical transitions that can be detected by PL measurements, some of which were illustrated in figure 3.7. For this reason, low-temperature PL can be a particularly powerful tool for probing defects as energy level occupancy is dependent upon temperature and so not all PL recombinations will occur at the same temperature, allowing for the isolation of different types of recombination transitions [19].

There are also other variations in the set up of a PL measurement that can be altered to provide more information on the band structure and how it is altered by the presence of defects. Firstly the intensity of the laser can be increased to determine if states are localized (such as those introduced by defects) or extended states (such as the conduction and valence bands) by if it is possible to saturate the states in the case of localized states such that an increase in laser intensity no longer increases the intensity of the PL peak [46]. Secondly, time-resolved PL (TRPL) measurements can be used to differentiate between recombination mechanisms with different carrier lifetimes. Slower optical transitions usually involve carriers in localized states, whereas faster transitions usually involve delocalized states [46].

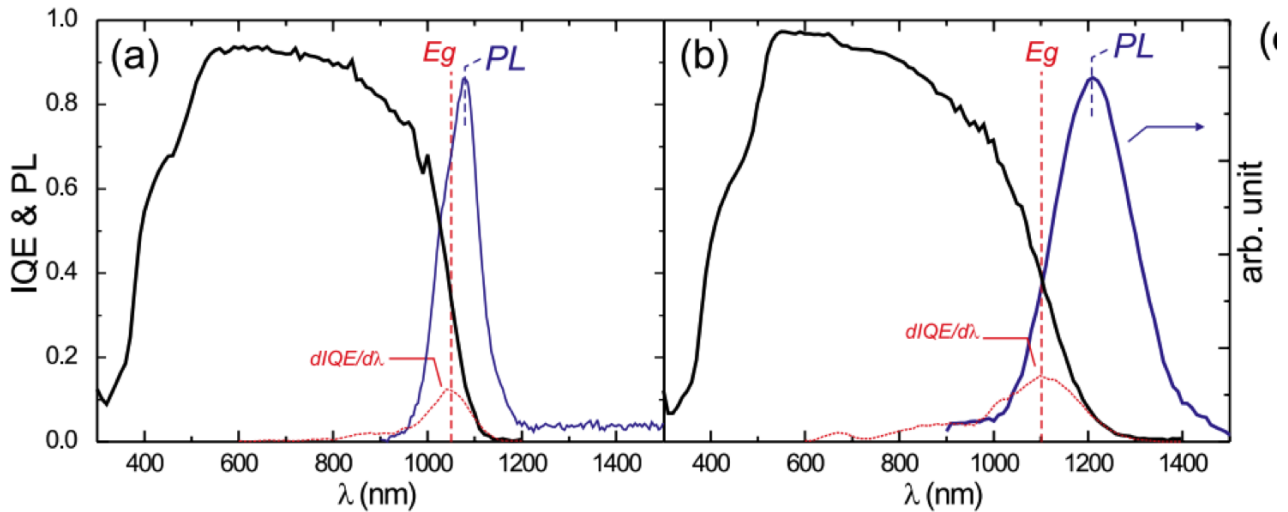


Figure 3.12: The internal quantum efficiency (IQE), band gap as determined from the IQE inflection point and the photoluminescence spectra of high performance devices with thin-film absorber layers of (a) CIGSSe ($E_g = 1.19$ eV) and (b) CZTSSe ($E_g = 1.13$ eV). Figure taken from reference 49.

Several PL studies have been performed on kesterite-structured samples of $\text{Cu}_2\text{ZnSnS}_4$, $\text{Cu}_2\text{ZnSnSe}_4$ and alloys of the two. PL measurements have been performed on both full devices and polycrystalline thin-films [49, 46, 45, 115, 89, 140] and single crystals [53, 79, 58]. In addition studies such as reference 53 compare the PL spectra for varying compositions of the sample, whereas in reference 49 measurements on both CIGSSe and CZTSSe thin films are performed in an attempt to account for the difference in the performance of these two technologies by comparing their defect-influenced PL emission spectra. Polycrystalline samples are more similar to those likely to be used in thin-film CZTS photovoltaic devices, however comparison between those

measurements with single crystal measurements could enable the isolation of recombination at grain boundaries from those due to bulk defects. Also measurements performed on single crystals as close to perfectly stoichiometric Cu₂ZnSnS₄ as possible are likely to be the most directly relatable to our simulations on bulk systems. However one feature common to all of the PL spectra from studies on kesterite samples is clear evidence of defects and disorder from the observed band tailing. The PL spectra of kesterite samples usually features a much broader peak than that observed in CIGSSe samples, such as that shown in figure 3.12. The energy of the maximum PL peaks of kesterite samples is also usually considerably red-shifted compared to the energy of the band gap. These two features are usually attributed to band tailing caused by either spatial band gap variations or electrostatic potential fluctuations in the absorber material, which were discussed in section 3.3.1. Both effects lead to a non-zero density of states (DOS) within the band gap [22, 49]. Measurements performed in reference 49 found the tailing in CZTSSe to be roughly twice as severe as that observed in higher-performing CIGSSe devices.

However, there is some disagreement in the literature about the main recombination mechanisms that could explain the observed PL spectra. Of the measurements performed on single crystals, reference 79 perform measurements on near-stoichiometric CZTS crystals and report a free-to-bound transition between the conduction band and an acceptor level. In reference 58, donor-acceptor-pair (DAP) transitions are reported for large single grains of CZTS, whereas in reference 53 where measurements are performed on CZTS single-crystals of varying composition, they report PL measurements through spatially fluctuating band states as would be expected from either spatial band gap variations or electrostatic potential fluctuations from heavy defect compensation. Therefore in bulk monograins of CZTS PL band-to-impurity, DAP and spatially fluctuating band-type recombinations have all been reported and the exact sources, or rather associated defects, for these recombination mechanisms are not yet known [45].

For measurements performed on polycrystalline kesterite samples, some studies attribute the spectra to spatially fluctuating band tail states [115], whereas others suggest that recombination in CZTS is dominated by the distinct energy levels introduced by DAPs [140, 89]. In other studies, an explanation that is almost a combination of the two is proposed [46, 45]. These studies refer to a quasi-donor-acceptor-pair (QDAP) model, where the word ‘quasi’ is used to

indicate a deviation from the classical DAP model for recombinations, such as that shown in figure 3.7, due to interactions between defects. In reference 45 they note that distinguishing between DAP recombination and spatially fluctuating band tails caused by spatially varying densities of ionized donor and acceptor defects is particularly complicated as a high density of compensating DAPs is necessarily co-incident with spatial fluctuation in electrostatic potential. In the same work, they note that the dominance of donor and acceptor pairs on PL spectra is in agreement with theoretical predictions such as those by Chen et al [29] that antisite DAPs such as $[Cu_{Zn}^- + Zn_{Cu}^+]$ should be abundant due to the low formation energy of the defect complex and also experimental observations of cation disorder by neutron diffraction, synchrotron radiation x-ray diffraction and aberration corrected scanning transmission electron microscopy respectively [119, 148, 86].

In this work we will attempt to quantify the contribution to the observed band tailing in CZTS from disorder amongst copper and zinc cations, or equivalently, the presence of $[Cu_{Zn}^- + Zn_{Cu}^+]$ antisite defect pairs. The methodology will be outlined in more detail in section 4, but the general approach will be to use Monte Carlo simulations that have been parameterised with first-principles calculations to determine the extent of Cu-Zn disorder in CZTS at various temperatures and to then study the distribution of electrostatic potential across the system from the inhomogeneous spatial arrangement of the charged antisite defects, Cu_{Zn}^- and Zn_{Cu}^+ .

Chapter 4

Monte Carlo Simulation of Thermodynamic Disorder in $\text{Cu}_2\text{ZnSnS}_4$

For this study we have created a custom Monte Carlo code to simulate on-lattice substitutional disorder amongst copper and zinc ions in $\text{Cu}_2\text{ZnSnS}_4$ as a function of temperature. In the following sections the methodology applied in the development of the model and methods for quantifying structural disorder will be discussed. Methods for extracting information on band tailing from the disorder will be discussed in section 5.1 as future work.

4.1 Mapping the Crystal Structure of $\text{Cu}_2\text{ZnSnS}_4$ onto a Simple Lattice

The crystal structure of $\text{Cu}_2\text{ZnSnS}_4$ can be described by two inter-penetrating face-centred cubic (FCC) lattices: one of metal cations and one of sulfur anions, as shown in figure 4.1. We consider the sulfur sub-lattice to be stationary because any substitution between ions in the cation sub-lattice and sulfur anion sub-lattice would be energetically infeasible and any substitutions

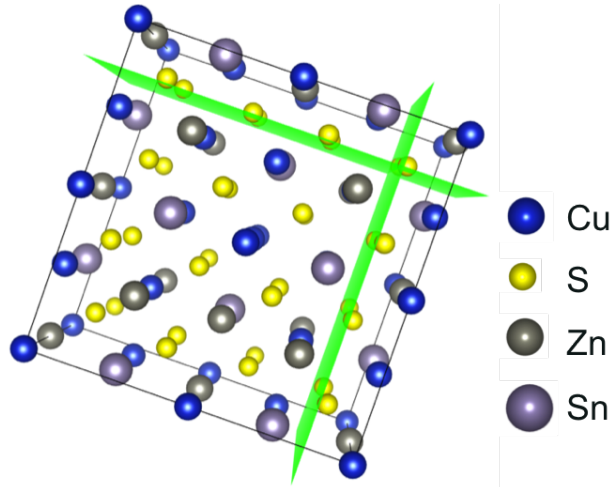


Figure 4.1: A supercell of the perfect Cu₂ZnSnS₄ crystal lattice, which can be described by inter-penetrating face-centred cubic sub-lattices: one of metal cations and one of sulfur anions. Green planes are used as guides to the eye to show planes of S anions that form one of the two face-centred cubic sub-lattices.

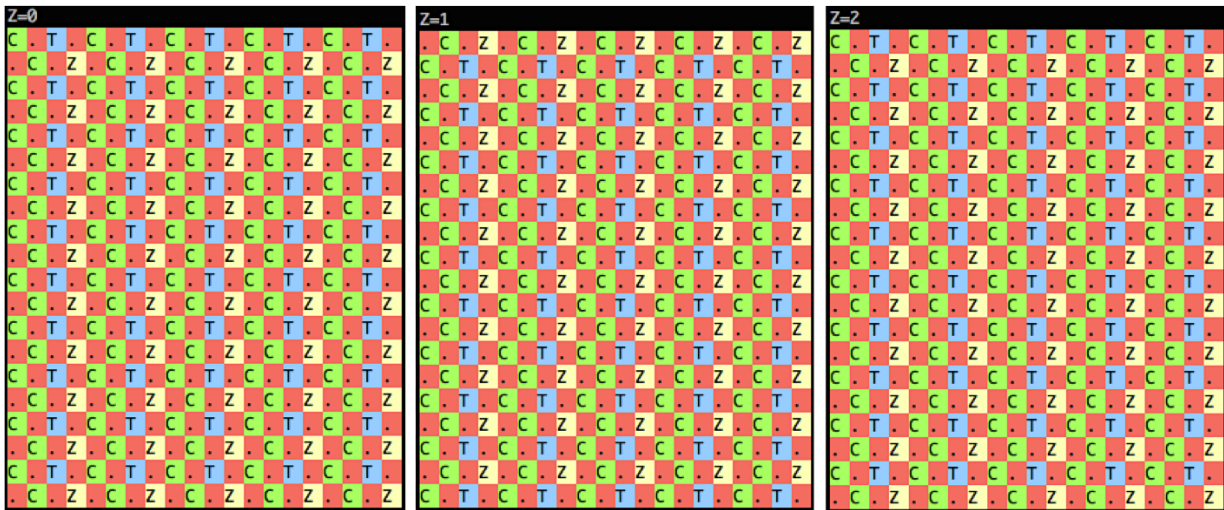


Figure 4.2: A two-dimensional (x-y) slice of a 20x20x20 cation sub-lattice of ordered Cu₂ZnSnS₄. Sulfur anions are neglected from the simulations and the face-centred cubic cation lattice is mapped onto a simple cubic lattice by including empty sites in the lattice. Alternating layers in the z-direction are displaced by one lattice unit in order to reproduce the correct kesterite structure. ‘C’, ‘Z’, ‘T’ and ‘.’ represent copper, zinc, tin and an empty site respectively.

amongst the sulfur anions in that sub-lattice would be energetically equivalent. The sulfur sub-lattice is therefore neglected during the Monte Carlo simulations but incorporated later in calculations of lattice electrostatics. This then reduces the problem of mapping the Cu₂ZnSnS₄ crystal structure onto a simple lattice to just one FCC cation lattice. We then map this onto a simple cubic (SC) lattice for our simulations by introducing empty lattice sites into the SC

lattice, as shown in figure 4.2. Sn ions are also fixed during our simulations to enable us to extract band tailing due to Cu-Zn disorder only. Furthermore, the formation of Sn defects has been predicted to have a considerably higher formation energy than that of Cu_{Zn}^- and Zn_{Cu}^+ antisite defects [29].

During our simulation the separation between lattice sites is one lattice unit but this is rescaled for calculations of lattice electrostatics using our DFT-optimised lattice parameters of $\frac{a}{2} = \frac{b}{2} = \frac{5.44}{2} \text{ \AA}$. Where the lattice parameters are divided by 2 as empty sites are placed in between ions to map the FCC structure onto an SC lattice. Figure 4.3 shows flat representations of the crystal structure, with empty lattice sites marked out by crosses. Lattice parameter c for our model will then be approximated to 2a, which is very close to the DFT-optimised value of 10.86 Å.

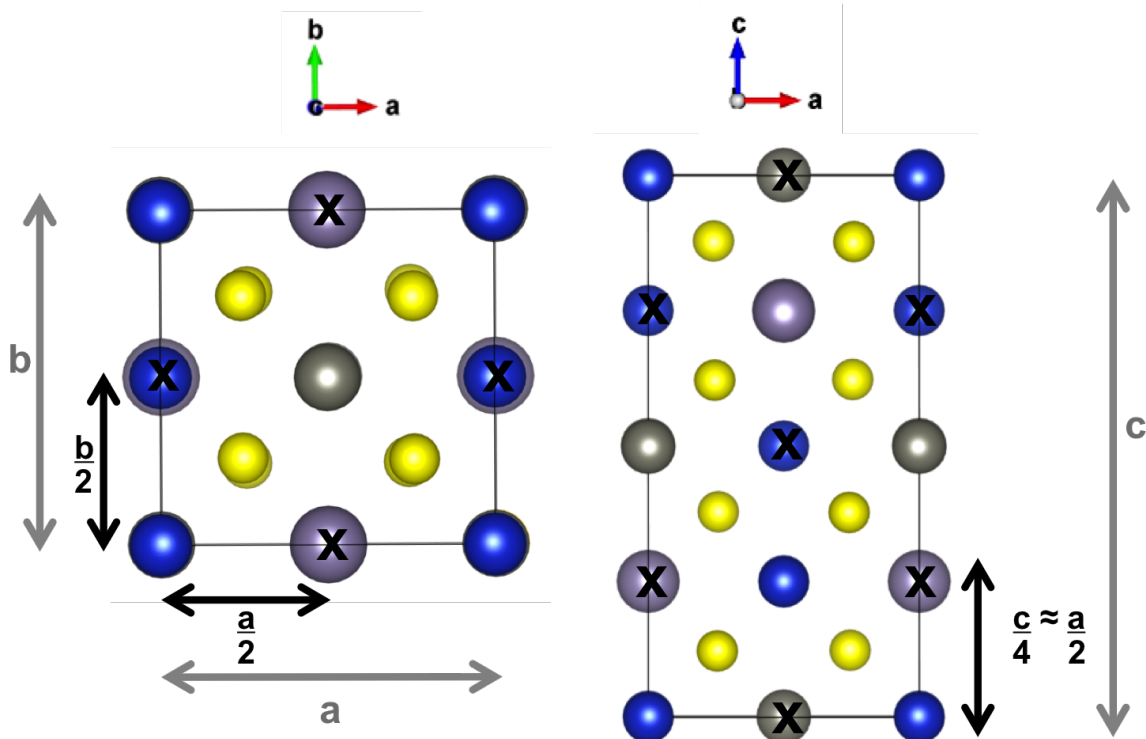


Figure 4.3: Visuals of the Cu_2ZnSnS_4 crystal structure showing positions of empty sites (denoted by x's) used to map the face-centred cubic lattice of the cations onto a simple cubic lattice. Lattice parameters obtained from hybrid density functional theory geometry optimizations are $a = b = 5.43770 \text{ \AA}$ and $c = 10.85670 \text{ \AA}$, and so c is approximately $2a$.

For some of our simulations, we initialise the system as the cation sub-lattice of the perfectly ordered crystal structure of CZTS. Then for simulations where we want to start from a dis-

ordered system, we again take this perfectly ordered initial structure but ‘shuffle’ Cu and Zn ions. An initial configuration of a large SC lattice of perfectly ordered CZTS is generated by producing a supercell of a unit cell of the perfectly ordered structure, where this unit cell was determined by examining the geometry of CZTS one layer at a time in three dimensions. An example of this analysis is shown in figure 4.4. The smallest unit cell was found to be a 2x2x4 cell when including the gap sites.

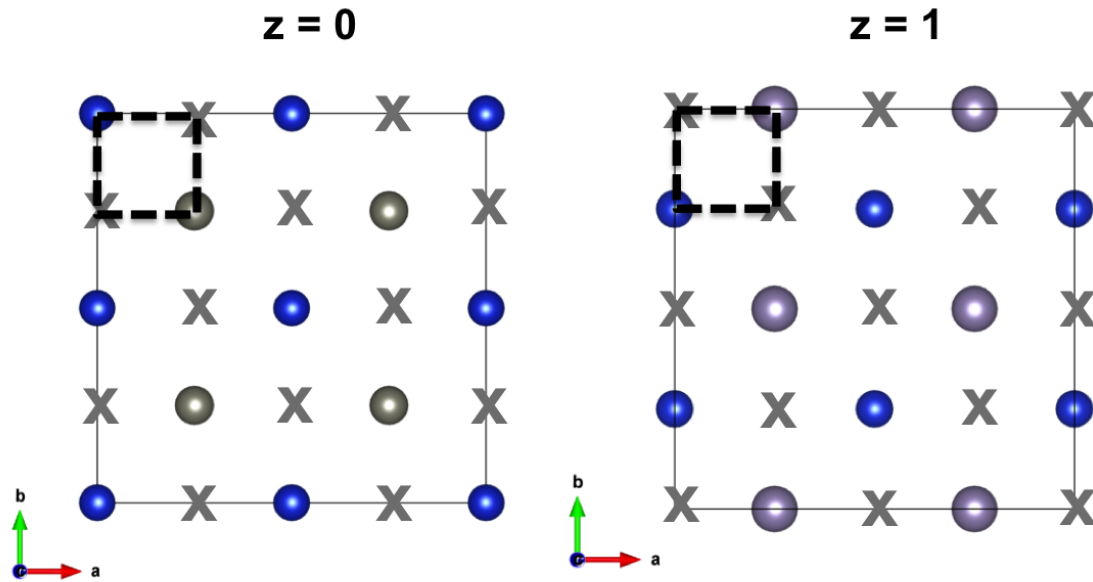


Figure 4.4: Some of the single layers of a CZTS supercell used to determine the minimum cation unit cell for constructing supercells in on-lattice Monte Carlo simulations. Here crosses are used to denote the empty sites used in to map a face-centred cubic lattice onto a simple cubic lattice.

4.2 Monte Carlo Simulation with the Metropolis Algorithm

The Monte Carlo method can be used to calculate thermodynamic information about a system of N interacting ions represented on a 3D lattice by using classical statistics, considering only two-body forces and assuming that the potential field of an ion is spherically symmetric. If we know the positions of the N interacting ions on the lattice then the potential energy of the system can be calculated using equation 4.1, where V is the Coulombic potential between two

ions and d_{ij} is the minimum distance between ions i and j [88].

$$E = \frac{1}{2} \sum_{i=1}^N \sum_{j=1}^N V d_{ij} \quad (4.1)$$

To calculate the properties of the system, the canonical ensemble is used where the temperature, number of ions and volume are all constant. In this ensemble, the equilibrium value for any quantity of interest, B, is given by equation 4.2, where E_α is the energy of the system when in state α and p_α is the probability of the system being in state α .

$$\langle B \rangle = \frac{\sum_\alpha e^{-\frac{E_\alpha}{k_b T}} B_\alpha}{\sum_\alpha e^{-\frac{E_\alpha}{k_b T}}} = \frac{\sum_\alpha e^{-\frac{E_\alpha}{k_b T}} B_\alpha}{Q} = \sum_\alpha B_\alpha p_\alpha \quad (4.2)$$

$$p_\alpha = \frac{e^{-\frac{E_\alpha}{k_b T}}}{\sum_\alpha e^{-\frac{E_\alpha}{k_b T}}} = \frac{e^{-\frac{E_\alpha}{k_b T}}}{Q} \quad (4.3)$$

Q in equation 4.2 is called the partition function. For most systems calculating the value of the partition function requires the summation over a large number of states. When applying the Monte Carlo method to a system of particles, the summation over discrete states for Q is replaced by a set of integrals. This is shown in equation 4.4 where $U(\mathbf{r}^N)$ is the potential energy of the system which depends upon the position, \mathbf{r} , of the N interacting ions in the system and Z_{NVT} is the configurational integral [78].

$$\langle U \rangle = \frac{\int e^{-\frac{U(\mathbf{r}^N)}{k_b T}} U(\mathbf{r}^N) d\mathbf{r}^N}{\int e^{-\frac{U(\mathbf{r}^N)}{k_b T}} d\mathbf{r}^N} = \frac{\int e^{-\frac{U(\mathbf{r}^N)}{k_b T}} U(\mathbf{r}^N) d\mathbf{r}^N}{Z_{NVT}} \quad (4.4)$$

The configurational integral is over the three coordinates of each ion, as shown in equation 4.2. There are therefore 3N coordinates that define all possible configurations of the system.

$$d\mathbf{r}^N = dx_1 dy_1 dz_1 dx_2 dy_2 dz_2 \dots dx_N dy_N dz_N \quad (4.5)$$

For a system containing several hundred ions this would be a several-hundred dimensional integral over the configuration space, which would be impractical to carry out by the usual numerical methods. The Monte Carlo method for many-dimensional integrals is used for this

purpose [88]. It is conceptually easiest to think about this method for a one-dimensional integral. This method involves sampling a large number of random points within a region defined by the limits of the integral. The integrated function is then the fraction of points that fall below the curve of the function multiplied by the area of the sampled region. The value obtained becomes a better approximation to the actual value of the integral as the number of random numbers, called Monte Carlo steps (MCS), used to sample the integration region increases. [78].

The Standard Monte Carlo method for our system would involve placing each of the N ions at random positions in the lattice to define a random point in the 3N-dimensional configuration space. The energy of the system would then be calculated using equation 4.1 and the configuration would then be weighted using $e^{-\frac{U(\mathbf{r}^N)}{k_b T}}$ when obtaining the equilibrium value of U. However, many configurations are very improbable so performing this calculation for every possible configuration would be inefficient and unnecessary to sufficiently evaluate the ensemble. The custom Monte Carlo code in this study makes use of the Metropolis modified Monte Carlo scheme [88]. In this implementation of the Monte Carlo method, instead of choosing configurations randomly and then weighting them, the Metropolis algorithm considers the relative probability of a system being in a new configuration, β , to that of being in the current configuration, α . This is shown in equation 4.6, where E_α is the energy of state α and E_β is the energy of state β .

$$\frac{p_\beta}{p_\alpha} = \frac{e^{-\frac{E_\alpha}{k_b T}}}{Q} \frac{Q}{e^{-\frac{E_\beta}{k_b T}}} = e^{-\frac{E_\beta - E_\alpha}{k_B T}} \quad (4.6)$$

The relative probabilities of the two states are completely determined by the energy difference, such that if:

$$\Delta E = E_\beta - E_\alpha \leq 0 \text{ then } \frac{p_\beta}{p_\alpha} \geq 1 \quad (4.7)$$

and if

$$\Delta E = E_\beta - E_\alpha > 0 \text{ then } \frac{p_\beta}{p_\alpha} < 1 \quad (4.8)$$

The Metropolis algorithm creates a list of configurations through configuration space that has the correct probability distribution. This list is called a trajectory through configuration space.

The approach involves making a trial move of the system to a new configuration, in the case of our study this would be a substitution between a Cu and a Zn ion. It is then decided if this new configuration should be added to the trajectory or not based on the probability of the new configuration relative to the current configuration. If the relative probability is ≥ 1 , as shown in equation 4.7, then the move is accepted and added to the trajectory. However, if the relative probability is < 1 then the move will only be accepted if $e^{-\frac{\Delta E}{k_B T}} \geq$ a random number generated between 0 and 1 [78].

4.3 Equilibration & Finite Size Effects

Our Monte Carlo model for Cu-Zn disorder is analogous to the Ising model of a ferromagnet, descriptions of which can be found in many textbooks such as references 95 and 74. In the case of an Ising model, the trial moves in the Metropolis algorithm are spin flips, whereas in our model the trial moves are swaps between Cu and Zn ions. Typically when performing simulations of an Ising model the calculated quantities of interest are the internal energy and average magnetization of the system as a function of temperature obtained by summing over the distribution of atomic spins. In the case of our system, the quantities of interest are the spatial arrangement of the Cu and Zn ions due to thermodynamic substitutions between the two species and the resulting distribution of electrostatic potential across the system for the implications this could have on band tailing. As we fix Sn ions in our simulation we calculate the on-site electrostatic potential for Sn ions to study how the chemical environment of these species is altered by Cu-Zn disorder. However, before we attempt to extract any information on thermodynamic disorder or the associated band tailing we would predict from such disorder, two important considerations for our model will be firstly to determine if the disordered configuration we obtain is in fact the equilibrated configuration at the given temperature and secondly if finite size effects are having an impact on the system properties we obtain from our simulations.

As simulations are performed for finite lattices, in order to simulate a bulk system the edges

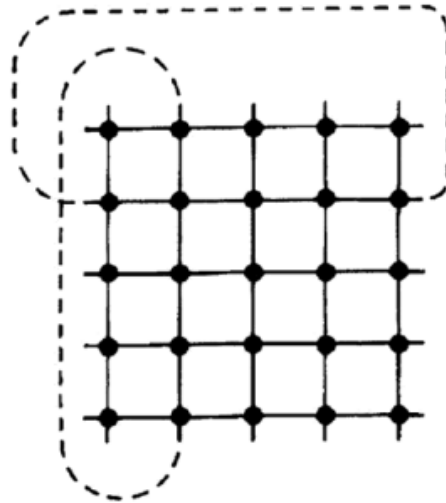


Figure 4.5: Typical periodic boundary conditions for the two-dimensional Ising model. Figure taken from 74.

or ‘boundaries’ of the system must be treated carefully. The boundaries can be effectively eliminated through the use of periodic boundary conditions (PBCs). In the case of an Ising model, this means that the first spin in a row interacts with the last spin in the row as if it were a nearest neighbour, and vice versa [74]. This principle is illustrated for a two-dimensional system in figure 4.5. Although this procedure effectively eliminates boundary effects, the system is still characterized by the finite lattice size, L , which limits the correlation length to $\frac{L}{2}$. Resultant properties of the simulated system may then differ from the bulk system. We therefore will need to perform simulations with increasing system size to look for any differences in the quantities of interest.

Determining if our system has reached equilibration at each temperature however may require a more complicated procedure. As the Monte Carlo method is stochastic, making use of sampling many times with random numbers in order to determine the minimum energy configuration of the system, the trajectory to reach this final configuration will by nature be random. Therefore, we can draw no conclusions about the properties of our system from evolved states until the final configuration at the particular temperature is reached. Even then we must consider the possibility of our system finding local minima instead of global minima, and therefore giving a false impression of having equilibrated. We therefore are developing methods to check for equilibration before we attempt to extract any thermodynamic properties of our system.

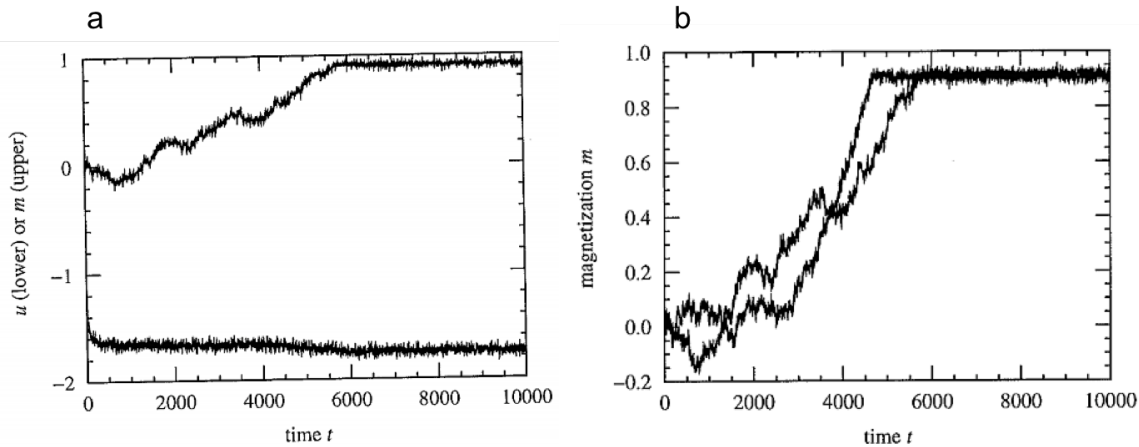


Figure 4.6: The magnetization (upper curve) and internal energy (lower curve) per site of a two-dimensional Ising model simulated using the Metropolis algorithm (a). Magnetization as a function of time for two different simulations (b). Time is measured in Monte Carlo steps per lattice site. Figures taken from 95.

In the case of the Ising model when, for example, determining the average magnetization of a system at a given temperature, the simulation must be run for a suitably long time until the system has come to equilibrium at that temperature. This is referred to as the equilibration time and the point at which a system has attained equilibrium can be defined as being when the average probability of finding the system in any particular state α is proportional to the Boltzmann weight of that state, $e^{-\frac{E_\alpha}{k_b T}}$. Once the system has equilibrated, the quantity of interest such as the magnetization must then be measured again over a suitably long time and averaged [95]. To gauge if a system has reached equilibrium, in the case of the Ising model, it is common practice to run the simulation for a large number of Monte Carlo steps (MCS) (where one MCS corresponds to attempting a trial spin-flip at all sites in the system once) and looking for how the value of a quantity of interest, such as the average magnetization across the system, changes with increasing number of MCS as the simulation progresses. Equilibration is often considered as the point at which the value of a quantity of interest, which initially changes by a large amount, eventually converges to fluctuating about a steady average value. An example of this is shown in figure 4.6a. This is dependent upon the principle that a system in equilibrium spends the overwhelming majority of its time in a small subset of states in which its properties take a narrow range of values [95]. Provided the simulation is allowed to run for a sufficiently long time to reach this global minimum energy (or equilibrium) configuration

and that the system does not become stuck in a local minimum state, the final configuration for a given system at a given temperature should always be the same regardless of the initial configuration of the simulation, this point is illustrated in figure 4.6b.

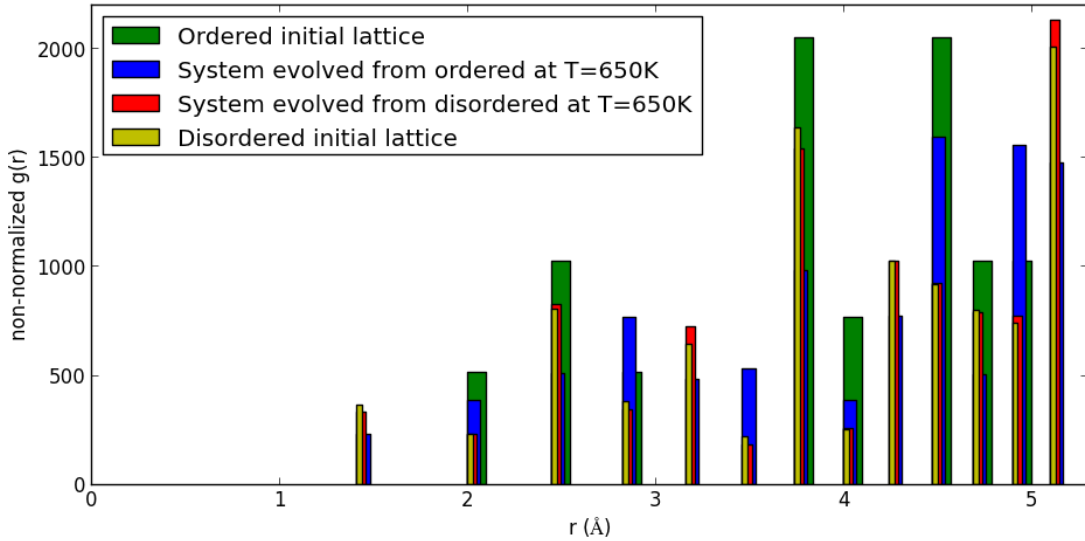


Figure 4.7: The radial distribution function (RDF) between pairs of zinc ions in $\text{Cu}_2\text{ZnSnS}_4$ before normalization. RDFs of an initial perfectly ordered lattice are plotted with that of a disordered initial lattice as reference points as well as systems that have been evolved from both of these initial configurations at $T=650\text{K}$. Widths of the bars plotted are arbitrarily chosen to ensure all data is visible.

Using this principle, one way to determine if our system has reached its equilibrium configuration could be to use the perfectly ordered or disordered initial lattice configurations that were discussed at the end of section 4.1. Both of these initial configurations, if the simulation is allowed to evolve over a suitable number of MCS, should eventually result in the same equilibrium system configuration. It would be difficult to distinguish differences in the atomic arrangement of one 3D lattice to another by eye, therefore comparisons of the radial distribution function (RDF) for each configuration as it evolves from either an ordered or disordered initial configuration will be made. Using RDFs for structural analysis will be discussed further in section 4.6, but for the present discussion, the point after which the RDF of the system evolved from an ordered initial lattice converges to being the same as that of a system evolved from a disordered initial lattice could be one way to determine if the system has reached its equilibrium configuration.

An example of this analysis is shown in figure 4.7. So far, we have seen that the system evolves much faster (in terms of number of MCS as opposed to time) when starting from an initially ordered configuration than an initially disordered configuration. This could be explained by it being more entropically favourable for a system to move away from a highly ordered system than to move from a disordered configuration to a more ordered configuration. So far in our study we have found that the system evolution from a disordered initial configuration is possibly too slow for comparisons between this simulation and that from an ordered initial configuration to be a feasible method to check for equilibration.

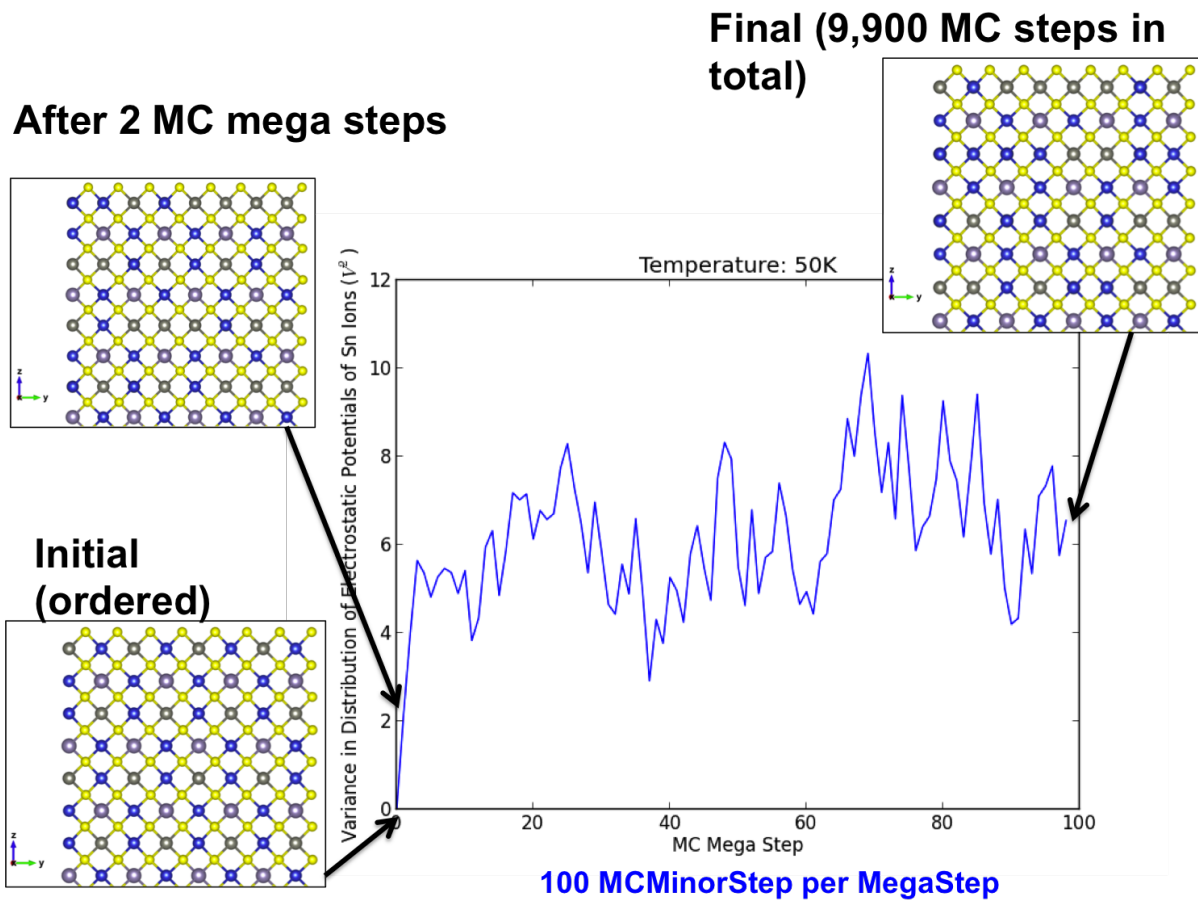


Figure 4.8: Variance in the distribution of Sn ions in a system of containing 128 Sn ions, where the system is evolved from an initially perfectly ordered lattice. Each ‘MC Mega Step’ corresponds to 100 Monte Carlo steps, which for our simulations are substitutions between Cu and Zn ions. Representative two-dimensional slices of the system are shown during system evolution from the perfectly ordered lattice, which when viewed along this crystallographic direction is alternating layers of Cu-Zn and Cu-Sn ions.

Another method to check for equilibration is analogous to that shown in figure 4.6a for the Ising model. In the case of our system, it is the distribution of the electrostatic potential at Sn sites

in the system that is of interest so one possible method to check for equilibration could be to look for a point after which the variance of the distribution of electrostatic potentials across the system has reached a steady value. An example of this analysis is shown in figure 4.8, where the system was evolved from an ordered initial configuration. In contrast to the disordered initial configuration, systems evolved from an initially perfectly ordered lattice appear to equilibrate quickly where in figure 4.8, each ‘MC Mega Step’ corresponds to 100 Monte Carlo steps (MCS). The figure shows the variance evolving from the initially perfectly ordered system, in which there is only one distinct crystallographic environment for Sn and so the variance is zero, to fluctuating around a finite value. Figure 4.9 shows the same simulation performed with 1000 MCS per data point.

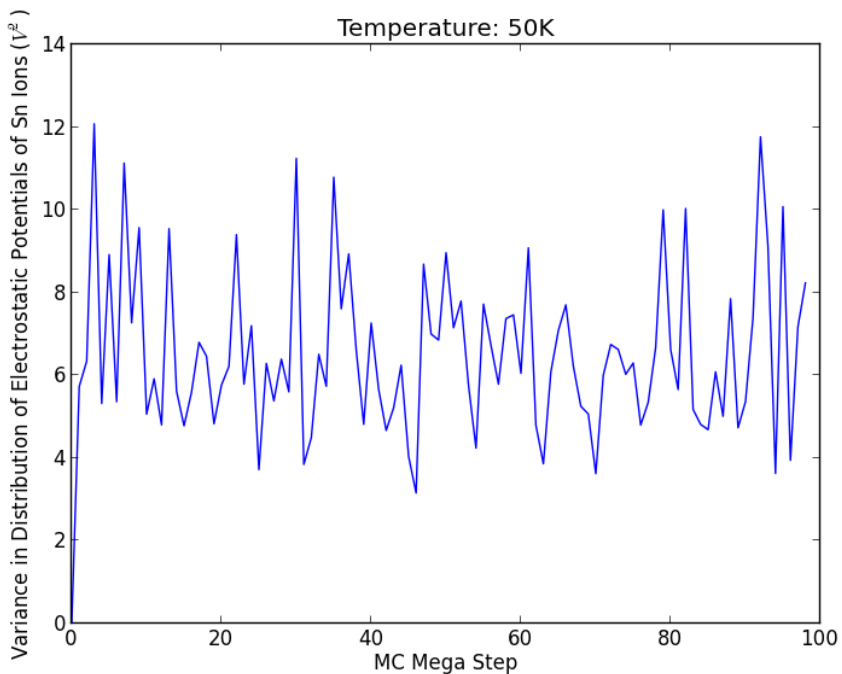


Figure 4.9: Variance in the distribution of Sn ions in a system of containing 128 Sn ions, where the system is evolved from an initially perfectly ordered lattice. Each ‘MC Mega Step’ corresponds to 1000 Monte Carlo steps, which for our simulations are substitutions between Cu and Zn ions.

4.4 Multi-Scale Approach with Density Functional Theory

Equation 4.9 can be used to calculate the electrostatic interaction between a pairs of ions, where q_1 and q_2 are the bare formal charges, r is the separation of the point charges and ϵ_r is the bulk static relative dielectric constant. The interaction between all pairs of ions within the system are summed over when calculating the change in the energy of the system after performing a trial move in our Monte Carlo simulations.

$$E_{electrostatic} = \frac{q_1 q_2}{4\pi\epsilon_0\epsilon_r} e^2 \frac{1}{r} = q_1 q_2 I_{electrostatic} \quad (4.9)$$

We separate out the parameter $I_{electrostatic}$ in our simulations. The value is first calculated considering a purely classical, electrostatic case where only the bare formal charges on the ions are considered and the bulk dielectric constant of Cu₂ZnSnS₄ is used. Using a value of 13.2 for ϵ_r and 3.8 Å for r , which is the separation of nearest-neighbour Cu-Zn ions, gives a value of -0.284 eV for $I_{electrostatic}$. This treatment however only accounts for the Coulombic interaction between the point charges and neglects any changes in the electronic structure during defect formation. The screening effect of the electronic structure would be more significant for the microscopic dielectric constant than for the bulk, macroscopic dielectric constant. In this study therefore we scale the interaction energy, $I_{interaction}$, in the simulations by comparing the formation energy of a nearest-neighbour Cu-Zn anti-site defect pair calculated using the classical code GULP to that obtained using quantum mechanical hybrid-density functional theory and the VASP code, where effects of the electronic structure are included in the calculation. This calculation was performed in a previous study, but details of the calculation are included in Appendix A. We found that the defect formation energy obtained using VASP was approximately 1.5 times that obtained with GULP, we therefore scaled the interaction energy by the same amount and so $I_{DFT} = 1.5 \times I_{electrostatic} = -0.425$ eV. Through doing this we aim to scale the macroscopic dielectric constant to be closer to the value of the microscopic dielectric constant.

4.5 Spatial Extent of Disorder Amongst Cu & Zn Ions

Monte Carlo simulations of thermodynamic substitutions between Cu and Zn ions will be allowed to evolve until the equilibrium configuration in terms of the arrangement of Cu and Zn atoms at the given temperature is reached, which was discussed in section 4.3. The electrostatic potential at each site in the lattice will then be calculated for later analysis of the distribution of electrostatic potential of Sn ions across the system when extracting information on band tailing due to Cu-Zn disorder. The methodology for this will be discussed as future work in section ???. Figure 4.10 shows an example of outputs from our simulations, where the $T = 0\text{K}$ spatial arrangement of cations in figure 4.10a corresponds to the perfectly ordered system and the $T = 200\text{K}$ configuration in figure 4.10b shows spatial clustering of Cu and Zn ions as the system has been allowed to evolve at a finite temperature.

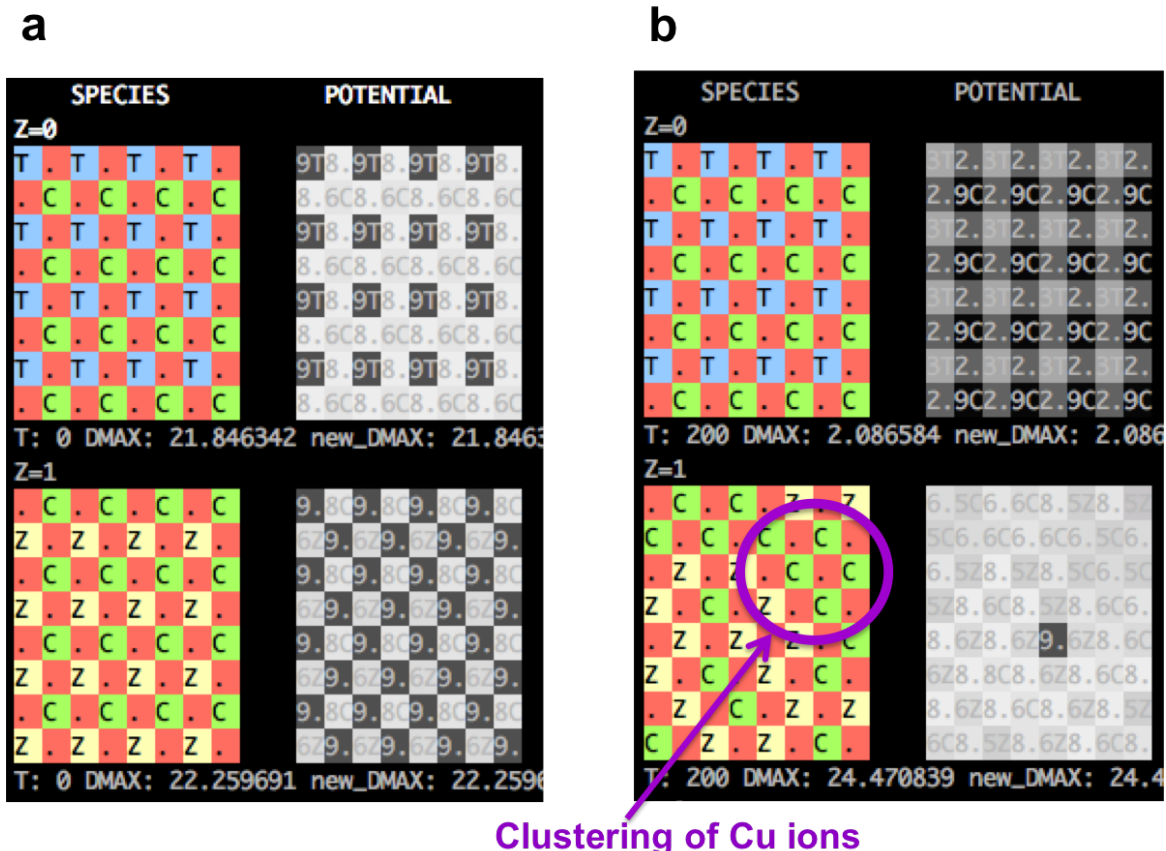


Figure 4.10: Example outputs from Eris Monte Carlo simulations of Cu-Zn disorder from an initially ordered lattice showing the top two layers of the lattice when simulations are performed at temperatures $T = 0\text{K}$ (a) and at $T = 200\text{K}$ (b).

4.6 Quantification of Disorder Using Radial Distribution Functions

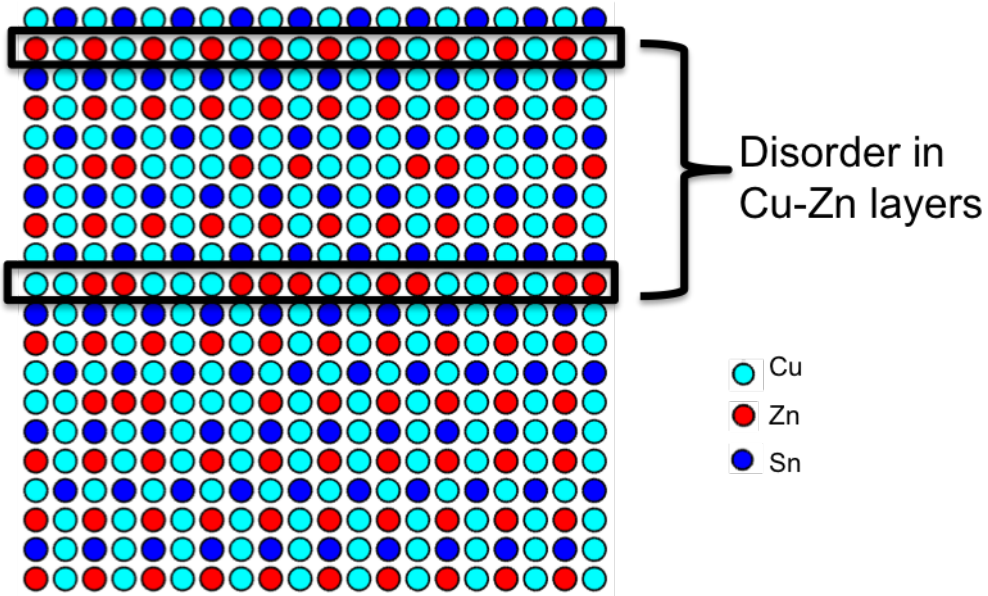


Figure 4.11: A 2D slice of a disordered configuration of the cation sub-lattice of $\text{Cu}_2\text{ZnSnS}_4$, where the top highlighted layer shows an example of perfectly ordered alternating Cu-Zn pattern and the second layer shows an example of a disordered layer.

In order to analyse the extent of disorder in resulting configurations from our simulations, we plan to use radial distribution functions (RDFs). The RDF of a system of particles describes how density varies as a function of distance from a reference particle. In our study we will use the RDF of particular pairs of species to study how the arrangement of Cu and Zn ions varies across the whole system as a result of thermodynamic disorder. The simplest way to quantify disorder could be to use the nearest-neighbour RDF peak of the Cu-Cu or Zn-Zn RDFs as an increase in disorder is associated with clustering of two or more Cu or Zn species together, as shown in figure 4.11. Therefore, when comparing to the RDF of a perfectly ordered system, we could expect a new nearest-neighbour peak to emerge in the Cu-Cu and Zn-Zn RDFs, which will increase in intensity as the regions of clusters of Cu and Zn increase in cluster-size and occur more frequently with disorder. This can be seen in figure 4.12 of the Zn-Zn RDF where a new nearest neighbour peak emerges in the disordered configurations, which was not present for the ordered initial configuration, and the peak appears to increase in intensity going from a system that has been evolved from an initially ordered configuration compared to the disordered initial

configuration. This analysis will not entirely capture the disorder process but could be used to quantify the initial disordering from a perfectly ordered system. Ideas for other methods to quantify disorder will be discussed as future work in section 5.1.

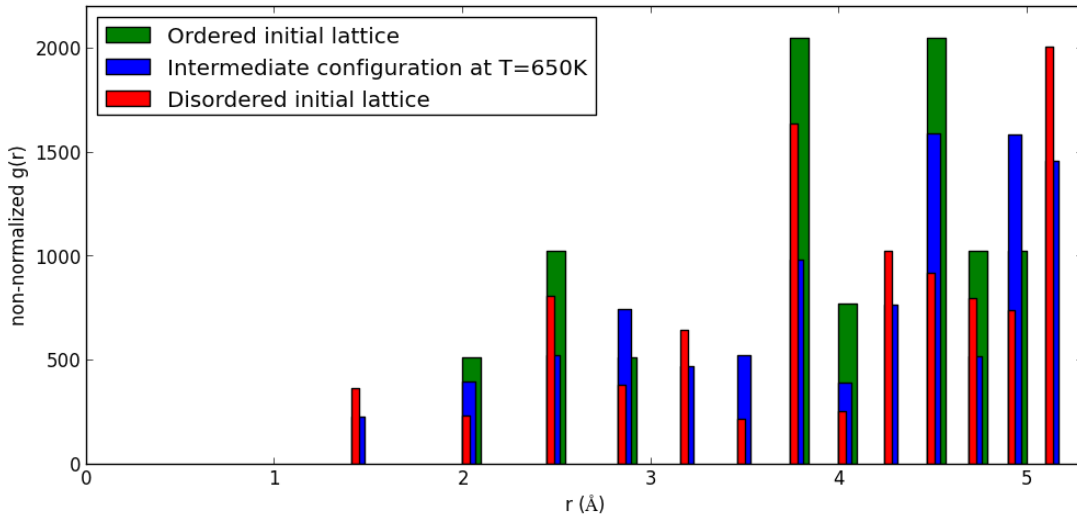


Figure 4.12: The radial distribution function (RDF) between pairs of zinc ions in $\text{Cu}_2\text{ZnSnS}_4$ before normalization. RDFs of an initial perfectly ordered lattice are plotted with that of a disordered initial lattice as well as a system that started from an initially ordered lattice and has been allowed to evolve at $T=650\text{K}$ but note that the system may not yet have reached the equilibrium configuration for the given temperature. Widths of the bars plotted are arbitrarily chosen to ensure all data is visible.

Chapter 5

Conclusion & Future Work

5.1 Further Development of Monte Carlo Disorder Models for Cu₂ZnSnS₄

So far from our simulations we are seeing clear clustering of Cu and Zn ions, such as that shown in figure 4.10b. This is in agreement with a previous study performed for CZTS using a motif-based Hamiltonian and Monte Carlo simulations [162]. In this particular study the authors report on an entropically driven clustering of cations from their simulations. The radial distribution function (RDF) we showed in figure 4.12 also indicates clustering of Zn ions with increased disorder due to the emergence of a new nearest neighbour peak in the Zn-Zn RDF when evolving the system from an initially perfectly ordered lattice.

Our study so far has focused on developing methods to gauge the point at which the system has reached its equilibrium amount of Cu-Zn disorder at the given simulation temperature, before we go on to extract thermodynamic information by averaging over data obtained from subsequent evolution of the system. The first method we attempted was to compare the RDF of a system evolved from an ordered initial lattice to that evolved from an initial disordered lattice. We would then use the principle that a system evolved from any initial configuration should eventually reach the same final configuration once the system has equilibrated to gauge

when the system has equilibrated. The RDF can be used as a measure of long-range structural order so we could consider the point at which the two RDFs are the same (within a range of error) to be the point at which the system has attained its equilibrium configuration. However, so far from our simulations it seems that the system takes a considerably longer time (in terms of Monte Carlo simulation steps) to evolve from an initial disordered lattice. This can be seen in the RDFs shown in figure 4.7, where the RDF of the system evolved from a disordered lattice changes very little from the RDF of the initial configuration compared to that evolved from an ordered lattice.

We next tried tracking the variance in the distribution of the electrostatic potential of Sn ions for the system evolved from an ordered lattice. For a perfectly ordered lattice, the variance is zero due to there being only one unique chemical environment for Sn in perfectly ordered CZTS. From these simulations, where some of the results were shown in figures 4.8 and 4.9, it appears that the system evolved from an ordered initial lattice reaches an equilibrated configuration after a fairly modest number of Monte Carlo steps of approximately 2000 steps in total. This suggests that when starting from this particular configuration, around 2000 steps could be a sensible number of steps to run for the simulation for before collecting data on thermodynamic information about the system.

Our study so far has also focused on developing methods to quantify the Cu-Zn disorder present in large and three-dimensional systems. We have initially just used the RDF for Cu-Cu pairs and Zn-Zn pairs, as discussed above, but we intend to develop more methods. This initial method is based on using the characteristic clustering of Cu and Zn ions as a measure of disorder. This principle could also allow us to use the clusters themselves as a measure of disorder, and possibly another way to gauge if our system has attained its equilibrium configuration. For this development, we will attempt to measure the size of Zn clusters present in the system and then count the number of clusters of each size. The point at which the number of each cluster size does not change after a large number of simulation steps could be considered the point at which the system has reached an equilibrated extent of Cu-Zn disorder.

In addition, there are other methods that have been used in the literature to quantify Cu-

Zn disorder in CZTS, which we could try to apply to our simulations. One method that has been used to quantify short-ranged cation disorder in CZTS involves studying how the local environments of S anions deviate to that in the perfectly ordered crystal lattice [162]. In the case of the ordered crystal, one S anion should be surrounded by two Cu ions, one Zn and one Sn. However as Cu and Zn ions substitute with thermodynamic disorder, a number of different motifs are possible. For example, one S ion could instead be surrounded by one Cu and two Zn ions or three Cu ions and no Zn ions in the first coordination sphere. In reference 162, cation disorder is quantified by counting the number of each type of motif present. This treatment will only capture very short-ranged disorder so we may wish to build upon the methodology of the authors in reference 162 to look at the deviation in the local environment of S anions to next nearest neighbour and next-next-nearest neighbour cations. Or, as we fix Sn ions in our simulations and do not initially include S ions in our Monte Carlo simulations, the local environment of Sn ions could be a more sensible way for us to perform the same type of analysis.

However, the most common method in the literature to quantify Cu-Zn disorder experimentally is to measure the site occupancy of sites which, in a more ordered system, should be preferentially occupied specifically by Cu or Zn. A recent example of such a study where the temperature dependence of Cu/ Zn ordering in CZTSe is measured and quantified in such a way using anomalous diffraction is given in reference 139. In this study the authors define an order parameter Q, shown in equation 5.1, where for example Cu_{2c} indicates the number of 2c sites that are occupied by Cu ions, which corresponds to the correct position for an ordered CZTS lattice. Likewise, Zn_{2d} corresponds to the same situation for sites that should be occupied by Zn in the perfectly ordered system.

$$Q = \frac{[Cu_{2c} + Zn_{2d}] - [Zn_{2c} + Cu_{2d}]}{[Cu_{2c} + Zn_{2d}] + [Zn_{2c} + Cu_{2d}]} \quad (5.1)$$

In a completely disordered system, 2c and 2d sites are occupied by an equal number of Cu and Zn ions, but as a system becomes more ordered Cu and Zn ions preferably occupy the correct site. For a perfectly ordered system, $Q=1$ and for a completely disordered system $Q=0$. In our simulations, we could attempt to implement something similar by studying the occupancy of

the crystallographic sites by considering the original perfectly ordered unit cells the supercell lattices in our simulations were constructed from.

Once we have fully established our methods for gauging when our system has equilibrated and for quantifying structural disorder, the next important step is to investigate the size dependence of our simulation-derived properties. This will be done by using our methods for quantifying disorder. We will vary the system size and study how this effects our order parameters, with the aim of determining a minimum system size for the equilibrium amount of disorder at each temperature to no longer vary with increased system size. Once a suitable system size has been determined, we will then go on to extract information on band tailing in CZTS due to Cu-Zn disorder. We intend to do this by studying the distribution of the electrostatic potential of Sn ions in the various disordered systems. We will investigate how the density of states (DOS) of Sn ions in a disordered system shifts relative to that of a perfectly ordered system. As the electronic environment is related to the ionic environment we will infer that the electronic DOS will be shifted in the same way as the ionic DOS. From this we aim to extract the amount one would expect the electronic DOS to tail into the band gap of the perfectly ordered system, such as that shown in figure 3.8.

5.2 Predicting the Photovoltaic Performance of Other Metal Sulfide Materials

As discussed in section 2.2, another component of this study is to predict the optoelectronic properties of other materials, which have currently received little or no attention for PV, to determine the likely performance of the materials for this application. The three candidate materials were: enargite (Cu_3AsS_4), stephanite (Ag_5SbS_4) and bournonite (PbCuSbS_3). These materials are all classed as sulfosalt minerals and an overview of their known properties was given in section 2.2. The candidate PV materials were originally selected based on the possibility of ferroelectricity due to their polar space group and associated ferroelectric-photovoltaic phenomena, which could open up new possible pathways for high performance PV devices.

However, currently in the study it is only the optoelectronic properties relevant for PV applications that are being studied.

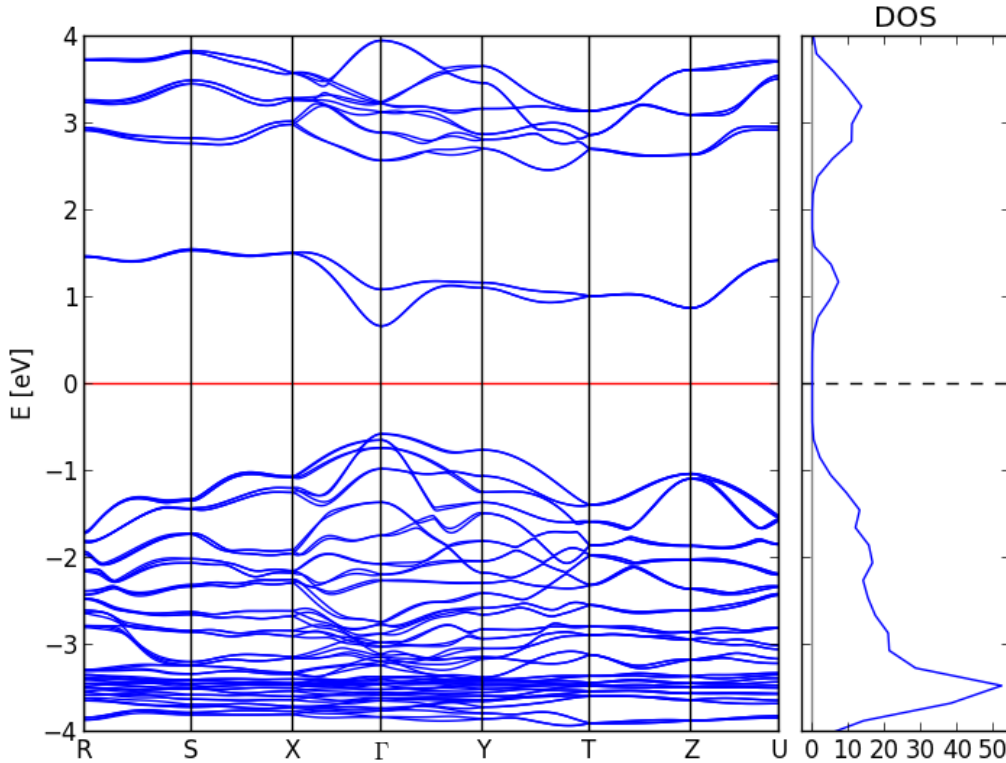


Figure 5.1: Band structure and density of states (DOS) of enargite (Cu_3AsS_4) calculated using the HSE06 functional with spin-orbit coupling. The atomic structure is obtained from experimental lattice parameters with internal atomic positions optimized with the HSE06 functional.

One of the first key material properties for PV applications mentioned in section 1.1.3 was the band gap of the material; both its magnitude relative to the solar spectrum and whether it is direct or indirect in nature. Therefore we firstly calculate the band structures of the materials and these are shown in figures 5.1, 5.2 and 5.3 for enargite, stephanite and bournonite respectively. Electronic structure calculations in this study are performed using the HSE06 functional [56] as implemented in the FHI-aims software package [17, 114, 54], with the inclusion of spin-orbit interaction . Initial geometries are taken from high-quality X-ray diffraction data from the Inorganic Crystal Structure Database (ICSD)[13] for enargite and bournonite and the resolved crystal structure from single crystal X-Ray diffraction measurements performed by Professor Mark Weller at the University of Bath on a natural sample of stephanite during a previous study. Geometry optimization of the structures are then performed allowing only

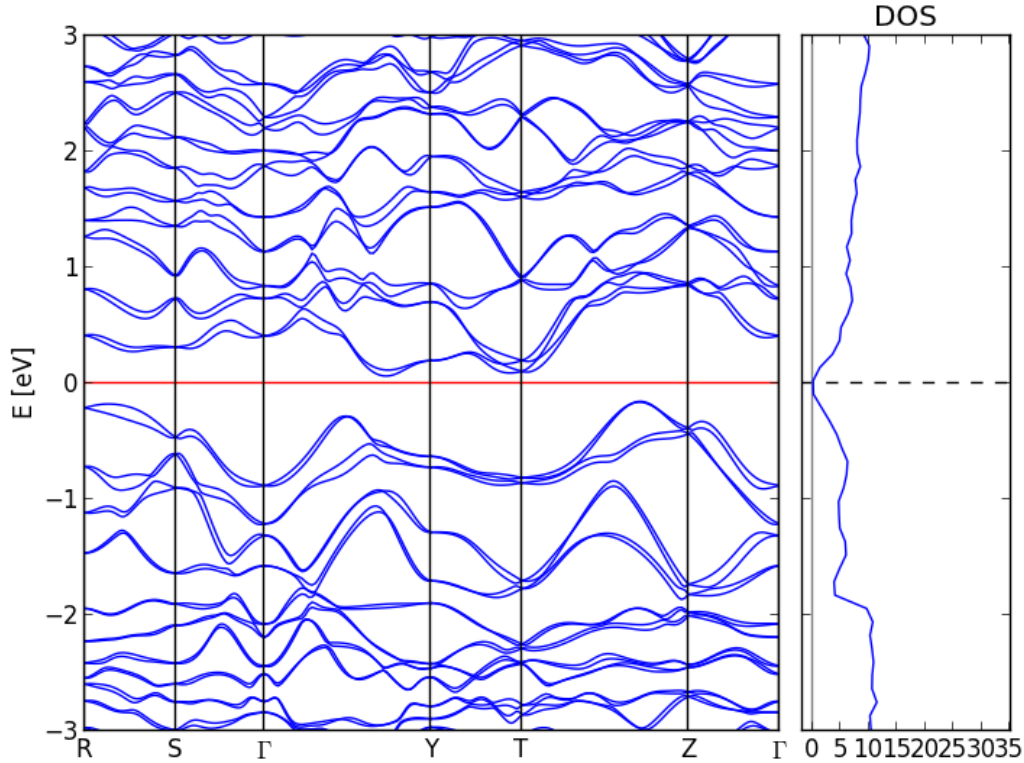


Figure 5.2: Band structure and density of states (DOS) of enargite (Ag_5SbS_4) calculated using the HSE06 functional with spin-orbit coupling. The atomic structure is obtained from experimental lattice parameters with internal atomic positions optimized with the HSE06 functional.

the ionic positions to relax, holding the unit cell parameters constant. An evenly spaced $4 \times 4 \times 4$ k -points grid centred on the Γ -point is used for the k -space sampling of the first Brillouin zone as this was found to be sufficient for the total energies of the systems to converge to within 1 meV in our previous study. Convergence plots from this study are shown in Appendix C. Default ‘tight’ accuracy convergence settings of the FHI-aims code were used for the basis sets and geometry relaxations were performed to obtain optimized structures using the Broyden-Fletcher-Goldfarb-Shanno (BFGS) optimization algorithm as implemented in the FHI-aims code [17] until forces on the atoms converged to within a tolerance of 10^{-3} eV/ Å. Band structures were then plotted along the paths of high symmetry for each type of crystal structure, shown in Appendix D. For band structure calculations the density of the k -points grid was increased to $8 \times 8 \times 8$.

From our calculations, enargite has a direct band gap of 1.24 eV. This is within the range of

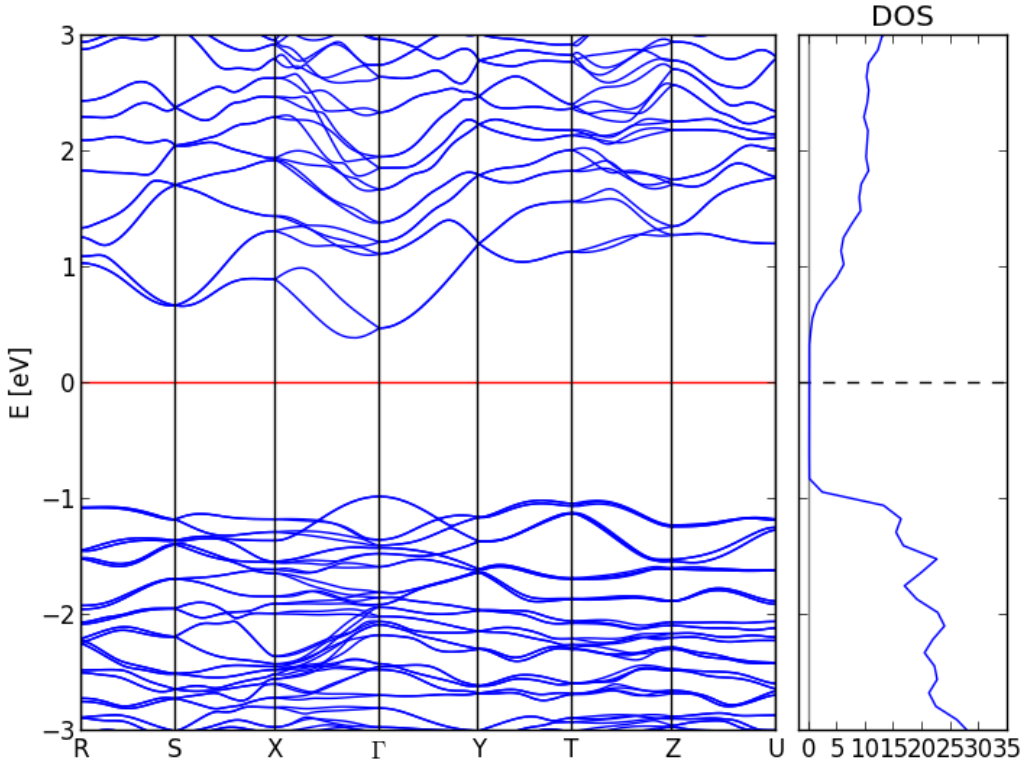


Figure 5.3: Band structure and density of states (DOS) of bournonite (PbCuSbS_3) calculated using the HSE06 functional with spin-orbit coupling. The atomic structure is obtained from experimental lattice parameters with internal atomic positions optimized with the HSE06 functional.

experimental values obtained for the band gap in the literature and is also in good agreement with UV-vis measurements on a natural sample of enargite that we performed during a previous study, which gave a value of approximately 1.2 eV for the band gap. Although it should be noted that this natural sample was found to contain Sb impurities. The value we calculate is also not too far from the 1.32 eV calculated in a previous theoretical study using $\text{G}_0\text{W}_0@\text{HSE06}$ [156]. For stephanite we calculate an indirect band gap of 0.22 eV. As far as we are aware there are no other theoretical predictions for the band gap of this material but our value is considerably less than experimental values obtained in the literature [36] and our UV-vis measurement performed in a previous study which all give a value of around 1.6 eV. For bournonite, we calculate an indirect band gap of 1.37 eV, which is in quite good agreement with experimental values in the literature of 1.23 [36] and 1.31 [149] eV. However to our knowledge there are currently only calculated values for the band gap of bournonite in the literature using GGA and GGA+U

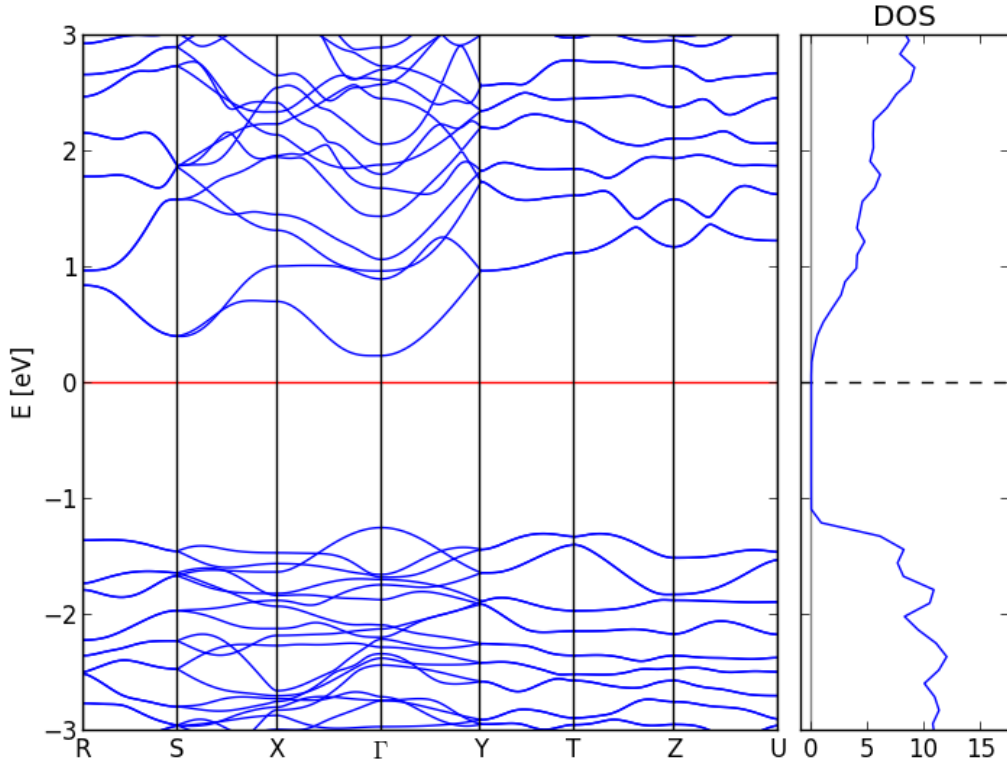


Figure 5.4: Band structure and density of states (DOS) of bournonite (PbCuSbS_3) calculated using the HSE06 functional without spin-orbit coupling. The atomic structure is obtained from experimental lattice parameters with internal atomic positions optimized with the HSE06 functional.

methodologies. From the calculated band structure for bournonite shown in figure 5.3, it appears that the material could exhibit conduction band spin splitting as a consequence of spin-orbit coupling. This is often referred to as Rashba splitting. The long carrier lifetime and diffusion length observed in organometal halide perovskite solar cells has been postulated to be linked to Rashba splitting in the band structure of these materials [164, 9]. In these works the authors suggest that the rate of electron-hole recombination could be reduced due to the spin-forbidden transition, thereby resulting in enhanced carrier lifetimes. Therefore, although the band gap we predict for bournonite is slightly indirect, it could be possible that this property could be beneficial for PV applications. The next step in investigating the optoelectronic properties of bournonite is to determine if the observed band splitting is in fact Rashba splitting. So firstly the band structure has been re-calculated with spin-orbit interaction omitted to see if the splitting is caused by spin-orbit coupling and from figure 5.4 it does appear that the

splitting of the conduction band has disappeared.

However, it has been suggested that the Shockley-Queisser (SQ) theoretical efficiency limit of a solar cell based on the value of direct band gap is not a sufficient screening criteria for candidate PV materials [157]. The authors instead suggest an alternative metric called the ‘spectroscopic limited maximum efficiency’ (SLME), which takes into account the band gap, the shape of the optical absorption spectra and the material-dependent non-radiative recombination losses. In the same work the author’s show that from their metric many materials have a maximum efficiency limit less than that predicted by SQ, this is illustrated in figure 5.5. Interestingly, the authors also find that some materials with similar band gaps (and therefore would have similar SQ limits) have very different theoretical limits from their metric. Therefore a more thorough evaluation of the potential of the candidate materials for applications in PV could be achieved by extending our investigation to encompass the SLME metric.

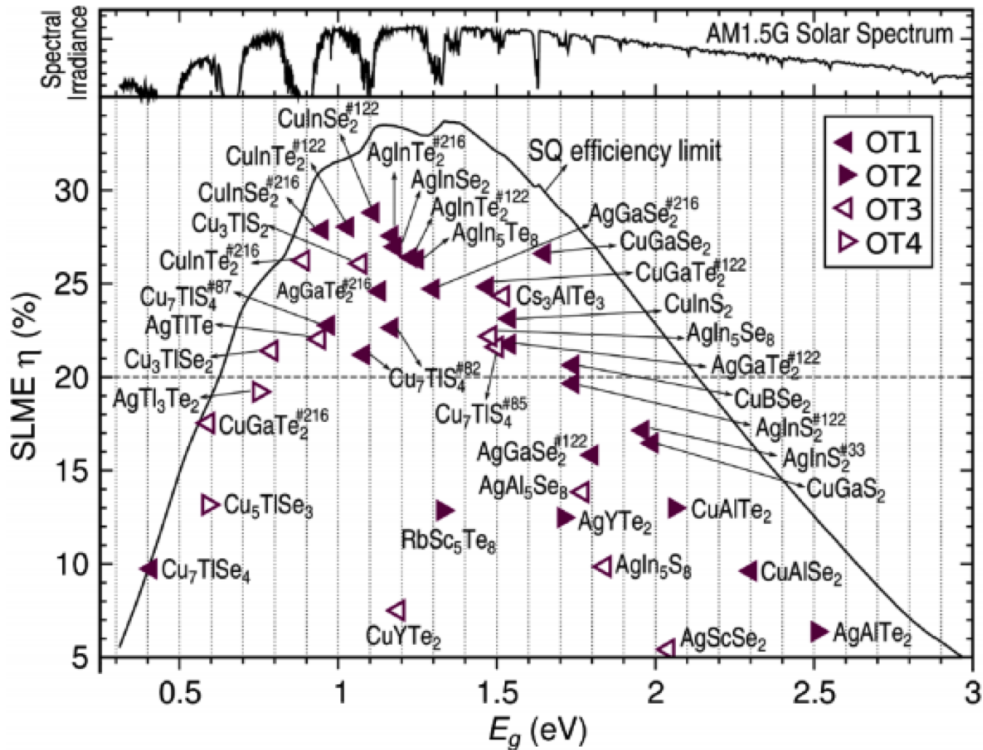


Figure 5.5: Spectroscopic limited maximum efficiency (SLME), η , versus the minimum band gap, E_g , for I-II-VI chalcopyrite materials of thickness $L = 0.5 \mu\text{m}$ (triangles). The Shockley-Queisser (SQ) efficiency limit is shown by the line. Figure taken from reference 157.

Appendix A

Calculation of the Formation Energy of the $[Cu_{Zn}^- + Zn_{Cu}^+]$ Defect Pair in Cu_2ZnSnS_4

The defect formation energy, ΔH_D , is the main quantity of interest in the theoretical description of defects and impurities. It can be used to determine the defect concentrations in equilibrium, as shown in equation A.3, and also the thermodynamic transition energies between different possible charge states of electrically active defects [76]. The former will be discussed later in this section and the latter will be discussed further in relation to sulfur vacancies in Cu_2ZnSnS_4 in section ???. It is common to use the supercell method when performing simulations of defects in solid state systems. In this method, a defect is inserted into a larger supercell to screen interactions between defects across a boundary when implementing periodic boundary conditions. The supercell should be chosen to ensure that it is large enough to prevent interactions between point defects in adjacent cells. In practise, it is often too computationally expensive to meet this requirement completely as the number of atoms in the supercell rises with the third power of the linear size of the supercell and the computational expense then increases with the third power of the number of atoms [132]. In our calculations of defects in Cu_2ZnSnS_4 we use a 64 atom supercell, which is the most isotropic and largest supercell that could feasibly be

used for our calculations at the level of accuracy we required. This corresponds to a cell size of approximately $11 \times 11 \times 11 \text{ \AA}^3$. This supercell is constructed by creating a $2 \times 2 \times 1$ supercell of the conventional CZTS supercell shown in figure 2.1.

The full expression for the formation energy of a defect is given in equation A.1, where $\Delta H_{D,q}$ is the total energy of the supercell containing the defect in charge state q , E_H is the total energy of an equivalent supercell of the perfect host crystal without the defect. The chemical potential μ_α describes the energy of the atomic reservoir of the atoms α removed from or added to the host crystal when the defect forms. For charged defects, where $q \neq 0$, E_F describes the energy of the reservoir of electrons, which is usually considered to be somewhere between the valence band maximum and conduction band minimum, but can be tuned by an applied bias. However, in the case of the antisite pair $[Cu_{Zn}^- + Zn_{Cu}^+]$, we do not add or remove any atoms, we only substitute their positions. Also the defect complex is overall charge neutral and so the full expression simplifies to that shown in equation A.2.

$$\Delta H_{D,q}(E_F, \mu) = [E_{D,q} - E_H] + \sum_{\alpha} n_{\alpha} \mu_{\alpha} + q \cdot E_F \quad (\text{A.1})$$

$$\Delta H_D = E_{D,q} - E_H \quad (\text{A.2})$$

First principles calculations using the density function theory (DFT) formalism have been found to yield reliable information about atomic structure, including the relaxation of the host atoms, during the formation of a defect in a crystal. A brief overview of standard DFT methodology for the calculation of total energies is given in Appendix B. However, in many cases traditional DFT functionals used in standard DFT methods often fail at the description of the electronic structure of a defective crystal. For instance, the local density approximation (LDA) and generalized gradient approximation (GGA), severely underestimate the band gaps of semiconductors and insulators [2]. Defect formation energies are in general affected by this band-gap problem in two ways. Firstly, defect states may be predicted to be within the continuum of host states when the band gap is underestimated but actually be within the band gap if the band-gap problem is corrected. The result of this incorrect placement of the

defect level is that electron-occupied defect states can erroneously spill into the conduction band or similarly hole defects could spill into the valence band. The calculated charge density associated with these defects would then be incorrect, resulting in an uncontrolled error in the value obtained for $\Delta H_{D,q}$. For charged defects, there is an additional source of error due to $\Delta H_{D,q}$ being dependent upon the Fermi level. E_F is bounded by the band-edge energies and so when the band gap is changed the range of formation energies between the valence band maximum and conduction band minimum is altered [76]. The band gap problem can be addressed by going beyond DFT. One such method is hybrid-DFT. Hybrid approaches incorporate a certain amount of screened exact exchange from the Hartree-Fock approximation with DFT exchange-correlation functionals. Hybrid functionals, such as the HSE06 functional [56] used in this study have been shown to produce band structures in much better agreement with experiment and provide a much more reliable description of charge localization, which is essential for accurate modeling of low-symmetry defects or structures that give rise to polaron formation [2].

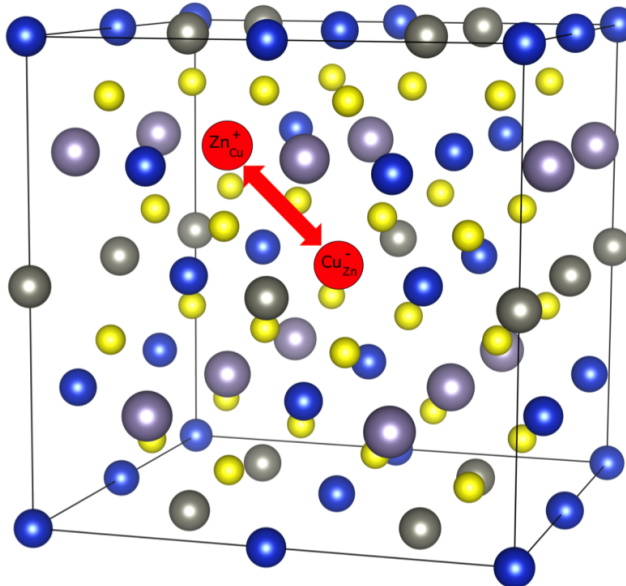


Figure A.1: 64 atom supercell of $\text{Cu}_2\text{ZnSnS}_4$ showing a substitution of Cu and Zn ions that results in the formation of the nearest neighbour antisite defect pair.

For our calculations of the formation energy of the nearest-neighbour $[\text{Cu}_{\text{Zn}}^- + \text{Zn}_{\text{Cu}}^+]$ defect pair (shown in figure A.1), we make use of the Heyd-Scuseria-Ernzerhof (HSE06) hybrid-functional [56] for the exchange-correlation functional as implemented in the Vienna Ab-initio Simula-

tion Package (VASP) [72]. This functional mixes 25% of screened Hartree-Fock exchange to the Perdew-Burke-Ernzerhof (PBE) exchange functional [105]. Projector augmented-wave potentials [73] were used to describe the core electrons with an energy cut-off of 500 eV for the plane-wave basis set. Calculations were initially performed at the gamma point (a 1x1x1 k -point mesh) until forces on the ions converged to within 0.01 eV/ Å. A single geometry step was then performed with a 2x2x2 k -point mesh centred on the gamma point as these parameters were found to be sufficient for the total energy to converge to within <2 meV per atom with respect to increased plane-wave cut-off energy and for the external pressure to be <1 kbar. However, performing the full calculation with a 2x2x2 k -point mesh was found to be too computationally expensive. Data for the convergence test is given in table A.1. From our calculation, we predict a defect formation energy of 0.30 eV.

Cut-off energy (eV)	k -points (Å)	Total energy, E (eV)	External pressure (kbar)	dE per atom (meV)
300	$1 \times 1 \times 1$	-305.53	-174.59	
350	$1 \times 1 \times 1$	-306.95	-23.86	- 22.12
400	$1 \times 1 \times 1$	-307.49	8.21	- 8.47
450	$1 \times 1 \times 1$	-307.08	5.71	6.33
500	$1 \times 1 \times 1$	-307.20	4.02	- 1.87
300	$2 \times 2 \times 2$	-306.76	-180.97	
500	$2 \times 2 \times 2$	-308.72	-0.08	

Table A.1: Convergence tests performed on the perfect CZTS supercell with various plane wave cut-off energies for the basis set and number of k -points in the sampling where dE is the difference in the total energy obtained as the cut-off energy for the plane-wave basis set is increased in increments of 50 eV.

When defect concentrations are less than 1%, it is usually assumed that the system is in the dilute defect limit where defects can be considered to be non-interacting. Using statistical thermodynamics for point defects, an expression for the equilibrium concentration of point defects as a function of temperature can be obtained [145]. This is shown in equation A.3, where N is the number of sites, ΔH is the defect formation energy, k_B is the Boltzmann constant and T is the temperature of the system.

$$n = Ne^{\frac{-\Delta H}{k_B T}} \quad (\text{A.3})$$

The probability of defect formation as a function of temperature is given by the exponential expression in equation A.3. The defect formation energy from the DFT calculations were halved to take an average of the formation energy per defect during the formation of an antisite pair before being inserted into this expression. This is plotted against temperature in figure A.2. It can be seen from figure A.2 that the probability of defect formation at a typical annealing

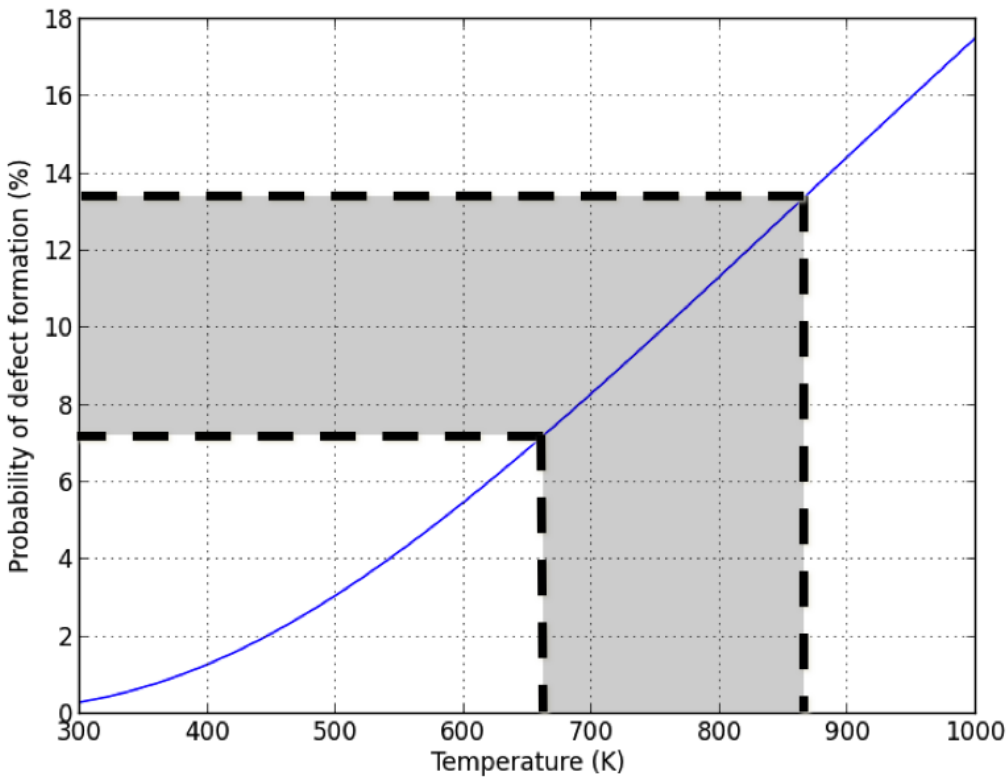


Figure A.2: Probability of nearest neighbour $[Cu_{Zn}^- + Zn_{Cu}^+]$ defect formation as a function of temperature based on the equilibrium defect concentration from classical thermodynamics. The shaded region indicates typical annealing temperatures used in the synthesis of Cu_2ZnSnS_4 .

temperatures is approximately 7-13%. It was also found that, compared to the undefective system, there was a decrease in the separation of the antisite defects of 3.84\AA to 3.82\AA after the geometry optimization. This effect could be due to a Coulombic attraction between the two antisite defects. The point defects (the Cu_{Zn}^- and Zn_{Cu}^+ antisites) form the defect complex $[Cu_{Zn}^- + Zn_{Cu}^+]$. The point defects become associated with one another due to a Coulomb interaction between the effective +1 and -1 charge that results from substituting species with a +1 charge with a species with a +2 charge and vice versa. This, in addition to the high equilibrium concentrations of antisite defects predicted, suggests that it is not sufficient to

consider the Cu_{Zn}^- and Zn_{Cu}^+ antisites as non-interacting point defects and that we must instead consider a system of interacting defects. We aim to do this through our Monte Carlo simulations of thermodynamic disorder, which are discussed in section 4.

Appendix B

Density Functional Theory (DFT) Methodology for the Calculation of Total Energy

Electronic Structure Calculations

Modelling electrons requires the use of quantum mechanics, the basis of which is the Schrödinger equation, which describes the energy of the electrons and nuclei within a material where electrons interact with the positively charged atomic nuclei through an electrostatic potential [77].

The Schrödinger equation for a one particle system is given in equation B.1.

$$\left(-\frac{\hbar}{2m}\nabla^2 + \hat{V}\right)\psi(r,t) = i\hbar\frac{\partial\psi}{\partial t} \quad (\text{B.1})$$

However, for systems containing even more than one electron this becomes a very complex problem. This is due to the many electrons in the system interacting with each other as well as with the nuclei. When dealing with such systems, the Born-Oppenheimer approximation is almost universally used. As electrons are fast moving relative to the nuclei, they are considered to be moving in the classical field generated by static nuclei. This decouples the nuclear and

electronic degrees of freedom, reducing the problem to solving only the electronic structure of the system. The total energy of the system is then just the sum of the energy of the electrons and the nuclei. The Schrödinger equation for a system containing M nuclei and N electrons is shown in equation B.2 [77]. This is still a very complex mathematical problem for most systems. For example, ψ in equation B.2 for 1 cm³ of a typical metal would be a function of approximately 10²³ variables.

$$\left\{ -\frac{\hbar^2}{2m} \left(\frac{\nabla_{n_1}^2}{m_1} + \dots + \frac{\nabla_{n_M}^2}{m_M}, \frac{\nabla_{e_1}^2}{m} + \dots + \frac{\nabla_{e_M}^2}{m} \right) + V(\mathbf{R}_1, \dots, \mathbf{R}_M, \mathbf{r}_1, \dots, \mathbf{r}_N) \right\} \psi(\mathbf{R}_1, \dots, \mathbf{R}_M, \mathbf{r}_1, \dots, \mathbf{r}_N, t) = i\hbar \frac{\partial \psi(\mathbf{R}_1, \dots, \mathbf{R}_M, \mathbf{r}_1, \dots, \mathbf{r}_N, t)}{\partial t} \quad (\text{B.2})$$

Density Functional Theory (DFT)

Density functional theory (DFT) is a method to dramatically reduce the computational expense of solving the many-electron Schrödinger equation, by simplifying the problem. Firstly, DFT considers only the ground state of a system, which dominates most of the properties of a material. This then enables a different formalism of many-body quantum mechanics based on the Hohenberg-Kohn Theorem [57], which states that the ground state energy of a system of electrons in an external potential depends only on the electronic density, ρ . This results in a dramatic reduction in the complexity of the mathematical problem as the key quantity in the expression is now ρ , which is only a function of 3 variables, in comparison to the many-body wavefunction ψ which is a function of 3N variables where N is typically a very large number of electrons within a system. The Kohn-Sham formalism of DFT then produces N non-interacting Schrödinger equations, such as that shown in equation B.3.

$$\left\{ -\frac{\hbar^2}{2m} \nabla^2 + V[\rho(\mathbf{r})] + V_{xc}[\rho(\mathbf{r})] \right\} \psi(\mathbf{r}) = \epsilon \psi(\mathbf{r}) \quad (\text{B.3})$$

The Kohn-Sham method then uses an iterative solution, which is illustrated in figure B.1. An initial guess is made for the set of wavefunctions ψ_i^0 , an initial electron density, ρ_0 , is then constructed from this where ρ is given by equation B.4. The effective Kohn-Sham potential,

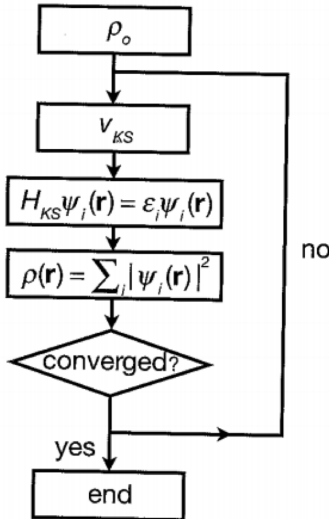


Figure B.1: Steps in the solution of the self-consistent field method. Figure taken from reference 77.

V_{ks} , is then found based on this value of the electron density and equation B.5, where V_{ext} is the external potential and $V_{xc} = \frac{\delta E_{xc}}{\delta \rho(\mathbf{r})}$ where E_{xc} is the exchange-correlation function chosen.

$$\rho(\mathbf{r}) = \sum_{i=1}^N |\psi_i(\mathbf{r})|^2 \quad (\text{B.4})$$

$$V_{ks}(\mathbf{r}) = V_{ext}(\mathbf{r}) + \int \frac{\rho(\mathbf{r})}{|\mathbf{r} - \mathbf{r}_1|} d\mathbf{r}_1 + V_{xc}(\mathbf{r}) \quad (\text{B.5})$$

As V_{ks} is defined by the electron density from the previous step in the iteration cycle, the Hamiltonian includes no direct interaction between electrons. Instead, it describes each electron as moving in an external field based on a fixed electron distribution $\rho(\mathbf{r})$. The Kohn-Sham equation shown in equation B.3 is then solved with the second and third terms replaced by V_{ks} calculated in equation B.5, to give a new set of wavefunctions and 1-electron orbital energies (ϵ). From this a new ρ is found and then a new V_{ks} , until the new value for ρ does not change anymore than a certain prescribed amount after each iteration. This would then be considered to be the ground state energy of the system and this is referred to as a self-consistent process [77].

$$\psi = \sum_j c_j \phi_j \quad (\text{B.6})$$

$$\phi(\mathbf{r}) = ce^{i(\mathbf{k}+\mathbf{G}) \cdot \mathbf{r}} \quad (\text{B.7})$$

$$\phi(\mathbf{r}) = \frac{u_i(r)}{r} Y_{lm}(\Omega) \quad (\text{B.8})$$

Typically, the wavefunction is expanded as a sum over a set of basis functions as shown in equation B.6. For solids, the wavefunctions should reflect the periodicity of the system. Plane-waves, such as that shown in equation B.7, are often chosen for the basis set of a crystal and this is the basis set used in the Vienna Ab-initio Simulation Package (VASP) [72]. In the case of the Fritz Haber Institute ab initio molecular simulations (FHI-aims) software package, numeric atom-centred orbital (NAO) basis functions, such as that shown in equation B.8, are the basis set used. The radial shape, $u_i(r)$, is numerically tabulated and so fully flexible enabling the creation of optimized element-dependent basis sets that are as compact as possible to minimize computational expense. To exactly represent the wavefunction may require an infinitely large basis set. In practise, the basis set must be truncated at some point. The consequence of this is that the minimum energy obtained by the iterative method in figure B.1 will always be an upper bound of the true minimum energy of the system. If the size of the basis set is increased, then this minimum value of the energy calculated will decrease further and further towards the true value until convergence is reached such that adding any additional basis states does not change the energy by more than a prescribed amount.

The FHI-aims package provides pre-constructed default definitions of the basis set for each species depending on the level of accuracy required from the calculations, where these defaults are referred to as ‘light’, ‘tight’ or ‘really_tight’ settings. Light settings are recommended for initial screening for minimum energy structures or fast pre-relaxations where the relaxed structure can then be used as the input for subsequent more accurate calculations. The developers state that meV-level converged energy differences can be expected for large molecular structures using these settings. Tight settings are stated to guarantee meV-level accuracy for large structures and really_tight settings are described as only being necessary for individual tests

to ensure sufficient accuracy was achieved with less computationally expensive settings [17]. However when using the VASP software package, the usual practise is to perform convergence tests with calculations with increased energy cut-off for the plane wave basis set.

In periodic DFT calculations, the total energy is also converged with respect to the number of k -points used to sample the Brillouin zone. Each electron occupies a state of definite \mathbf{k} . Therefore, in a periodic crystal structure an infinite number of electrons would result in an infinite number of k -points. At each k -point, only a finite number of the available energy levels will be occupied. Therefore only a finite number of electrons need to be considered but at an infinite number of k -points. In practise, all of these k -points are not considered. Electron wavefunctions will be almost identical for values of \mathbf{k} that are sufficiently close, so the wavefunctions over a region of reciprocal space can be represented by considering the wavefunction at a single k -point. It is therefore sufficient to consider the electronic states at a finite number of k -points in order to determine the ground state energy of the solid. This approximation is illustrated in figure B.2. Bloch's Theorem enables the ground state energy to be approximately determined by considering only the number of electrons in the unit cell at a finite number of k -points, which are chosen to sample the Brillouin zone appropriately. The choice here is a balance between more k -points for a more accurate representation of the Brillouin zone and fewer k -points to reduce the computational expense of the calculation [138]. An example of a convergence test for the k -grid used in our DFT calculations is shown in Appendix C.

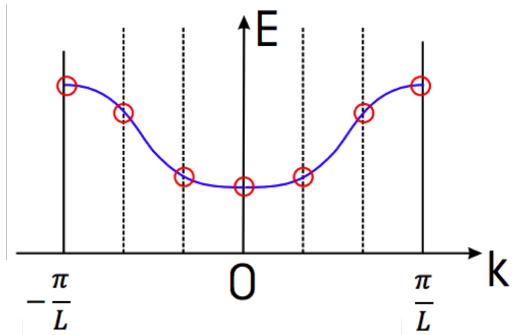


Figure B.2: The energy dispersion relation for electrons moving in a crystal, illustrating how the function can be approximately represented by a finite number of k -points, which form an equally-spaced mesh. Figure adapted from reference 39.

The fundamental approximation in DFT is the form the unknown exchange-correlation func-

tional, $E_{xc}[\rho]$. The most simple functionals are based on the local density approximation (LDA) where an electron with a given local electron density is assumed to experience the same many-body response as if the whole material had this same electron density. The next correction to LDA includes the local gradient of the electron density. These methods are referred to as generalised gradient approximations (GGA). These approximations are commonly used for solids and work well for metallic systems which have a fairly uniform electron density. However, they are well known to under-estimate the band gap of semiconductors and insulators. It is possible to ascend the ‘ladder of DFT Chemical accuracy’ [106] by incorporating more complexity and costly ingredients into the exchange-correlation functional. Hybrid functionals have been shown to give values for the band gaps of various semiconductors that are in much better agreement with experimental values than those calculated using GGA functionals [21]. In Hybrid approaches there is an interpolation between exact exchange from the Hartree-Fock approximation and DFT exchange-correlation functionals [77]. In this study we made use of the Heyd-Scuseria-Ernzerhof (HSE06) hybrid functional [56].

Appendix C

Convergence of Total Energy with Number of K-Points for Geometry Optimization of Sulfosalt Crystal Structures

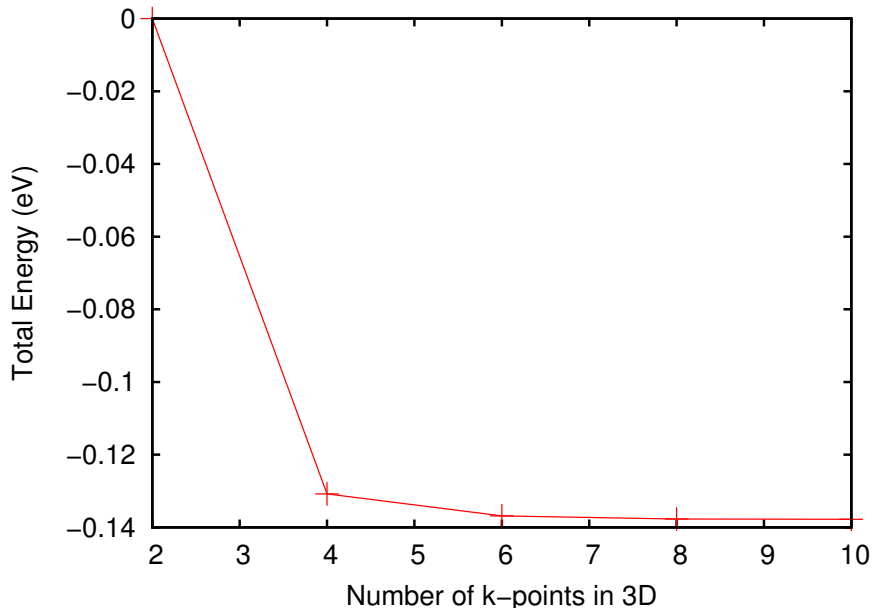


Figure C.1: Convergence of the change in calculated total energy for enargite (Cu_3AsS_4) with respect to the number of k -points used in the three-dimensional sampling of the first Brillouin zone in density functional theory calculations of total energy.

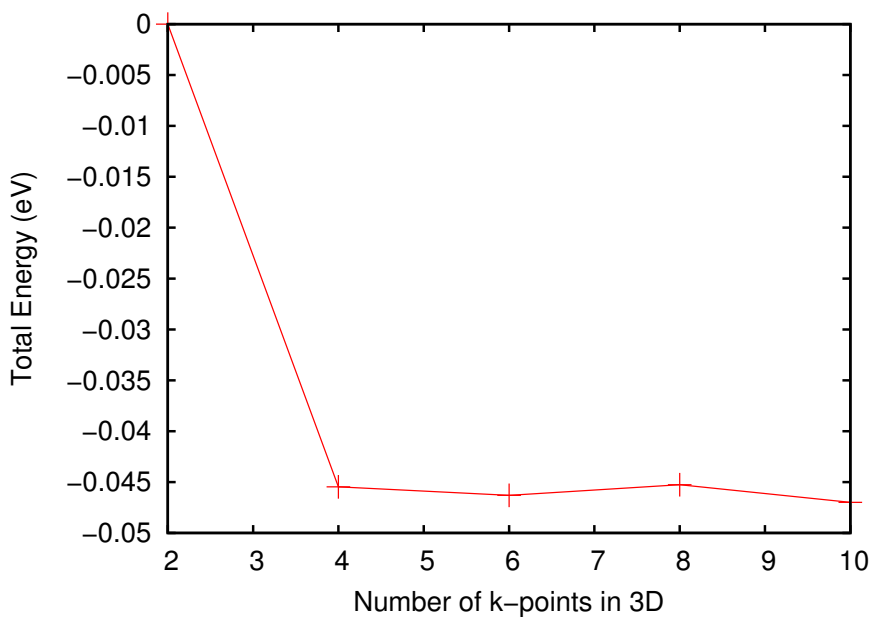


Figure C.2: Convergence of the change in calculated total energy for bournonite (PbCuSbS_3) with respect to the number of k -points used in the three-dimensional sampling of the first Brillouin zone in density functional theory calculations of total energy.

Appendix D

High Symmetry Paths for Sulfosalt Band Structure Calculations

The high-symmetry points of the Brillouin zones of the crystal structures being studied here are shown in figure D.1 and given in units of reciprocal lattice vectors in table D, which were taken from the Bilbao Crystallographic Server [4, 3]. The high symmetry lines for each of the crystal structures are shown in equations D.1 and D.2 where equation D.1 shows the high symmetry lines for the crystal structure $\text{Pmn}2_1$, which is that of enargite (Cu_3AsS_4) and bournonite (PbCuSbS_3), and equation D.2 shows the high symmetry lines for crystal structure $\text{Cmc}2_1$, which is that of stephanite (Ag_5SbS_4).

$$R \longrightarrow S \longrightarrow X \longrightarrow \Gamma \longrightarrow Y \longrightarrow T \longrightarrow Z \longrightarrow U \quad (\text{D.1})$$

$$R \longrightarrow S \longrightarrow \Gamma \longrightarrow Y \longrightarrow T \longrightarrow Z \longrightarrow \Gamma \quad (\text{D.2})$$

Calculations of the electronic band structure in this study are performed using the FHI-aims DFT code [17], which was described in the section above. In practise, this is implemented in the FHI-aims code by requesting the band structure along the high symmetry lines shown in

equations D.1 and D.2 to be outputted from a starting point, such as the Γ point, to an end point such as Y with a certain number of points in between, which determines how smooth the plot will appear.

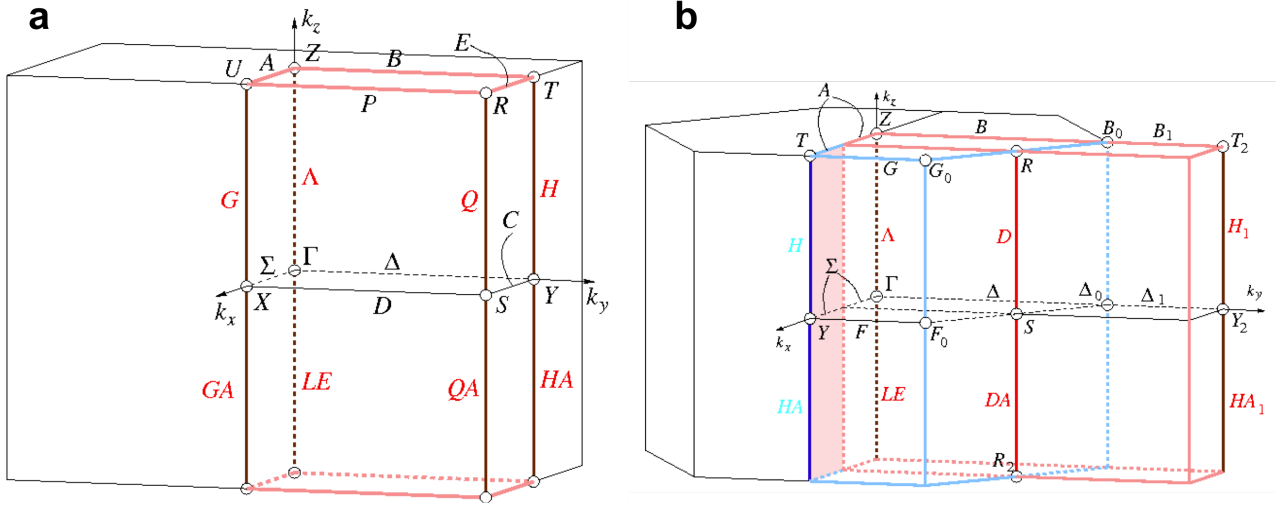


Figure D.1: The reciprocal lattice shown with the first Brillouin zone for the space groups Pmn₂₁ (a) and Cmc₂₁ (b), where the former is the space group of enargite (Cu_3AsS_4) and bournonite (PbCuSbS_3) and the latter is the space group of stephanite (Ag_5SbS_4). Figures taken from the Bilbao Crystallographic Server [4, 3].

Pmn ₂ ₁			Cmc ₂ ₁				
x_1	x_2	x_3	x_1	x_2	x_3		
R	0.5	0.5	0.5	R	0	0.5	0.5
S	0.5	0.5	0	S	0	0.5	0
X	0.5	0	0	Γ	0	0	0
Γ	0	0	0	Y	0.5	0.5	0
Y	0	0.5	0	T	0.5	0.5	0.5
T	0	0.5	0.5	Z	0	0	
Z	0	0	0.5	Γ	0	0	0
U	0.5	0	0.5				

Table D.1: High symmetry points for the Pmn₂₁ and Cmc₂₁ given in units of reciprocal lattice vectors ($\mathbf{k} = x_1\mathbf{b}_1 + x_2\mathbf{b}_2 + x_3\mathbf{b}_3$), taken from the Bilbao Crystallographic Server [4, 3].

Bibliography

- [1] T. Abzieher, T. Schnabel, M. Hetterich, M. Powalla, and E. Ahlswede. Source and effects of sodium in solution-processed kesterite solar cells. *Phys. Status Solidi*, 11, 2015.
- [2] A. Alkauskas, M. D. McCluskey, and C. G. Van de Walle. Tutorial: Defects in semiconductorsCombining experiment and theory. *Journal of Applied Physics*, 119(18):181101, 2016.
- [3] M. I. Aroyo, D. Orobengoa, G. de la Flor, E. S. Tasçi, J. M. Perez-Mato, and H. Won-dratschek. Brillouin-zone database on the bilbao crystallographic server. *Acta Cryst.*, A70, 2014.
- [4] M. I. Aroyo, J. M. Perez-Mato, D. Orobengoa, E. Tasçi, G. de la Flor, and A. Kirov. Crystallography online: Bilbao crystallographic server. *Bulg. Chem. Commun.*, 43:183–197, 2011.
- [5] N. Ashcroft and N. Mermin. *Crystal Lattices*. Saunders College Publishing, 1976.
- [6] N. Ashcroft and N. Mermin. *The Reciprocal Lattice*. Saunders College Publishing, 1976.
- [7] N. Ashcroft and N. Mermin. *Solid State Physics*. Saunders College Publishing, 1976.
- [8] E. P. I. Association. Global market outlook for photovoltaics 2014-2018. 2014.
- [9] P. Azarhoosh, S. McKechnie, J. M. Frost, A. Walsh, and M. van Schilfgaarde. Research Update: Relativistic origin of slow electron-hole recombination in hybrid halide perovskite solar cells. *APL Mater.*, 4(9):091501, sep 2016.

- [10] T. L. Bahers, M. Rérat, and P. Sautet. Semiconductors used in Photovoltaic and Photo-catalytic Devices: Assessing Fundamental Properties from DFT. *J. Phys.* . . . , 2014.
- [11] M. Balkanski and R. F. Wallis. *Introduction to Transport in Semiconductors*. OUP Oxford, 2000.
- [12] W. Bao and M. Ichimura. Influence of Secondary Phases in Kesterite-Cu₂ZnSnS₄ Absorber Material Based on the First Principles Calculation. *Int. J. Photoenergy*, 2014(c), 2014.
- [13] G. Bergerhoff and I. Brown. *Crystallographic Databases*, 1987.
- [14] BISEM. *SMUD & BISEM-USA complete first ever PV Curtain Wall Retrofit project in USA*, 2010 (Accessed on May 17, 2016).
- [15] J. Blakemore. *Crystallinity and the Form of Solids: Reciprocal Space*. Cambridge University Press, 1985.
- [16] J. Blakemore. *Electrons in Metals: The band Theory of Solids*. Cambridge University Press, 1985.
- [17] V. Blum, R. Gehrke, F. Hanke, P. Havu, V. Havu, X. Ren, K. Reuter, and M. Scheffler. *Computer Physics Communications*, 180:2175–2196, 2009.
- [18] K. W. Böer. *Handbook of the Physics of Thin-Film Solar Cells*. Springer, 2013.
- [19] M. Bokalič and M. Topič. *Spatially Resolved Characterization in Thin-Film Photovoltaics*.
- [20] R. L. Bonevitz. *Minerals*. Dorling Kindersley, Ltd, 2012.
- [21] S. Botti, D. Kammerlander, and M. A. L. Marques. Band structures of cu_2znsns_4 and $cu_2znsnse_4$ from many-body methods. *Applied Physics Letters*, 98(24):–, 2011.
- [22] S. Bourdais, C. Choné, B. Delatouche, A. Jacob, G. Larramona, C. Moisan, A. Lafond, F. Donatini, G. Rey, S. Siebentritt, A. Walsh, and G. Dennler. Is the Cu/Zn Disorder the Main Culprit for the Voltage Deficit in Kesterite Solar Cells? *Adv. Energy Mater.*, mar 2016.

- [23] R. E. Brandt, V. Stevanovi, D. S. Ginley, and T. Buonassisi. Identifying defect-tolerant semiconductors with high minority-carrier lifetimes: beyond hybrid lead halide perovskites. *MRS Communications*, 5:265–275, 6 2015.
- [24] F. Brivio, A. B. Walker, and A. Walsh. Structural and electronic properties of hybrid perovskites for high-efficiency thin-film photovoltaics from first-principles. *APL Mater.*, 1(4):042111, 2013.
- [25] K. T. Butler, J. M. Frost, and A. Walsh. Ferroelectric Materials for Solar Energy Conversion: Photoferroics Revisited. (December):1–11, 2014.
- [26] N. I. Butsko, I. D. Zhezhnich, and P. M. M. *Some Physical Properties of Stephanite in the Phase Transition Region*, 1973 (Accessed on September 3, 2015).
- [27] S. Chen, X. G. Gong, A. Walsh, and S.-H. Wei. Crystal and electronic band structure of $Cu_2ZnSn_xS_4$ (x=s and se) photovoltaic absorbers: First-principles insights. *Applied Physics Letters*, 94(4):–, 2009.
- [28] S. Chen, X. G. Gong, A. Walsh, and S.-H. Wei. Defect physics of the kesterite thin-film solar cell absorber Cu_2ZnSnS_4 . *Appl. Phys. Lett.*, 96(2):021902, 2010.
- [29] S. Chen, J.-H. Yang, X. G. Gong, A. Walsh, and S.-H. Wei. Intrinsic point defects and complexes in the quaternary kesterite semiconductor Cu_2ZnSnS_4 . *Physical Review B*, 81(24):245204, June 2010.
- [30] W. S. Choi, M. F. Chisholm, D. J. Singh, T. Choi, G. E. Jellison, and H. N. t. . Lee.
- [31] A. G. Chynoweth. Surface space-charge layers in barium titanate. *Phys. Rev.*, 102:705–714, May 1956.
- [32] E. S. Cortezon, R. Aninat, and E. Sanchez-cortezon. Kesterite-based photovoltaic devices: Challenges for scale-up. In *Proceedings of the IEEE Photovoltaic Specialist*, 2016.
- [33] S. Curtarolo, G. L. W. Hart, M. B. Nardelli, N. Mingo, S. Sanvito, and O. Levy. The high-throughput highway to computational materials design. *Nat. Mater.*, 12(3):191–201, Mar. 2013.

- [34] J. P. Dakin and R. G. W. Brown. *Engineered Optical Materials*. CRC Press, 2010.
- [35] H. Dittrich, A. Bieniok, U. Brendel, M. Grodzicki, and D. Topa. Sulfosalts A new class of compound semiconductors for photovoltaic applications. *Thin Solid Films*, 515(15):5745–5750, May 2007.
- [36] H. Dittrich, A. Stadler, D. Topa, H. J. Schimper, and A. Basch. Progress in sulfosalt research. *Phys. Status Solidi Appl. Mater. Sci.*, 206(5):1034–1041, 2009.
- [37] Y. Dong, A. R. Khabibullin, K. Wei, J. R. Salvador, G. S. Nolas, and L. M. Woods. Bournonite pbcusbs3: Stereochemically active lone-pair electrons that induce low thermal conductivity. *ChemPhysChem*, 2015.
- [38] H. Du, F. Yan, M. Young, B. To, C.-S. Jiang, P. Dippo, D. Kuciauskas, Z. Chi, E. A. Lun, C. Hancock, W. M. H. OO, M. A. Scarpulla, and G. Teeter. Investigation of combinatorial coevaporated thin film Cu_2ZnSnS_4 . i. temperature effect, crystalline phases, morphology, and photoluminescence. *Journal of Applied Physics*, 115:173502, 2014.
- [39] A. Eichler. *Sampling the Brillouin Zone*, 2014 (Accessed on April 28, 2015).
- [40] F. Espinosa-Faller. Neutron Diffraction and Xray Absorption Fine Structure Evidence for Local Lattice Distortions and Aperiodic Antisite Substitution in Cu_2ZnSnS_4 Nanoparticles. *The Journal of Physical Chemistry C*, 118:26292–26303, 2014.
- [41] H. Föll. *Point Defects*, (Accessed on 30 June, 2016).
- [42] F. I. for Solar Energy Systems ISE. *Levelized Cost of Electricity Renewable Energy Technologies*, 2013 (Accessed on Aug 3, 2015).
- [43] M. Fox. *Optical Properties of Solids*. Oxford University Press, 2010.
- [44] V. Fthenakis. Sustainability of photovoltaics: The case for thin-film solar cells. *Renewable and Sustainable Energy Reviews*, 13(9):2746 – 2750, 2009.
- [45] T. Gershon, B. Shin, N. Bojarczuk, T. Gokmen, S. Lu, and S. Guha. Photoluminescence characterization of a high-efficiency Cu_2ZnSnS_4 device. *J. Appl. Phys.*, 114(15):154905, 2013.

- [46] T. Gershon, B. Shin, T. Gokmen, S. Lu, N. Bojarczuk, and S. Guha. Relationship between Cu_2ZnSnS_4 quasi donor-acceptor pair density and solar cell efficiency. *Appl. Phys. Lett.*, 103(May):2012–2015, 2013.
- [47] C. D. Ginley, David S. Cambridge University Press, 2012.
- [48] J. E. Girard. *Principles of Environmental Chemistry*. Jones & Bartlett Learning, LLC, 2014.
- [49] T. Gokmen, O. Gunawan, T. K. Todorov, and D. B. Mitzi. Band tailing and efficiency limitation in kesterite solar cells. *Applied Physics Letters*, 103(10):–, 2013.
- [50] B. Goldstein and L. Pensak. *J. Appl. Phys.*, 155, 1959.
- [51] J. L. Gray. *The Physics of the Solar Cell*, pages 61–112. John Wiley & Sons, Ltd, 2005.
- [52] M. Grundmann. *The Physics of Semiconductors*. Springer, 2006.
- [53] D. P. Halliday, R. Claridge, M. C. Goodman, B. G. Mendis, K. Durose, and J. D. Major. Luminescence of Cu_2ZnSnS_4 polycrystals described by the fluctuating potential model. *J. Appl. Phys.*, 113(22):2013, 2013.
- [54] V. Havu, V. Blum, P. Havu, and M. Scheffler. Efficient integration for all-electron electronic structure calculation using numeric basis functions. *Journal of Computational Physics*, 228(22):8367 – 8379, 2009.
- [55] W. Hermes, D. Waldmann, M. Agari, K. Schierle-Arndt, and P. Erk. Emerging Thin-Film Photovoltaic Technologies. *Chemie Ingenieur Technik*, 87(4):376–389, 2015.
- [56] J. Heyd, G. E. Scuseria, and M. Ernzerhof. Hybrid functionals based on a screened Coulomb potential. *J. Chem. Phys.*, 118(18):8207–8215, 2003.
- [57] P. Hohenberg and W. Kohn. *Phys. Rev.*, 136, 1964.
- [58] K. Hönes, E. Zscherpel, J. Scragg, and S. Siebentritt. Shallow defects in Cu_2ZnSnS_4 . *Phys. B Condens. Matter*, 404(23-24):4949–4952, 2009.

- [59] C. Honsberg and S. Bowden. *Open-Circuit Voltage*, 2014 (Accessed on April 28, 2015).
- [60] R. E. Hummel. *Electronic Properties of Materials*. Springer Science+Business Media, 2012.
- [61] F. S. Inc. *Emissions from Photovoltaic Life Cycles*, 2009 (Accessed on April 18, 2015).
- [62] S. J. C. Irvine. RSC Energy and Environment Series, 2014.
- [63] K. Ito. *An Overview of CZTS-Based Thin-Film Solar Cells*. John Wiley & Sons, 2015.
- [64] K. Ito and T. Nakazawa. *Jpn. J. Appl. Phys.*, 27:2094–2097, 1998.
- [65] J. Jean, P. R. Brown, R. L. Jaffe, T. Buonassisi, and V. Bulovic. Pathways for Solar Photovoltaics. *Energy Environ. Sci.*, 2015.
- [66] H. R. Johnson, R. H. Williams, and C. H. B. Mee. The anomalous photovoltaic effect in cadmium telluride. *Journal of Physics D: Applied Physics*, 8(13):1530, 1975.
- [67] A. K. Jonscher. *The Electronic Structure of Solids*. Routledge & Kegan Paul Ltd., 1965.
- [68] A. K. Jonscher. *The Imperfect Solid*. Routledge & Kegan Paul Ltd., 1965.
- [69] J. Kim, H. Hiroi, T. K. Todorov, O. Gunawan, M. Kuwahara, T. Gokmen, D. Nair, M. Hopstaken, B. Shin, Y. S. Lee, W. Wang, H. Sugimoto, and D. B. Mitzi. High efficiency $Cu_2ZnSn(s, se)_4$ solar cells by applying a double in_2s_3/cds emitter. *Advanced Materials*, 26(44):7427–7431, 2014.
- [70] B. Kolb and A. M. Kolpak. First-Principles Design and Analysis of an Efficient, Pb-Free Ferroelectric Photovoltaic Absorber Derived from $ZnSnO_3$. *Chem. Mater.*, 27(17):5899–5906, 2015.
- [71] V. Kosyak, N. B. Mortazavi Amiri, A. V. Postnikov, and M. A. Scarpulla. Model of native point defect equilibrium in Cu_2ZnSnS_4 and application to one-zone annealing. *J. Appl. Phys.*, 114(12), 2013.

- [72] G. Kresse and J. Furthmüller. Efficiency of ab-initio total energy calculations for metals and semiconductors using a plane-wave basis set. *Computational Materials Science*, 6(1):15 – 50, 1996.
- [73] G. Kresse and D. Joubert. From ultrasoft pseudopotentials to the projector augmented-wave method. *Phys. Rev. B*, 59:1758–1775, Jan 1999.
- [74] D. P. Landau and K. Binder. *A Guide to Monte Carlo Simulations in Statistical Physics*. Cambridge University Press, 2015.
- [75] D. W. Lane, K. J. Hutchings, R. McCracken, and I. Forbes. *New Chalcogenide Materials for Thin Film Solar Cells*. The Royal Society of Chemistry, 2015.
- [76] S. Lany and A. Zunger. Accurate prediction of defect properties in density functional supercell calculations. *Model. Simul. Mater. Sci. Eng.*, 17(8):084002, 2009.
- [77] R. Lesar. *Electronic Structure Methods*. Cambridge University Press, 2014.
- [78] R. Lesar. *The Monte Carlo Method*. Cambridge University Press, 2014.
- [79] S. Levchenko, V. E. Tezlevan, E. Arushanov, S. Schorr, and T. Unold. Free-to-bound recombination in near stoichiometric Cu_2ZnSnS_4 single crystals. *Phys. Rev. B*, 86(4):045206, 2012.
- [80] S. S. Li. *Semiconductor Physical Electronics*. Plenum Press, New York, 1993.
- [81] I. Lifshitz. *The energy spectrum of disordered systems*, volume 13. 1964.
- [82] M. E. Lines and A. M. Glass. Oxford University Press, 1977.
- [83] D. Ltd. *What is Levelised Cost of Energy (LCOE)?*, 2011 (Accessed on Aug 10, 2015).
- [84] A. Luque and S. Hegedus. *Handbook of Photovoltaic Science and Engineering*. John Wiley & Sons, Ltd, 2011.
- [85] A. McEvoy, T. Markvart, and L. C. ner. *Practical Handbook of Photovoltaics - Fundamentals and Applications*. Elsevier, 2012.

- [86] B. G. Mendis, M. D. Shannon, M. C. Goodman, J. D. Major, R. Claridge, D. P. Halliday, and K. Durose. Direct observation of cu, zn cation disorder in $\text{Cu}_2\text{ZnSnS}_4$ solar cell absorber material using aberration corrected scanning transmission electron microscopy. *Progress in Photovoltaics: Research and Applications*, 22(1):24–34, 2014.
- [87] B. G. Mendis, M. D. Shannon, M. C. J. Goodman, J. D. Major, A. A. Taylor, D. P. Halliday, and K. Durose. The nature of electrostatic potential fluctuations in $\text{Cu}_2\text{ZnSnS}_4$ and their role on photovoltaic device performance. *Journal of Physics: Conference Series*, 471(1):012014, 2013.
- [88] N. Metropolis, A. W. Rosenbluth, M. N. Rosenbluth, A. H. Teller, and E. Teller. Equation of State Calculations by Fast Computing Machines. *J. Chem. Phys.*, 21(6):1087–1092, 1953.
- [89] Y. Miyamoto, K. Tanaka, M. Oonuki, N. Moritake, and H. Uchiki. Optical Properties of $\text{Cu}_2\text{ZnSnS}_4$ Thin Films Prepared by SolGel and Sulfurization Method. *Jpn. J. Appl. Phys.*, 47(1):596–597, 2008.
- [90] J. E. Moore, C. J. Hages, R. Agrawal, M. S. Lundstrom, and J. L. Gray. The importance of band tail recombination on current collection and open-circuit voltage in CZTSSe solar cells. *Applied Physics Letters*, (109):021102, 2016.
- [91] J. Nelson. *Generation and Recombination*. Imperial College Press, 2003.
- [92] J. Nelson. *Introduction*. Imperial College Press, 2003.
- [93] J. Nelson. *Photons In, Electrons Out: Basic Principles of PV*. Imperial College Press, 2003.
- [94] J. Neugebauer and T. Hickel. Density functional theory in materials science. *Wiley Interdiscip. Rev. Comput. Mol. Sci.*, 3(5):438–448, sep 2013.
- [95] M. E. J. Newman and G. T. Barkema. *The Ising Model and the Metropolis Algorithm*. Oxford University Press, 1999.
- [96] R. E. Newnham. *Dielectric Constant*. Oxford University Press, 2005.

- [97] U. D. of Energy. Energy efficiency and renewable energy: 2008 solar technologies market report. 2010.
- [98] U. of Oregon Investment Group. *First Solar, Inc*, 2011 (Accessed on 05 May, 2016).
- [99] M. I. of Technology. *The Future of Solar Energy*, 2015 (Accessed on June 9, 2015).
- [100] A. Orlova, R. Gainov, A. Dooglav, I. Penkov, and E. Korolev. Structure and transport properties of stephanite (ag_5sbs_4) according to antimony nuclear quadrupole resonance. *JETP Letters*, 96(6):370–374, 2012.
- [101] C. Paillard, X. Bai, I. C. Infante, M. Guennou, G. Geneste, M. Alexe, J. Kreisel, and B. Dkhil. Photovoltaics with Ferroelectrics: Current Status and Beyond. *Adv. Mater.*, apr 2016.
- [102] J. I. Pankove. *Optical Processes in Semiconductors*. Dover Publications, Inc, 1971.
- [103] T. Pauporte and D. Lincot. ChemInform Abstract: Electrical, Optical and Photoelectrochemical Properties of Natural Enargite, Cu_3AsS_4 . *Adv. Mater. Opt. Electron.*, 5:289–298, 1995.
- [104] N. Pearson. *Crystal Defects*, 2014 (Accessed on 30 June, 2016).
- [105] J. P. Perdew, K. Burke, and M. Ernzerhof. Generalized gradient approximation made simple. *Phys. Rev. Lett.*, 77:3865–3868, Oct 1996.
- [106] J. P. Perdew and K. Schmidt. Jacob's ladder of density functional approximations for the exchange-correlation energy. *AIP Conference Proceedings*, 577(May):1–20, 2001.
- [107] C. Persson and A. Zunger. Anomalous grain boundary physics in polycrystalline cuinse₂: The existence of a hole barrier. *Phys. Rev. Lett.*, 91:266401, Dec 2003.
- [108] C. Persson and A. Zunger. Compositionally induced valence-band offset at the grain boundary of polycrystalline chalcopyrites creates a hole barrier. *Appl. Phys. Lett.*, 87(21):211904, 2005.

- [109] J. Piprek. *Semiconductor Optoelectronic Devices: Introduction to Physics and Simulation.* Elsevier Science, 2003.
- [110] A. Polizzotti, I. L. Repins, R. Noufi, S.-H. Wei, and D. B. Mitzi. The state and future prospects of kesterite photovoltaics. *Energy Environ. Sci.*, 6:3171–3182, 2013.
- [111] A. Polman, M. Knight, E. C. Garnett, B. Ehrler, and W. C. Sinke. Photovoltaic materials: Present efficiencies and future challenges. *Science*, 352(6283), 2016.
- [112] I. E. A. P. P. S. Programme. Trends in photovoltaic applications, 19th edition. 2014.
- [113] K. Ramanathan and et al. *Prog. Photovolt. Res. Appl.*, 2003.
- [114] X. Ren, P. Rinke, V. Blum, J. Wieferink, A. Tkatchenko, A. Sanfilippo, K. Reuter, and M. Scheffler. Resolution-of-identity approach to hartreefock, hybrid density functionals, rpa, mp2 and gw with numeric atom-centered orbital basis functions. *New Journal of Physics*, 14(5):053020, 2012.
- [115] M. J. Romero, H. Du, G. Teeter, Y. Yan, and M. M. Al-Jassim. Comparative study of the luminescence and intrinsic point defects in the kesterite Cu_2ZnSnS_4 and chalcopyrite $Cu(In, Ga)Se_2$. *Phys. Rev. B*, 84(16):165324, 2011.
- [116] K. Rudisch, Y. Ren, C. Platzer-Björkman, and J. Scragg. Order-disorder transition in b-type cu_2znsns_4 and limitations of ordering through thermal treatments. *Applied Physics Letters*, 108:231902, 2016.
- [117] T. Saga. Advances in crystalline silicon solar cell technology for industrial mass production. *NPG Asia Mater.*, 2(3):96–102, 2010.
- [118] H. W. Schock. *Adv. Solid State Phys.*, page 147, 1994.
- [119] S. Schorr. The crystal structure of kesterite type compounds: A neutron and x-ray diffraction study. *Solar Energy Materials and Solar Cells*, 95(6):1482 – 1488, 2011. Special Issue : Thin film and nanostructured solar cells.

- [120] S. Schorr, H.-J. Hoebler, and M. Tovar. A neutron diffraction study of the stannite-kesterite solid solution series. *Eur. J. Miner.*, 19(65):65–73, 2007.
- [121] I. Science and T. Directory. *List of Periodic Table Elements Sorted by Abundance in Earth's crust*, 1999 (Accessed on September 2, 2015).
- [122] J. J. S. Scragg, L. Choubrac, A. Lafond, T. Ericson, and C. Platzer-Björkman. A low-temperature order-disorder transition in Cu_2ZnSnS_4 thin films. *Appl. Phys. Lett.*, 104(4):041911, Jan. 2014.
- [123] J.-S. Seol, S.-Y. Lee, J.-C. Lee, H.-D. Nam, and K.-H. Kim. Electrical and optical properties of cu_2znsns_4 thin films prepared by rf magnetron sputtering process. *Solar Energy Materials and Solar Cells*, 75(12):155 – 162, 2003. {PVSEC} 12 Part {II}.
- [124] A. Shah, P. Torres, R. Tscharner, N. Wyrsch, and H. Keppner. Photovoltaic technology: The case for thin-film solar cells. *Science*, 285(5428):692–698, 1999.
- [125] Z. Shahan. *13 Charts On Solar Panel Cost & Growth Trends*, 2014 (Accessed on 15 May, 2016).
- [126] W. Shockley and H. J. Queisser. Detailed balance limit of efficiency of pn junction solar cells. *Journal of Applied Physics*, 32(3), 1961.
- [127] W. Shockley and W. T. Read. Statistics of the recombinations of holes and electrons. *Phys. Rev.*, 87:835–842, Sep 1952.
- [128] R. Shuey. *Semiconducting Ore Minerals*. Elsevier, 2012.
- [129] S. Siebentritt and S. Schorr. Kesterites - a challenging material for solar cells. *Prog. Photovoltaics Res. Appl.*, 20(February):512–519, 2012.
- [130] S. Siebentritt and S. Schorr. Kesterites-a challenging material for solar cells. *Prog. Photovoltaics Res. Appl.*, 20(February):512–519, 2012.
- [131] T. G. E. Society. *Introduction and the history of photovoltaics*. Routledge, 2013.

- [132] J. Spaeth and H. Overhof. *Computational Methods for Deep Point Defects*. Springer-Verlag Berlin Heidelberg, 2003.
- [133] J. Starkiewicz, L. Sosnowski, and O. Simpson. *Nature*, 158, 1946.
- [134] C. Tablero. The optical properties of CuPbSbS₃-bournonite with photovoltaic applications. *Theor. Chem. Acc.*, 135(5):126, apr 2016.
- [135] S. Tajima, T. Itoh, H. Hazama, K. Ohishi, and R. Asahi. Improvement of the open-circuit voltage of cu₂zns_ns₄ solar cells using a two-layer structure. *Applied Physics Express*, 8(8):082302, 2015.
- [136] R. J. D. Tilley. *Colour in Metals, Semiconductors and Insulators*. John Wiley & Sons, Ltd, 2011.
- [137] A. E. I. to the Knowledge of Mineralogy. *Capacitive Circuits*. Collins and Co., 1818.
- [138] P. R. Tulip. Dielectric and Lattice Dynamical Properties of Molecular Crystals via Density Functional Perturbation Theory: Implementation within a First Principles Code, 2004.
- [139] D. M. Tbbens, G. Gurieva, S. Levchenko, T. Unold, and S. Schorr. Temperature dependency of cu/zn ordering in cztse kesterites determined by anomalous diffraction. *physica status solidi (b)*, 2016.
- [140] T. Unold, S. Kretzschmar, J. Just, O. Zander, B. Schubert, B. Marsen, and H.-W. Schock. Correlation between composition and photovoltaic properties of Cu₂ZnSnS₄ thin film solar cells. *Photovolt. Spec. Conf. (PVSC), 2011 37th IEEE*, pages 2820–2823, 2011.
- [141] F. Urbach. The long-wavelength edge of photographic sensitivity and of the electronic absorption of solids. *Phys. Rev.*, 92:1324–1324, Dec 1953.
- [142] T. Urban. *The Deal With Solar*, 2016 (Accessed on 23 April, 2016).
- [143] USGS. *Commodity Statistics and Information*, 2014 (Accessed on September 2, 2015).
- [144] M. D. Uspenskii, N. G. Ivanova, and M. I. E. Sov. *Phys.- Semicond*, page 1059, 1968.

- [145] P. Varotsos and K. Alexopoulos. *Thermodynamics of Point Defects and Their Relation with Bulk Properties*. 1986.
- [146] P. Vela. SEM , EDX and EIS study of an electrochemically modified electrode surface of natural enargite (Cu₃AsS₄). 494:87–95, 2000.
- [147] J. Vidal. *UK and Germany break solar power records*, 2014 (Accessed on 04 May, 2016).
- [148] T. Washio, H. Nozaki, T. Fukano, T. Motohiro, K. Jimbo, and H. Katagiri. Analysis of lattice site occupancy in kesterite structure of cu_2znsns_4 films using synchrotron radiation x-ray diffraction. *J. Appl. Phys.*, 110:074511, 2011.
- [149] K. Wei, J. Martin, J. R. Salvador, and G. S. Nolas. Synthesis and characterization of bournonite pbkusbs3 nanocrystals. *Crystal Growth & Design*, 15(8):3762–3766, 2015.
- [150] S.-Y. Wei, Y.-C. Liao, C.-H. Hsu, C.-H. Cai, W.-C. Huang, M.-C. Huang, and C.-H. Lai. Achieving high efficiency $Cu_2ZnSn(S,Se)_4$ solar cells by non-toxic aqueous ink: Defect analysis and electrical modeling. *Nano Energy*, 26:74–82, aug 2016.
- [151] H. Wirth. *Recent Facts about Photovoltaics in Germany*, 2015 (Accessed on 04 May, 2016).
- [152] S. D. Wolf, J. Holovsky, S.-J. Moon, P. Lper, B. Niesen, M. Ledinsky, F.-J. Haug, J.-H. Yum, and C. Ballif. Organometallic halide perovskites: Sharp optical absorption edge and its relation to photovoltaic performance. *The Journal of Physical Chemistry Letters*, 5(6):1035–1039, 2014. PMID: 26270984.
- [153] J. Yan and B. R. Saunders. Third-generation solar cells: a review and comparison of polymer:fullerene, hybrid polymer and perovskite solar cells. *RSC Adv.*, 4:43286–43314, 2014.
- [154] Y. Yan, W.-J. Yin, T. Shi, F. Hong, J. Ge, Y. Yue, W. Ke, D. Zhao, and A. Cimaroli. Theoretical and experimental study of earth-abundant solar cell materials. In *Active-Matrix Flatpanel Displays and Devices (AM-FPD), 2015 22nd International Workshop on*, pages 57–60, July 2015.

- [155] B. Yang, L. Wang, J. Han, Y. Zhou, H. Song, S. Chen, J. Zhong, L. Lv, D. Niu, and J. Tang. Cu₃Bi₂S₃ as a promising earth-abundant photovoltaic absorber material: A combined theoretical and experimental study. *Chemistry of Materials*, 26(10):3135–3143, 2014.
- [156] L. Yu, R. S. Kokenyesi, D. a. Kesler, and A. Zunger. Inverse design of high absorption thin-film photovoltaic materials. *Adv. Energy Mater.*, 3(1):43–48, 2013.
- [157] L. Yu and A. Zunger. Identification of potential photovoltaic absorbers based on first-principles spectroscopic screening of materials. *Phys. Rev. Lett.*, 108:068701, Feb 2012.
- [158] P. Y. Yu and M. Cardona. *Electronic Band Structures*. Springer-Verlag Berlin Heidelberg, 2010.
- [159] Y. Yuan, Z. Xiao, B. Yang, and J. Huang. Arising applications of ferroelectric materials in photovoltaic devices. *J. Mater. Chem. A*, 2(17):6027, 2014.
- [160] A. A. Zaky and R. Hawley. *Dielectric Solids*. Routledge & Kegan Paul, Ltd, 1970.
- [161] A. A. Zaky and R. Hawley. *Dielectrics in Static Fields*. Routledge & Kegan Paul, Ltd, 1970.
- [162] P. Zawadzki, A. Zakutayev, and S. Lany. Entropy-driven clustering in tetrahedrally bonded multinary materials. *Phys. Rev. Applied*, 3:034007, Mar 2015.
- [163] H. Zhao and C. Persson. Optical properties of Cu(*in, ga*)Se₂ and Cu₂ZnSn(S, Se)₄. *Thin Solid Films*, 519(21):7508 – 7512, 2011. Proceedings of the {EMRS} 2010 Spring Meeting Symposium M: Thin Film Chalcogenide Photovoltaic Materials.
- [164] F. Zheng, L. Z. Tan, S. Liu, and A. M. Rappe. Rashba spinorbit coupling enhanced carrier lifetime in ch₃nh₃pbi₃. *Nano Letters*, 15(12):7794–7800, 2015. PMID: 26461166.
- [165] H. Zimmermann. *Integrated Silicon Optoelectronics*. Springer, 2010.